Transition Metal Doped Semiconductor Nanoclusters and Nanotubes: A Density Functional Investigation

Thesis

Submitted in partial fulfillment of the requirements for the degree of

Doctor of Philosophy

by

Kapil

2011PHXF027P

Under the Supervision of

Prof. Debashis Bandyopadhyay

BIRLA INSTITUTE OF TECHNOLOGY & SCIENCE PILANI

PILANI (RAJASTHAN) INDIA

2016

BIRLA INSTITUTE OF TECHNOLOGY AND SCIENCE, PILANI

CERTIFICATE

This is to certify that the thesis entitled "Transition metal doped semiconductor nanoclusters and nanotubes: a density functional investigation" and submitted by Kapil, ID No 2011PHXF027p for award of Ph.D. of the Institute embodies original work done by him under my supervision.

Supervisor

Date:

(Prof. Debashis Bandyopadhyay)
Department of Physics,
BITS, Pilani, Pilani campus
Rajasthan-333031, India

Dedicated To

My Mother

ACKNOWLEDGEMENTS

Though only my name appears on the cover of this dissertation, a great many people have contributed to its completion. I owe my gratitude to all those people who have made this dissertation possible and because of whom my doctorate experience has been one that I will cherish forever.

I would like to express my special appreciation and thanks to my advisor Prof. Debashis Bandyopadhyay. He has been a tremendous mentor for me. I would like to thank him for encouraging my research and for allowing me to grow as a research scientist. His advice on both research as well as on my career have been priceless. He gave me enough freedom in thinking and choosing my own problems which helped me to bring out my best. I owe him my sincere gratitude for having me shown this way of research.

I would also like to thank my DAC members, Dr. Srijata Day and Dr. Jayendra Nath Bandyopadhyay for serving as my committee members even at hardship. I also want to thank for their brilliant comments and suggestions.

I would like to gratefully acknowledge Prof. V.S. Rao, vice chancellor of BITS Pilani, for giving me the opportunity to join the institute. I also express my gratitude to Prof. A.K. Sarkar, Director, BITS Pilani, Prof. S. K. Verma, Dean, Academic research division, BITS, Pilani, Prof. Hemant Jadhav, Associate Dean, Academic research division, BITS, Pilani for their co-operation and encouragement at every stage of my Ph.D. program. I would like to thank Dr. Anshuman, Unit Chief, Estate Management, BITS, Pilani for helping me with a pleasant stay at BITS, Pilani.

I convey my cordially gratitude to Prof. D. D. Pant, Head of Physics Department and Prof. Rakesh Choubisa, DRC Convener for providing me all the necessary departmental facilities at various stages of my research work. Also, I wish to express my gratitude to all the faculty members in Physics department for their kind help time-to-time.

I owe my deep gratitude to Prof. Prasenjit Sen, HRI Allahabad (U.P.) for his initial support for learning and understanding the basics of different softwares and also for computational facilities provided.

I am immensely thankful to the administration of BITS, Pilani for their help and support. I would express my gratitude to Mr. Rajiv Gaur and Mr. Shrikant Sharma for constant help at time. I am thankful to the office staff of Academic research division, Mr. Mahipal and Mr. Raghuvir for all the help and good wishes.

Most importantly, none of this would have been possible without the love, patience and guidance of my mother Mrs. Kitab Kour. My mother to whom this thesis is dedicated to, has been a constant source of love, concern, support and strength from the day I born. Thank you mom for everything. You are the real hero and a huge

motivation for me and nothing is comparable to your love. Without you my life would be meaningless. Thank you very much for all the support that I needed in order to constantly push myself to succeed.

I would like to express my heart-felt gratitude to Mr. Rajesh Dhaka (Bhaiya) and Mrs. Sapna Poonia Dhaka (Bhabhi) for their love, blessings and invaluable support they have provided throughout this endeavor.

My acknowledgment will never be complete without mentioning the name of my friend, my brother, Dr. C. Karthik. I thank him for always standing beside me and for helping me get through the difficult times, and for all the emotional support, camaraderie, entertainment and care he provided.

Life is always been a tough task without good friends. I wish to thank few of my close friends, especially, Dr. Neha Gupta (Applied Materials India Pvt Ltd, Chennai, India) for helping, supporting and motivating me constantly during my Ph.D. work. I would like to thank Dr. Mona Arora for the constant push and support she provided during these years.

I thank all research scholars of Physics department for the stimulating discussions, and for all the fun we have had in the last five years. At same time I would like to express my special thanks to my friend Dr. Vikas Chouhan (VCU, Richmond, USA), for his fruitful discussions. I want to extend my thanks to my Lab-mate Ravi Trivedi and Dr. Manish kumar for helping me to carry out my research work.

I deeply acknowledge BITS, Pilani and UGC-BSR for the financial assistance throughout my Ph.D. tenure.

Kapil Dhaka

Date:

ABSTRACT

In the field of computational materials science, one of the most fundamental approaches for modeling new materials with desired novel properties is to assemble atoms and clusters at nanocluster level. Such modeled materials may find applications in the field of nanoscience and nanotechnology. For such nano order assemblies, the use of transition metal (TM) doped clusters as building blocks are fruitful due to their suitable geometries, high stability and easily tunable electronic as well as the magnetic properties. The prevalence of silicon and germanium in the semiconductor industry has sparked great interest in the area of nanomaterials that could act as building blocks for new easy-to-combine and engineered materials. The present thesis systematically assesses the feasibility of using transition metal (TM) doped silicon and germanium clusters and to design novel functionalized cluster-assembled materials using density functional methodology. Initially, a thorough analysis of the nature of chemical bonding within exohedrally and endohedrally TM doped Ge_n (TM = Ni, Cr, Mo, Au) clusters, have been done. The study of their energetic and the chemical bonding between the dopant and host atoms explain the stability of such clusters. The shell closing number obtained by Hund's rule also plays an important role to explain the cause of structure stabilization. It explains the adaptive capability of the TM-Ge bonding, which is due to the result of a complex hybridization rather than the originally proposed mere formal charge transfer. Other reasons to stabilize these clusters are the localization of the electrons, which can be theoretically measured by the negative value of nuclear independent chemical shift (NICS). Similar approach are also employed in the case of TM doped Si clusters. The resulting strong interaction of the TM dopant atom with Si/Ge atoms unfortunately results in the quenching of the dopant's spin moment due to sp^3 hybridization between the doped atom and the Ge/Si atoms on the cluster surface. However, we have used hydrogen termination in the small clusters to exploits the dangling bonds and to get the idea of infinite TM doped nanotubes made by using similar kind of simi-infinite tube like cluster assembled structures. Similar effect can be obtained by adding more cluster units to make an infinite nanotube. These units can be taken as the base units or possibly modified base clusters depending upon the level of concentration of the doped atoms or the structural orientation. This will finally makes a functionalized cluster assembled material. Interestingly, the chemical, electronic and magnetic properties of these building blocks can be easily tuned by changing the dopant atom or by modifying the structural orientation. The present thesis is focused on the basic science behind these clusters, clusters assembled materials and nanotubes; and is presented in several chapters.

Contents

List of Tables

List of Figures

Abbreviations

AO	**A**tomic **O**rbitals
B3LYP	**B**ecke **3**-parameter **L**ee-**Y**ang-**P**arr
BE	**B**inding **E**nergy
DFT	**D**ensity **F**unctional **T**heory
DOS	**D**ensity **O**f **S**tates
EA	**E**lectron **A**ffinities
ECP	**E**ffective **C**ore **P**otential
EE	**E**mbedding **E**nergy
FE	**F**ragmentation **E**nergy
GGA	**G**eneralized **G**radient **A**pproximation
HOMO	**H**ighest **O**ccupied **M**olecular **O**rbital
IP	**I**onization **P**otential
IR	**I**nfrared
LANL2DZ	**L**os **A**lamos **N**ational **L**aboratory **2** **D**ouble **Z**eta
LDA	**L**ocal **D**ensity **A**ppoximation
LUMO	**L**owest **U**noccupied **M**olecular **O**rbital
MO	**M**olecular **O**rbital
PBE	semi-local functional due to **P**erdew, **B**urke and **E**rnzerhof
PBE0	**PBE**-based **0**-parameter hybrid functional by Adamo and Barone
RHF	**R**estricted **H**artree-**F**ock method
SCF	**S**elf-**C**onsistent **F**ield
TM	**T**ransition **M**etal
WW	**W**igner-**W**itmer

Chapter 1

Introduction

1.1 Atomic clusters

Clusters are generally aggregates of atoms and molecules intermediate in size range between the bulk matter and the individual atoms or molecules. Clusters can be classified as small, medium and large-sized depending upon the number of constituent atoms or molecules. Small clusters are those whose "properties" vary abruptly as we change their sizes, shapes and compositions because of their thermodynamic and chemical instabilities. Hence, their properties are not a smooth variation as a function of size. However, these "properties" vary comparatively smoothly with the increase of the number of component atoms, where the significant finite size effects is lesser. These clusters are called medium-sized or large clusters. It is worth to mention here that the experimentally verified quantum dots are within the size range of 2 to 10 nanometers having typically 100 to 100,000 atoms. Clusters can be homogeneous (made of one kind of atom or molecule) or can be heterogeneous (composed of more than one kind). Clusters are having their unique properties and are different from the bulk and the constituent individual atoms or molecules[1]. As compared to bulk materials, clusters are having a very large surface to volume ratio, which means a large fraction of the constituent particles lie on the surface. This makes surface chemistry of the clusters extremely important in determining their properties. In a particular size and composition there may be more then one isomer and the number of isomers in a particular size increases exponentially with the increase of the number of constituent atoms or molecules. Consequently, the number of local minima in the potential energy surface increases exponentially with the number of atoms in the cluster. So, it is a challenging

job in the computational material science to identify the most stable isomer with global minima in the potential energy surface. The "most stable isomer" in a particular size and composition depends upon the geometrical point group symmetry, its physical and chemical properties. It is also possible to obtained a number of isomers with different structures and point group symmetries in a particular size in addition to the "most stable" or "ground state" isomer. Not only the structure, but the most of the properties like average binding energy, relative stability, HOMO-LUMO gap, magnetic properties and hybridizations also depend sharply on the number of atoms and the structural orientation of the cluster.

1.2 Why semiconductor clusters?

In the field of computational materials the cluster science is currently one of the most active and evolving fields of research with potential applications in science and engineering. As mentioned earlier, clusters and cluster assembled materials bridges the domains of atomic and molecular physics with the condensed matter physics. The cluster properties are dominated by their large surface-to-volume ratio, providing a unique opportunity to study the relationship between surface and volume effects. Clusters exhibit discrete spectroscopy because of their finite size. In the following section, we enumerate some of the specific questions which are under investigation from the fundamental view point.

- How the shell closing model plays an important role in cluster stabilization?
  For TM doped Si/Ge clusters, single TM atom is generally hold its unique properties and spread it over the surface of the host clusters. Shell model[2] initially applied on metal clusters and now it is also important to explain the stability of the hybrid semiconductor clusters. Hence, in the thesis we extensively used shell closing model to explain the TM doped Si/Ge clusters stabilities.

- How the quenching of magnetic moment of the TM atom take place in the semiconductor cluster?
  Usually the stability of the hybrid cluster is in expanse of the magnetic moment of the doped atom. This is because of strong hybridization between the Ge s and p orbitals with d-orbitals of the TM atom. However, in some cases the TM can hold the magnetic moment in addition to the high stability of the system. So,

it is interesting to study how the magnetic moment of the TM quenches in the semiconductor cluster due to the hybridization.

- Why cluster assembled materials?

  Cluster assembled material is the combination of the stable clusters in a bigger size, where the basic property of the assembled materials most of the times influenced by the base unit clusters. Usually, these clusters are relatively small in size and hence reactive because of its surface to volume ratio. This can be over come by increasing the volume in the assembled materials. The assembled materials are also useful for device applications. Since the clusters properties are very sensitive to its size, shape and composition, it is easy to tune their property as per the demand of technological applications and therefore this is also possible in cluster assembled materials.

- How to find out the preferable sites in the cluster to add another unit to prepare a assembled material?

  There are certain ways to explore the possibilities to design new materials. The most popular way is to use the small clusters as building blocks and assembled them one-by-one based on the symmetry sites of the clusters. Calculation of Fukui function of the cluster sites plays an important role to understand/select the probable cluster sites available for making cluster assembled materials.

1.3 Cluster magnetism

Cluster magnetism is sensitive to many factors, such as, the symmetry of the cluster, hybridization and different types of magnetic coupling between the atoms that depends upon their interatomic distances. These characteristics are interrelated. Let us consider the case of free transition metal atoms. The TM atoms Cr, Mn, Fe are having 6, 7 and 8 valence electrons, respectively and are distributed in the 3d and 4s shells. Hund's rules[3] require the spin to be a maximum and this leads to electronic configurations $3d^5\uparrow\ 3d^0\downarrow\ 4s^1\uparrow$ for Cr, and $3d^5\uparrow\ 3d^0\downarrow\ 4s^2$ for Mn and $3d^5\uparrow\ 3d^1\downarrow\ 4s^2$ for Fe, where the 3d↑ and 3d↓ subshells are separated by the exchange interaction. Since the spin magnetic moment of an electron is 1 μ_B, and the TM atoms mentioned above are having non-zero spins, the atoms possess substantial magnetic moments. The magnetic moment is given by the difference in the number of spin ↑ and spin ↓ 3d electrons per atom, which is $n_d(\uparrow) - n_d(\downarrow)$

= 5, 5 and 4 for Cr, Mn and Fe respectively. Since 4s electrons is also contributing in magnetic moment of Cr, the total redistribution of spin magnetic moments are 6, 5 and 4 for Cr, Mn and Fe respectively. In the atomic cluster, the overlap between the atomic orbitals of atoms gives rise to energy bands. The levels corresponding to 4s electrons produce a free electron-like band, while the d electrons stay localized on the atomic sites. The crystal potential stabilizes the d and s states by different amounts. However, the behavior of the Cr is different from Mn and Fe: (a) as a free atom and also (b) as a molecule in a cluster or in bulk. In the molecular orbital of Cr in cluster or in bulk, one of the 3d electron pushed up to 4s state.

Together with the crystal field potential, spd hybridization leads to charge transfer from s to d states. Assuming that the 3d orbitals are atomic-like, the Hund's rules[3] require the majority 3d↑ sub-band to be almost fully occupied with four and five electrons per atom while the minority 3d↓ sub-band has zero, zero and one electrons per atom in Cr, Mn and Fe, respectively. The difference in the number of spin ↑ and spin ↓ 3d electrons per atom is $n_d(\uparrow)$ - $n_d(\downarrow)$ = 5, 5 and 4 for Cr, Mn and Fe respectively; and the corresponding magnetic moments per atom are $6\mu_B$, $5\mu_B$ and $4\mu_B$ for Cr, Mn and Fe respectively. These magnetic moments may be different in cluster and bulk depending upon the composition and size. Hence, it depends upon the type of hybridization.

1.4 Literature review

1.4.1 Electronic shell structure

In 1984, Knight et al.[4] measured the mass abundance spectrum of Na_n clusters which showed a non-monotonic behavior with respect to the size (n) of the clusters. It was found that there was a sharp drops in the intensity just after n=8, 20, 40, and 58 as shown in Fig. 1.1. In the mass abundance spectrum of the cluster in gas phase, intensity peaks indicate the greater stability of these clusters with respect to their neighbors. Thus, Na_n clusters at n=8, 20, 40, 58 are more stable and these numbers are called magic numbers. These magic clusters are also observed in experiments on various other simple metal and noble metal clusters[2].

Origin of the enhanced stability at certain sizes can be understood in terms of simple quantum mechanical models. The common assumption of all these models is that the valence electrons of all the metal atoms move freely within a finite region

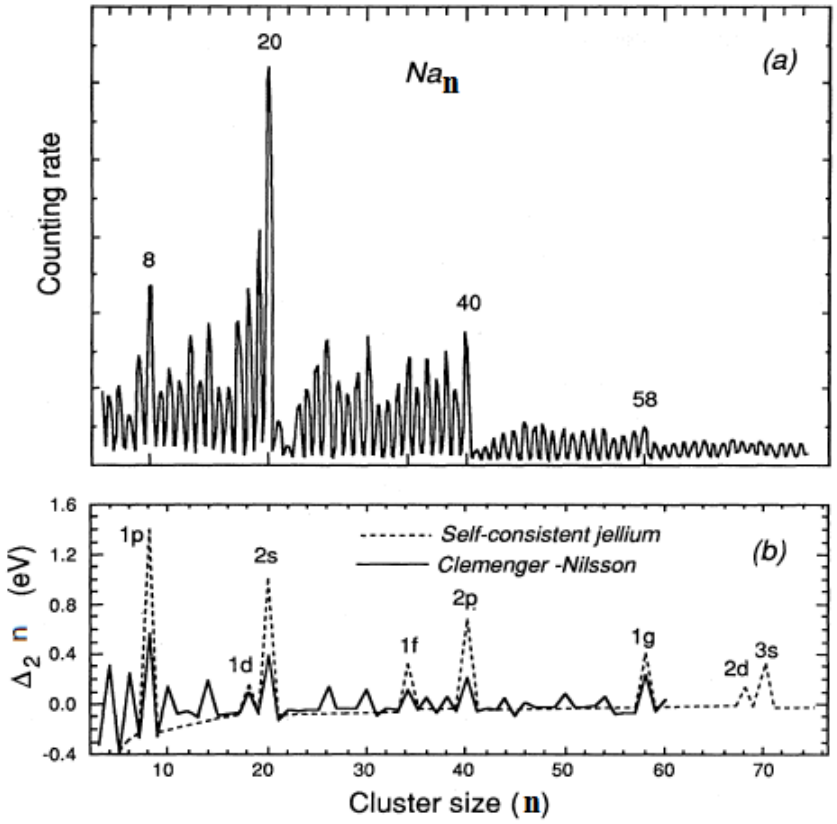

Figure 1.1: Sodium cluster abundance spectrum: (a) experimental (b) dashed line, using Woods-Saxon potential (after Knight et at.[4]); solid line, using the ellipsoidal shell (Clemenger-Nilsson) model[2]

of space defined by the "volume" of the cluster. Depending on the symmetry of the confining potential, quantum confinement leads to discrete electronic energy levels with degeneracies. These simple quantum mechanical shell models provide us with an elegant electron counting rule through which we can understand the electronic and chemical stabilities of atomic clusters.

1.4.1.1 Spherical Shell Model

In the spherical shell model[2], as the name suggests, the potential confining the valence electrons is assumed to be spherically symmetric. The radius of the confining sphere R_0 is taken as

$$R_0 = xN^{1/3}r_s \tag{1.1}$$

where, r_s is the Wigner-Seitz radius in the corresponding bulk and x is the valence of the metal atom. In the simplest picture of these models, the valence electrons experience a

potential V($\overrightarrow{r}$) which is given by

$$\begin{aligned} V(\overrightarrow{r}) &= 0; r < R_0 \\ &= \infty; r \geq R_0 \end{aligned} \tag{1.2}$$

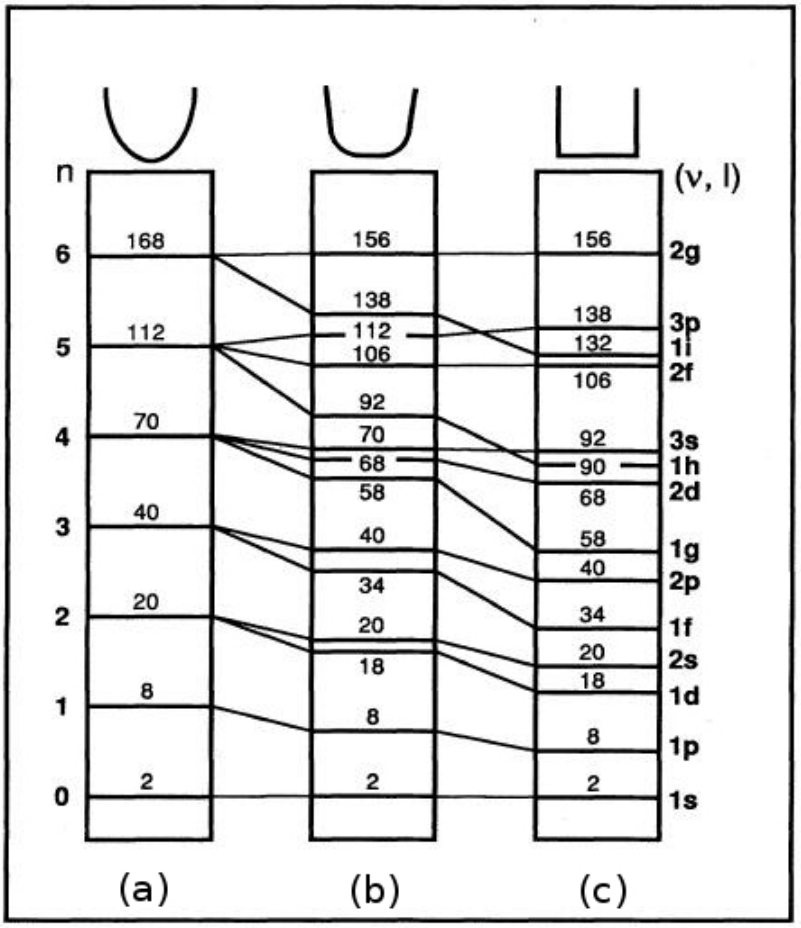

Figure 1.2: Energy-level occupations for spherical three-dimensional, harmonic, intermediate, and square-well potentials [2]

Since the valence electrons feel an infinite potential at the boundary, this model can be termed as the "hard sphere" model. By solving the Schrodinger equation, one can obtain the one-electron energy levels E_{nl} following this model as:

$$E_{nl} = \frac{\hbar^2 \beta_{nl}^2}{2mR_o^2} \tag{1.3}$$

where β_{nl} is the n^{th} order zero of the spherical Bessel function j_l. Since the potential has spherical symmetry, energy eigenstates are also angular momentum eigen-states and

possess $2(2l+1)$ fold degeneracies. These energy eigenstates form the electronic shells (n, l) which are arranged in increasing energy as $1S^2$, $1P^6$, $1D^{10}$, $2S^2$, $1F^{14}$, $2P^6$, $1G^{18}$.... as shown in Fig. 1.2c. Thus, electronic shells will be completely filled when there are 2, 8, 18, 20, 34, 40, 58... electrons in the cluster. As filled electronic shells lead to greater stability in atoms, filled shell clusters are also expected to be more stable. Therefore Na_n clusters with n=8, 20, 40, 58... electrons will be more stable. Note that this model also predicts stable clusters at n=18, 34, and 68 which were not found with high intensity in the spectrum (Fig. 1.2).

1.4.1.2 Clemenger-Nilsson shell model

Though the shell model discussed in the previous section are quite successful in explaining the relative stability of magic clusters, but it is not able to explain the fine structure of the mass abundance spectrum. This is a consequence of the assumed spherical shape of the clusters. Indeed, shape of an open shell cluster does not need to be spherical. To explain the fine structure of the mass spectrum, Clemenger proposed a model based on the ideas of Nilsson model. This model is known as Clemenger-Nilsson shell model[5]. The basic idea is to introduce spheroidal deformations in a 3D harmonic oscillator confining potential. In spheroidal deformations, two semi-axes (R_x) and (R_y) are taken equal and the third (R_z) could be different, with the constraint that the volume of the cluster remains unchanged. This constraint is imposed through the condition

$$R_x R_y R_z = R^3 \tag{1.4}$$

1.4.1.3 Jellium model

Jellium model[6] is a more realistic model as compared to the shell model discussed because the jellium model includes coulomb interaction among the valence electrons. However, the discrete nature of the ionic cores are neglected and the entire positive charge is uniformly distributed over the spherical shape of a cluster of radius R_0 as a static background having density $n_+(\vec{r})$. Positive charge density $n_+(\vec{r})$ is given by

$$n_+(\vec{r}) = n_0^+ \theta(R_0 - r) \tag{1.5}$$

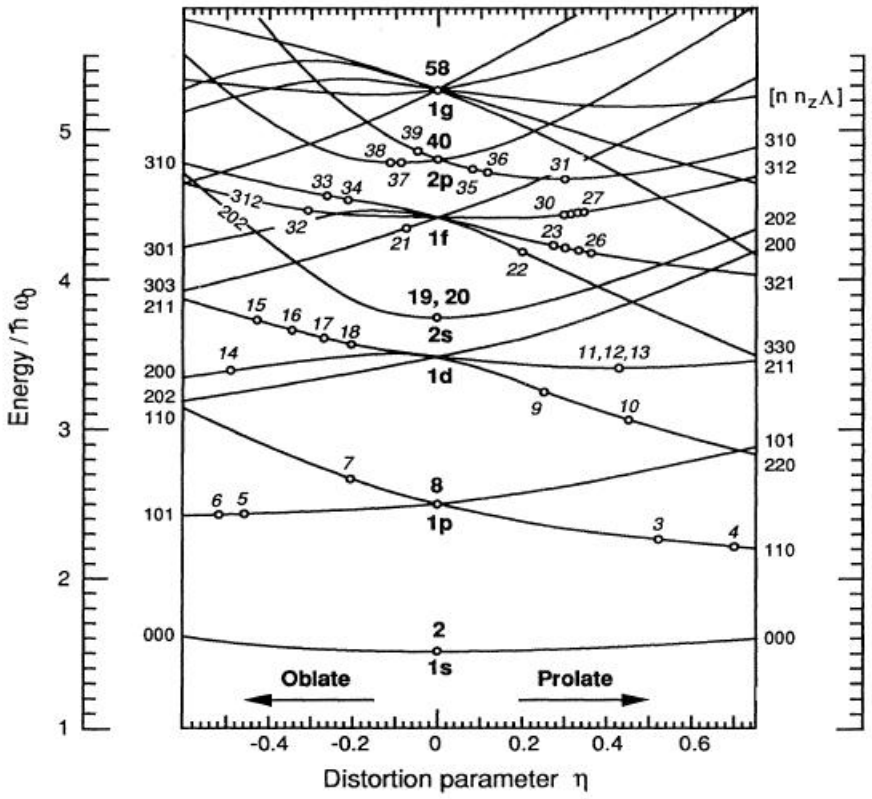

Figure 1.3: Total electronic energy curves as functions of for the 3D harmonic potential. Open circles denote the optimal values for the valence electron counts given next to the circles[2]

while $\theta(R_0 - r)$ is the step function, and has value 1 for $r \leq R_0$ and 0 for $r > R_0$. The radius of the cluster is given by Eq. 1.4. Uniform positive charge density of the background yields an attractive potential for valence electrons

$$V(\vec{r}) = -\int \frac{n_+(\vec{r})}{|\vec{r} - \vec{r}|} d^3\vec{r} \tag{1.6}$$

Chou et al.[7] used density functional theory (DFT) within the local density approximation (LDA) to calculate the ground state of interacting electrons subject to this potential. They obtained a closed electronic shell for the Na_{40} cluster with electronic configuration $1S^2$, $1P^6$, $1D^{10}$, $2S^2$, $1F^{14}$, $2P^6$, $1G^{18}$ as in the shell model. Similar to shell model, the jellium model[6] is also very successful in explaining the magic numbers of molecular system. However, it does not explain the fine structure of the mass abundance spectrum. But one can relax the constraint of spherical shape of the background charge distribution and allow deformations as done in the Clemenger-Nilsson model[5]. Hence, the fine structure in the mass abundance spectrum is captured[8,9].

1.4.2 Semiconductor clusters

The physical properties for the clusters of group 14 elements such as Si, Ge, and Sn have been the subject of intensive studies for the last decade because of their importance both in fundamental and applied sciences. In this section, we will discus about the theoretical and experimental aspect of pure Si and Ge cluster. In Fig. 1.4, the experimental setup for the photoionization threshold measurement with a vacuum ultraviolet (VUV) laser light has shown.

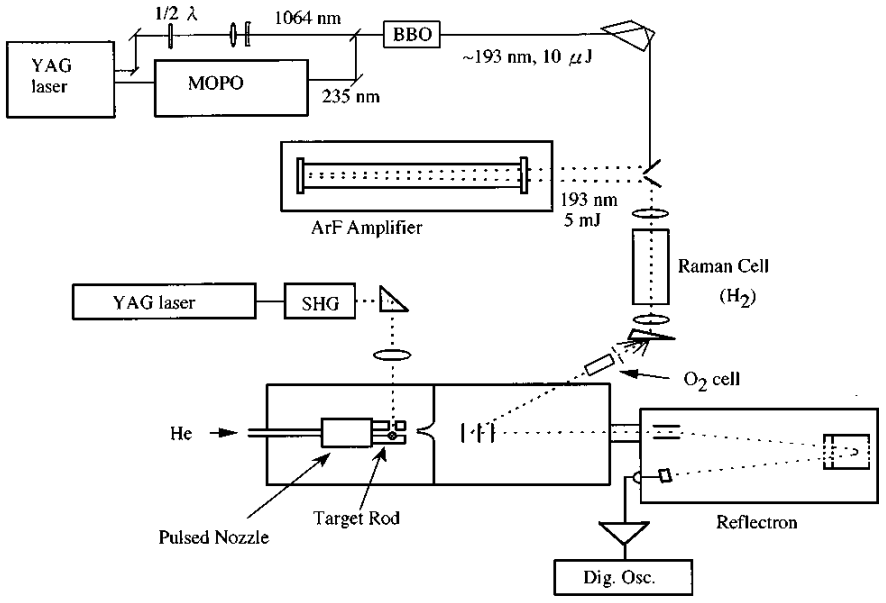

Figure 1.4: Experimental setup for ionization threshold measurement in the vacuum ultraviolet region[10].

The result is shown in Fig. 1.5 that the photoionization mass spectra for pure Ge_n clusters exhibits most stable cluster at n=10.

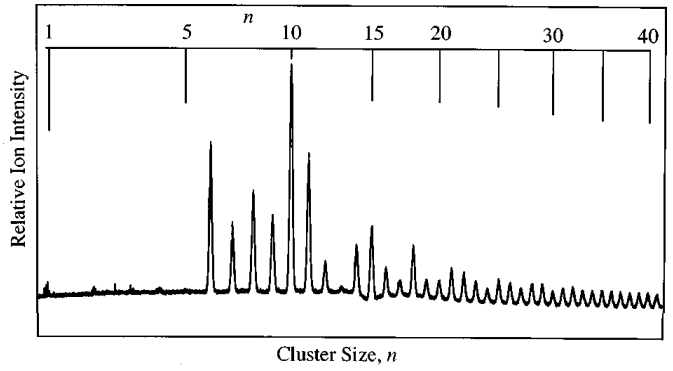

Figure 1.5: Typical photoionization mass spectra of germanium clusters, Ge_n (n=1 – 41)[10]

1.4.3 Role of TM doping in semiconductor clusters

In past few decades, extensive studies on transition metal doped semiconductor nanoclusters[11–23] and their realizations in the laboratory[24–29] have done. This opened up a new avenues to develop different silicon and germanium nano-structures. Study of the effect of different types of doping on the geometric structures of low energy semiconductor nanoclusters along with a search for their growth pattern have been reported[11–23].

Table 1.1: List of works done in literature on TM doped Si clusters. Abbreviations: QC= Quantum chemistry methods, DFT=Density Functional Theory, BE=Binding Energy, EBE=Electron Binding Energy, EE= Embedded Energy, FE=Fragmentation Energy, EA=Electron Affinity, HL=HOMO-LUMO gap, Freq=Frequencies, VIP=Vertical Ionization Potential, VDE=Vertical Detachment Energy, ADE= Adiabatic Detachment Energy, MM=Magnetic Moment, MC=Mullikan Charge, Exp=Experimental Work, NEC= Natural electronic configuration, NICS=Nucleus Independent Chemical Shifts, ELF=Electron Localization Function.

Authors	Doped Atom	Base cluster	Methods	Properties studied
Wang et al.[11]	Co	Si	DFT	BE,HL, VIP, MM
Han et al.[12]	Cr,Mo,W	Si	DFT	MC, IP
Xiao et al. [13]	Cu	Si	DFT	BE,EE,FE
Mahtout et al. [14]	Fe	Si	DFT	BE,HL,MM
Kumar et al. [15]	Ti,Zr,Hf	Si	DFT	BE,IP,EA,HL
Kumar et al. [16]	Ti,Zr	Si	DFT	Freq,HL
Koyasu et al. [17]	Sc,Y,Lu,Ti,Zr Hf,V,Nb,Ta	Si	Exp.	
Chuang et al. [18]	Ag	Si	DFT	HL,BE,FE
Zhao et al. [19]	Eu	Si	DFT	HL,BE,VIP,MC,MM
Liu et al. [20]	Gd	Si	DFT	HL,BE,VIP,EA,MM
Zhao et al. [21]	Rh	Si	DFT	HL,BE,FE,MM
Abreu et al. [22]	Cr	Si	DFT	BE,FE,EE,IP,HL
Abreu et al. [23]	W	Si	DFT	FE,IP,ADE,VDE,HL
Li et al. [30]	Nb	Si	DFT,Exp.	BE,HL,FrEq.
Li et al. [31]	Co	Si	DFT,Exp.	FrEq.
Li et al. [32]	Ag,Cu	Si	DFT,Exp.	FrEq.
Chauhan et al. [33]	Fe	Si	DFT	BE,FE,EE,IP,DE,HL
Goicoechea et al. [34]	Sc-Zn,Y-Cd	Si,Ge	DFT	
Furuse et al. [28]	Ti,Zr,Hf	Si,Ge,Sn,Pb	DFT,Exp.	Freq,NICS,EBE
Kumar et al. [35]	Cr,Mo,W	Si	DFT	BE,EE,HL
Guo et al. [36]	Sc-Zn	Si	DFT	BE,EE,VIP,HL,MM
Kawamura et al. [37]	Cr	Si	DFT	BE,EA,IP,Freq
Guo et al. [36]	Sc-Zn	Si	DFT	BE,EA,IP,Freq
Khanna et al. [38]	Fe	Si	DFT	BE,FE,VIP,HL
Neukermans et al.[27]	Cr,Mn,Cu,Zn	Si,Ge,Sn,Pb	Exp.	
Koyasu et al.[39]	Sc,Ti,V	Si	Exp.	
Kong et al. [40]	Cr	Si	DFT,Exp.	VDE,ADE,MC
Zheng et al. [41]	Cr	Si	Exp.	EBE

Table 1.2: List of works done in literature on TM doped Ge clusters. Abbreviations: QC= Quantum chemistry methods, DFT=Density Functional Theory, BE=Binding Energy, EBE=Electron Binding Energy, EE= Embedded Energy, FE=Fragmentation Energy, EA=Electron Affinity, HL=HOMO-LUMO gap, Freq=Frequencies, VIP=Vertical Ionization Potential, VDE=Vertical Detachment Energy, ADE= Adiabatic Detachment Energy, MM=Magnetic Moment, MC=Mullikan Charge, Exp=Experimental Work, NEC= Natural electronic configuration, NICS=Nucleus Independent Chemical Shifts, ELF=Electron Localization Function.

Authors	Doped Atom	Base cluster	Methods	Properties studied
Bandyopadhyay [42]	Cu	Ge	DFT	BE,FE,EE,IP,EA,MC
Wang et al. [43]	Mn	Ge	DFT	BE,HL,VIP,MM
Zhao et al. [44]	Fe	Ge	DFT	BE,FE,HL,MM
Deng et al. [45]	Ti	Ge	DFT,Exp.	EBE,VDE,ADE
Kapila et al. [46]	Mn,Co,Ni	Ge	DFT	BE,HL,MC
Zhao et al. [47]	Mn	Ge	DFT	BE,HL,MC,MM
Mahtout et al. [48]	Cr	Ge	DFT	BE,VIP,EA,HL
Wang et al. [49]	Ni	Ge	DFT	BE,FE
Jin et al. [50]	Ru	Ge	DFT	BE,MC,HL
Wang et al. [51]	Zn	Ge	DFT	Freq,HL,MC,BE,FE
Trivedi et al.[52]	Mo	Ge	DFT	BE,FE,EE,NEC,NICS
Hou et al. [53]	Cr	Ge	DFT	BE,FE,ELF
Goicoechea et al. [34]	Sc-Zn,Y-Cd	Si,Ge	DFT	MM
Deng et al. [24]	Co	Ge	DFT,Exp.	EBE,VDE,ADE,MM
Quintero et al. [26]	Ru	Ge	DFT,Exp.	
Deng et al. [25]	V	Ge	DFT,Exp.	EBE,ADE,VDE,MM
Quintero et al. [26]	Rh	Ge	DFT,Exp.	MC
Wang et al. [54]	W	Ge	DFT	BE,FE,Freq,HL
Neukermans et al.[27]	Cr,Mn,Cu,Zn	Si,Ge,Sn,Pb	Exp.	
Furuse et al. [28]	Ti,Zr,Hf	Si,Ge,Sn,Pb	DFT,Exp.	Freq,NICS,EBE
Atobe et al. [29]	Sc-V,Y-Nb	Ge,Sn	DFT,Exp.	EBE

1.4.3.1 Multiple TM doped Si/Ge clusters

Till today, most of the experimental and theoretical studies are focused on TM doped silicon clusters. However, less attention have been made on silicon clusters with multiple TM doping.

Ji and Luo[65] investigated the geometries, magnetic properties and stabilities of a number of TM_2Si_{18} (TM = Ti, V, Cr, Mn, Fe, Co, Ni, Cu or Zn) clusters using DFT calculations. They found that the magnetic moments of the TM atoms in these clusters are quenched, most of the cases except Mn_2Si_{18}, Fe_2Si_{18} and Cu_2Si_{18} with the moment of $2\mu_B$. A spin moment of $2\mu_B$ is also found in a hydrogenated $Cr_2Si_{18}H_{12}$ cluster[66]. Xu et al.[67–69] used photoelectron spectroscopy and DFT to reveal strong V–V interaction and weak Sc–Sc interaction in the V_2Si_n and Sc_2Si_n clusters respectively.

Table 1.3: List of works done in literature on multiple TM doped Si/Ge clusters. Abbreviations: DFT=Density Functional Theory, BE=Binding Energy, EBE=Electron Binding Energy, FE=Fragmentation Energy, EA=Electron Affinity, HL=HOMO-LUMO gap, Freq=Frequencies, VIP=Vertical Ionization Potential, VDE=Vertical Detachment Energy, MM=Magnetic Moment, Exp=Experimental Work, NEC= Natural electronic configuration,Pol=polarizability.

Authors	Doped Atom	Base cluster	Methods	Properties studied
Jin et al. [55]	Co_2	Ge	DFT,Exp.	
Zhang et al. [56]	Rh_2	Si	DFT	BE,HL,Freq,NEC,VIP,VEA
Zhao et al. [57]	Pd_2	Si	DFT	BE,FE,HL
Shao et al. [58]	Cu_2	Si	DFT	BE,FE,HL,Freq
Zhang et al. [59]	Rh_2	Si	DFT	BE,HL,Freq,NEC
Yang et al. [60]	Ag_2	Si	DFT	BE,FE,HL,Freq,VIP,
Ji et al. [61]	Pd_2	Si	DFT	BE,FE,HL,Pol
Han et al. [62]	Mo_2	Si	DFT	BE,FE,HL,NEC
Huang et al. [63]	V,V_2,V_3	Si	DFT	EBE,MM
Xia et al. [64]	Cu_m	$Si_n(2\leq m+n\leq 7)$	DFT	BE,FE,VIP,EA,HL

1.4.4 Functionalized cluster assembled materials

Assembling the small clusters building blocks into one assembled material structure is the key problem in chemistry and material science to design new materials. The possibility of building homo- and heterogeneous aggregations of MSi_{16} clusters for different metal dopants TM has been theoretically investigated by Balbas et al.[70] and Nakajima et al.[71]. Robles and Khanna[72] reported that the assemblies of $CrSi_{12}$ clusters may have a net spin moment. Willand et al.[73] reported that $TMSi_{20}$ clusters do not form cage-like structures at all as the Si utilizes its coordination through strong TM-Si interaction. This suggests that a carefully reduction of hydrogenation (and, therefore, increase of the amount of unsaturated Si bonds) might be used to control the number of bonding sites offered by the cluster available for reaction. As long as this does change the structural integrity of the cage, such a strategy would lead to a toolbox of monomers with differing number of "docking sites", that may offer the possibility to build network architectures of any morphology.

Assembling functionalized materials offer the ability to tune component properties, lattice parameters, and thus coupling of physical properties through the careful selection and assembly of building blocks[1]. Hybrid clusters have been found to exhibit physical properties beyond those available from the standard elements in the periodic table; classification of the properties of such clusters effectively enables expansion of the periodic table to a third dimension. Using clusters as superatomic building blocks

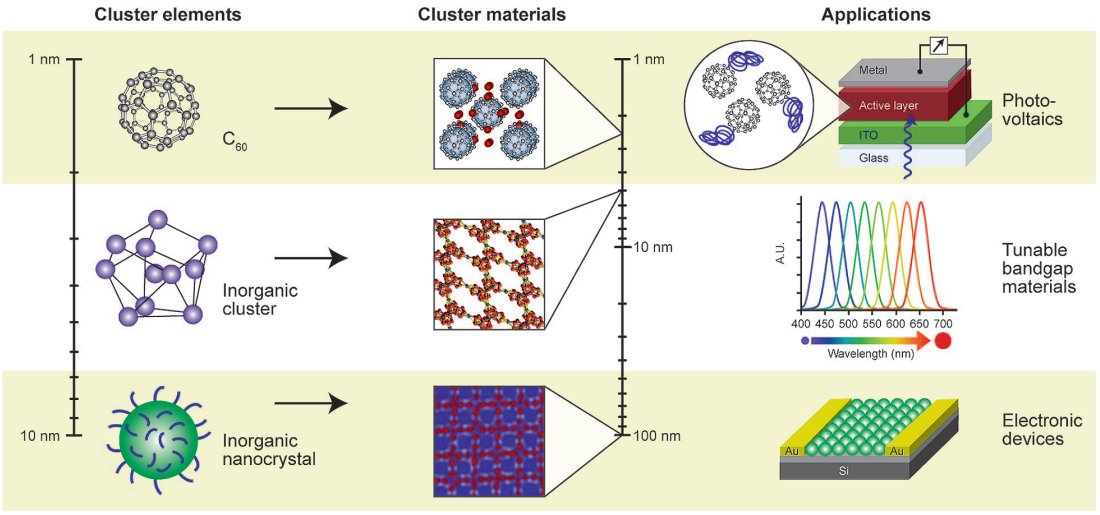

Figure 1.6: Schematic representation to understand the size, nature and application part of the cluster and cluster-assembled materials [1]

for hierarchically assembled materials allows these properties to be incorporated into designer materials with tailored properties.

Since pure and doped Si and Ge clusters have their own properties, but the obvious question aeries about their ability to design the assemblies using these clusters. As mentioned earlier, clusters which have symmetries but at the same times having dangling bonds, are the suitable candidate to make a stable assembled material. There are various reports available on these kind of cluster assembled materials which are identified and synthesized [74–81].

1.5 Goal of the thesis

The major part of the thesis work has been devoted to study the electronic structure and properties of the TM doped silicon and germanium clusters. We conducted a systematic step-by-step investigation of the electronic, magnetic, physical and chemical properties of transition metal doped semiconductor at synthetically feasible nanometer-scale. The thesis has been structured into four major parts as follows:

Part I of the thesis is divided into 2 chapters. In *Part I*, a concise introduction to different methodologies employed and concepts to explore the configurational space have been thoroughly described. In *Chapter 1*, we have reviewed the literature on the pure and TM doped Si/Ge nanocluster. The concept of shell models related to the clusters is explained. Also, the cluster assembled material is discussed. *Chapter 2* includes the introduction and explanation of all the methodology employed in the computational

calculations mentioned in the chapters. Density functional theory has been reviewed. A small introduction on psudo-potential and basis sets have also been given.

The *Part II* of thesis work has been divided into three different chapters. All the results obtained for 3d transition metal especially Ni and Cr doped Ge_n cage-like clusters are grouped together and presented in a systematic way to understand the nature of bonding within the TM doped Germanium clusters. The stability of such clusters have been explained by the energetics and the chemical bonding between the dopant and the host atoms. We have seen that the shell closure number also plays an important role in the structure stabilization. This also explains the adaptive capability of the TM-Ge bonding, which is more as the result of a complex hybridization than the originally proposed mere formal charge transfer. In *Chapter 3* and *Chapter 4*, we have checked the possibility of creating cage structures with minimized TM-Ge interaction to preserve unique atomic properties of the dopant TM atom. In *Chapter 5*, all the results obtained from 5d-Au doped Ge_n cluster are discussed.

Part III of the thesis (*Chapter 6*) explores the possibility to prepare functionalized assembled materials. We have used bottom-up approach to determine big sized structures. Initially, we have discussed the geometric and electronic structure of TMSin clusters with Cr, Mn and Fe dopant atoms. In the later part, we picked few sizes and connected them as the building blocks with different structural orientations. We have examined the stabilities of these building blocks by the addition of small cluster units and finally prepared finite Si-nanotubes. In such finite nanotubes, it is found that the atomic character of the dopant atoms is conserved. Inspired by these results, we have modeled infinite TM doped Si infinite nanotubes and discussed their electronic and magnetic properties. Interestingly, we found that these engineered functionalized magnetic nanotube's band gap properties could be easily tuned by the changing the TM atoms or their structural orientation.

In *Part IV* (*Chapter 7*) of the thesis, we focus on ongoing developments in cluster science. We discuss our future plan which is to go beyond the conventional scope in this field. We have discussed the possibility to find catalytic properties of late 5d- TM atom doped Si/Ge cluster. We also have discussed the possibility of multi-doping in Si and Ge clusters in order to achieve high spin states beyond the single-dopant atom which has been reported as a potential future plan. We can explore further on conserving both, the structural integrity of the host cage and the high spin state of the guest dimer dopant, thereby exceeding the magnetic moment. Moreover, the possibility of increasing

the cluster spin state further by encapsulating a different number of dopant atoms into a suitably sized Si/Ge cage could be quite interesting. This multiple doping phenomena could be also used in functionalized assembled materials. These developments indicate many potential future applications beyond the specific problem of doped semiconductor clusters.

Chapter 2

Methodology

2.1 Theoretical Basis of Quantum Chemistry Calculations

Quantum mechanically, to study all the physical properties of any system, basic equation given by Schrödinger[82] can be used. This time dependent Schrödinger equation yields a wavefunction ψ and moving potential V, given as:

$$\left(-\frac{\hbar^2}{2m}\nabla^2 + \hat{V}\right)\psi(\vec{r},t) = i\hbar\frac{\partial\psi(\vec{r},t)}{\partial t} \tag{2.1}$$

where ψ is a wavefunction, $\vec{r}$ - position vector, t - time, ∇^2- Laplacian, $\hat{V}$ - potential energy operator, and $\hbar$ - Planck constant divided by 2π. In the Eq. 2.1, left hand side term can be written in form of Hamiltonian operator, which a sum of kinetic and potential energy operators.

$$\hat{H} = \left[-\frac{\hbar^2}{2m}\nabla^2 + \hat{V}\right] \tag{2.2}$$

i.e. it is a sum of kinetic and potential energy operators. The stationary Schrödinger equation is a first-order differential equation:

$$\hat{H}_{tot}\psi_{tot} = E_{tot}\psi_{tot} \tag{2.3}$$

where E_{tot} and ψ_{tot} are eigenvalue and eigenfunction of the Hamiltonian, respectively.

We may write the non-relativistic Hamiltonian($\hat{H}$) for the ith electron with Ath nucleus in a molecule in atomic units (energy in Hartree and length in Bohr) as:

$$\hat{H} = -\frac{1}{2}\sum_{i=1}^{N}\nabla_i^2 - \frac{1}{2M_A}\sum_{A=1}^{M}\nabla_A^2 - \sum_{i=1}^{N}\sum_{A=1}^{M}\frac{Z_A}{r_{iA}} + \sum_{i=1}^{N}\sum_{j>i}^{N}\frac{1}{r_{ij}} + \sum_{A=1}^{M}\sum_{B>A}^{M}\frac{Z_A Z_B}{R_{AB}} \tag{2.4}$$

In the above equation, M_A is the ratio of the mass of nucleus A to the mass of an electron and Z_A is the atomic number of nucleus A. The ∇_i^2 and ∇_A^2 are the Laplacian operators. The first two terms in Eq. 2.4 are for the kinetic energy of the electrons and nuclei, respectively. The third term represents the Coulomb attraction between electrons and nuclei. The fourth and fifth terms represent the repulsion between electrons and between nuclei, respectively.

2.1.1 Born-Oppenheimer approximation

The Hamiltonian consists of five terms: kinetic energy of electrons $\hat{T}_e$, kinetic energy of nuclei $\hat{T}_n$, potential energy of electron-electron interaction $\hat{V}_{ee}$, potential energy of nuclei interaction $\hat{V}_{nn}$, and potential energy of electron-nucleus interaction $\hat{V}_{ne}$. We may write the non-relativistic Hamiltonian for a molecule as a sum of these five terms:

$$\hat{H} = \hat{T}_e + \hat{T}_n + \hat{V}_{ee} + \hat{V}_{nn} + \hat{V}_{ne} \tag{2.5}$$

The Born-Oppenheimer approximation[83] plays a vital role in electronic structure calculations. The underling rationalization of this approximation is that the mass of nuclei are much heavier than electrons. Thus in most cases the nuclei move much more slowly than electrons. Hence, nuclei can be consider as a fixed or not in moving state. This is the qualitative rationalization to separate the movement of electrons and nuclei. In the Born-Oppenheimer approximation the second term in Eq. 2.4 is neglected, and the final term, the repulsion between nuclei, can be treated as a constant for a fixed configuration of the nuclei. The remaining terms in Eq. 2.4 are called the electronic Hamiltonian ($\hat{H}_{ele}$),

$$\hat{H}_{ele} = -\frac{1}{2}\sum_{i=1}^{N}\nabla_i^2 - \sum_{i=1}^{N}\sum_{A=1}^{M}\frac{Z_A}{r_{iA}} + \sum_{i=1}^{N}\sum_{j>i}^{N}\frac{1}{r_{ij}} \tag{2.6}$$

Thus, the total wavefunction can be separated into two parts: an electronic part ψ_e and a nuclear part ψ_n. In this view, electrons move in a potential field created by

the nuclei, and the Schrödinger equation for the electron wavefunction ψ_e is written as follows:

$$\left(\hat{H}_e + \hat{V}_{nn}\right)\psi(\vec{r},\vec{R}) = E_e(\vec{R})\psi(\vec{r},\vec{R}) \tag{2.7}$$

where $\vec{r}$ is a position vector for electrons, $\vec{R}$ position vector for nuclei. For the material applications, the electronic wavefunction is sufficient. Thus we have $\hat{H} = \hat{V}_e + \hat{V}_{ee} + \hat{V}_{ne}$, $\psi = \psi_e$, E = E_e, and can re-write the Schrödinger equation in a simpler form:

$$\hat{H}\psi = E\psi \tag{2.8}$$

After multiplying by the complex conjugate and integrating over volume

$$\int \psi^* \hat{H}\psi d\upsilon = \int \psi^* E\psi d\upsilon, \tag{2.9}$$

a scalar value of the energy E can be found as:

$$E = \frac{\int \psi^* \hat{H}\psi d\upsilon}{\int \psi^* \psi d\upsilon} \tag{2.10}$$

In most cases, finding the exact form of the wavefunction is unfeasible. Therefore, additional approximations are introduced to simplify the calculation. Historically the first and most widely used approximation is the Hartree-Fock (HF) method[84].

2.1.2 Hartree-Fock (HF) method

In order to solve the Schrödinger equation for a multi-electron system, the approximation of non-interacting electrons is introduced. In this case the total wavefunction can be described as a product of one-electron wavefunctions. The Hamiltonian for every electron is:

$$h_i = \hat{T}_i + \sum_n \hat{V}_{ni} \tag{2.11}$$

where $\hat{T}_i$ is electron kinetic energy, and $\hat{V}_{ni}$ the potential energy of electron-nucleus interaction. Thus, the Schrödinger equation can be solved for a single-electron system $h_i\psi_i = \epsilon_i\psi_i$, where ψ_i are single-electron wavefunctions and ϵ_i the corresponding energy values. However, such a single-electron composed wavefunction does not properly describe the anti-symmetrization requirement for fermionic systems, known as Pauli

principle[85]. Slater therefore suggested to use a linear combination of single-electron spin functions in form of a determinant[86], which then describes the many-electron wavefunction with proper account for the symmetry and the Pauli principle. Such an N-electron Slater wavefunction is written as:

$$\psi = \frac{1}{\sqrt{N!}} \begin{vmatrix} \chi_1(1) & \chi_2(1) & \dots & \chi_N(1) \\ \chi_1(2) & \chi_2(2) & \dots & \chi_N(2) \\ \vdots & \vdots & \ddots & \vdots \\ \chi_1(N) & \chi_2(N) & \dots & \chi_N(N) \end{vmatrix} \tag{2.12}$$

where χ is a spin function, *i.e.* a single-electron function which accounts for spin. For the given expression of the determinant, all functions describe occupied orbitals. Within the restricted Hartree-Fock (RHF) method[87,88] all electrons are paired. Then the set of paired differential equations can be written in form of the Hartree-Fock equations $f_i\psi_i = \epsilon_i\psi_i$, where ϵ_i are the energy eigenvalues for single-electron functions ψ_i, and f_i is the Fock operator:

$$f_i = \hat{h}_i + \sum_{j=1}^{N}(J_i(1) - K_i(1)) \tag{2.13}$$

In Eq. (2.13) a summation is done over the number of electrons N. "1" means that the operator includes coordinates of one electron only. J is a Coulomb integral describing the electrostatic repulsion between electrons, K is the exchange integral.

Within the Hartree-Fock method each electron occupies its own orbital and moves within the potential field of the other N – 1 electrons. Thus, electrons can be located closer to each other than they would be, if the energy of each electron was minimized individually. Therefore, the HF method always overestimates the energy. The difference between the energy in the Hartree-Fock limit and the exact non-relativistic energy of a system is designated as correlation energy $E_{corr} = E_{exact} - E_{HF}$. Thus, the sum of single-electron energy values does not equal the total energy of the system. Electron-electron interaction is calculated twice upon summation of single-electron energies, and should be corrected through division of the full interaction by two. Then the total energy is:

$$E_{HF} = \sum \epsilon_i - \frac{1}{2}\sum_i \sum_j (J_{ij} - K_{ij}) \tag{2.14}$$

Solution of the Hartree-Fock equations yields molecular orbitals, which describe the spatial distribution of the probability of finding an electron. Each orbital corresponds to a certain energy level. Orbitals are occupied by maximum of two electrons each, starting from the energetically lowest. Occupation of N orbitals with minimal energy values then yields a minimal total energy, which corresponds to the ground state of the system. The remaining high-energy orbitals are called virtual orbitals. Especially important for chemical applications are the so-called frontier orbitals, *i.e.* the highest occupied (HOMO) and lowest unoccupied (LUMO) molecular orbitals.
Molecular orbitals (MO) filled with electrons are mathematical functions, which can be represented as linear combinations of atomic orbitals (LCAO):

$$\psi_i = \sum_{\mu} C_{\mu i}\phi_{\mu} \tag{2.15}$$

where $C_{\mu i}$ is a coefficient, ϕ_{μ} is an atomic orbital (AO). Atomic orbitals are the solutions of the Schrödinger equation for a hydrogen atom, *i.e.* the orbitals of the hydrogen atom (1s, 2s, 2p, 3s, 3p,...) The LCAO method allows constructing molecular orbitals using already known functions with only coefficients unknown. Integration over the volume gives the Roothaan equation[89]:

$$FC = SC\epsilon \tag{2.16}$$

where F is the Fock matrix, S and C are matrices with overlap integrals $S_{\mu\nu}$ and coefficients $C_{\mu\nu}$. The matrix elements are

$$\left.\begin{aligned} F_{\mu\nu} &= \int \phi_{\mu}^{*} f \phi_{\mu} dV \\ S_{\mu\nu} &= \int \phi_{\mu}^{*} \phi_{\mu} dV \end{aligned}\right\} \tag{2.17}$$

The solution of the equations can be considered as a procedure of energy minimization, where, according to the variational principle, the best wavefunction corresponds to the minimal energy. The problem can be solved iteratively, with the coefficients $C_{\mu\nu}$ found by the energy minimization. Such procedure is known as self-consistent field (SCF).

2.2 The Density Functional Theory (DFT)

One of the most common present-day computational chemistry approaches is based on the density functional theory (DFT). Within this method, the main variable of quantum mechanics, wavefunction ψ, is substituted by the electron density ρ(r), which is a function of only three spatial coordinates. The total energy, as well as any other observable property of a molecular system, can be defined through ρ(r) via so-called functionals.[†] According to the Hohenberg-Kohn theorems[92], the electron density can be considered as a variable in many-electron theory. When the ground-state electron density of a system is known, it is possible to calculate energy of the ground state and all molecular properties. The second Hohenberg-Kohn theorem states that the energy of the given configuration obeys the variational principle, and among all possible electron density distributions the one that yields the minimal energy is the ground-state density. However, the Hohenberg-Kohn theorems do not give an exact form of the E(ρ) functional needed to evaluate such a minimization. The Kohn-Sham scheme[93] is currently the main procedure for the explicit calculation of electron density and energy for any atomic and molecular system, and is the basis of most present-day DFT calculations. The main goal of the Kohn-Sham method is to calculate a hypothetical system composed of N electrons, which do not interact with each other, occupy N orbitals ψ_i, and move within the potential field ν_s. For this type of systems, the Slater determinant rigorously describes the wavefunction in the ground state. Optimal orbitals for the system can be found by solving single-electron equations:

$$\left(-\frac{1}{2}\nabla^2 + \nu_s\right)\psi_i = \epsilon_i\psi_i \tag{2.18}$$

Here, the Hamiltonian consists of the kinetic energy operator and a single-particle effective potential. The total electron density is a sum of orbital densities:

$$\rho_s(\vec{r}) = \sum_{i=1}^{N} |\psi_i(\vec{r})|^2 \tag{2.19}$$

The connection of the system where there is no electron-electron interaction with the true system, where electrons do interact, can be assessed via the choice of an effective potential of one particle in such a way that the electron distribution corresponds to the

[†] For an extended discussion of Density Functional Theory see ref. [90]. For detailed derivations consult ref. [91].

density distribution of the real system in its ground state. Despite the fact that the exact expression for the density functional E(ρ) is unknown, its constituent parts can be expressed as follows:

$$E_{DFT}(\rho) = T_S(\rho) + E_{ne}(\rho) + J(\rho) + E_{XC}(\rho) \tag{2.20}$$

where ρ is the density of the system of interacting electrons. The form of the first three terms is known. $T_S(\rho)$ is the kinetic energy of the system with non-interacting electrons, $E_{ne}(\rho)$ is the potential energy of the Coulomb interaction between nuclei and electrons, and $J(\rho)$ is the energy of inter-nuclei repulsion. All other terms are accounted for in the fourth term $E_{XC}(\rho)$), the exchange-correlation functional. $E_{XC}(\rho)$ includes all non- classical interaction effects, as well as the part of kinetic energy not included in $T_S(\rho)$. The exchange-correlation functional also corrects the $J(\rho)$, which allows for a non-physical interaction of the electron with itself. Taking into account Eq. (2.19), one can rewrite the Eq. (2.20) in the following form:

$$\begin{aligned} E(\rho) = &-\frac{1}{2}\sum_{i=1}^{N}\int \psi_i^*(\vec{r})\nabla^2\psi_i^*(\vec{r})d\vec{r} - \sum_{i=1}^{N}\int\sum_{A=1}^{M}\frac{Z_A}{|R_A-\vec{r}|}\left|\psi_i(\vec{r})\right|d\vec{r} + \\ &\sum_{i=1}^{N}\sum_{j=1}^{N}\int\int\left|\psi_i(\vec{r})\right|^2\frac{1}{|\vec{r}-\vec{r}'|}\left|\psi_j(\vec{r}')\right|^2 d\vec{r}d\vec{r}' + E_{XC}(\rho) \end{aligned} \tag{2.21}$$

where M and N are the number of nuclei and electrons, respectively. The energy minimization after normalization of the wavefunction yields a set of single-electron Kohn-Sham equations:

$$\hat{h}_{KS}\psi_i = \epsilon_i\psi_i, (i = 1, 2, ...N.) \tag{2.22}$$

The single-electron operator $\hat{h}_{KS}$ contains the kinetic energy, nuclei potential, the classical Coulomb potential and the potential caused by $E_{XC}(\rho)$:

$$\hat{h}_{KS} = -\frac{1}{2}\nabla^2 - \sum_A\frac{Z_A}{|R_A-\vec{r}|} + \int\frac{\rho(\vec{r}')}{|\vec{r}-\vec{r}'|}d\vec{r}' + \nu_{XC}(\vec{r}) = -\frac{1}{2}\nabla^2 + \nu_{eff}(\vec{r}) \tag{2.23}$$

The exchange-correlation potential ν_{XC} is defined as the functional derivative of the exchange-correlation energy with respect to ρ: $\nu_{XC} = \frac{\partial E_{XC}[\rho]}{\partial\rho(\vec{r})}$. Comparison of

Eqs. (2.18), (2.22) and (2.23) reveals that if the potential of a single particle s in Eq. (2.18) is defined as $\nu_{eff}\ (\vec{r})$ in Eq. (2.23), then the system with non-interacting electrons transforms into a system where electrons do interact. Thus, the Kohn-Sham equations appear after substitution $\nu_s = \nu_{eff}\ (\vec{r})$ in Eq. (2.18), and the solution of this equation yields the Kohn-Sham orbitals. $\nu_{eff}\ (\vec{r})$ depends on the electron density, and in order to find the Kohn-Sham orbitals, Eq. (2.22) needs to be solved iteratively using the SCF procedure, just like in the HF method. The energy of the system can be obtained by inserting the electron density found from the Kohn-Sham orbitals (Eq. (2.19)) into the Eq. (2.20).

2.2.1 Exchange correlation functionals

2.2.1.1 Local density approximation (LDA)

As it has been mentioned before, the exact form of the exchange-correlation functional is unknown. Therefore, the quality of the solution obtained within the DFT framework is directly dependent on the chosen functional E_{XC} [94]. Exchange-correlation functionals can be classified according to the way the electron density distribution is described. The simplest approximation is the local density approximation (LDA), with the idea of a hypothetical uniform electron gas, where the electrons sit in an infinite region of space, with a uniform positive external potential, chosen to preserve overall charge neutrality. Then E_{XC}^{LDA} is:

$$E_{XC}^{LDA} = \int \rho(\vec{r})\epsilon_{XC}(\rho(\vec{r}))d(\vec{r}) \tag{2.24}$$

where ϵ_{XC} is a functional that depends only on the local density at each point $\vec{r}$. The exchange-correlation functional can further be divided into two parts $E_{XC} = E_X + E_C$, where E_X and E_C are functionals accounting for exchange and correlation parts of the energy, respectively. The form of the exchange part E_X for the homogeneous electron gas is known, and was originally derived by Bloch[95] and Dirac[96]. No such explicit expression is known for the correlation part E_C, however. Several authors developed their representations of E_C[97–99]. The most recent and accurate one has been suggested by Perdew and Wang[100]. These functionals can be successfully used in systems where the real density resembles the one of the uniform electron gas, e.g. in metals.

2.2.1.2 Generalized-gradient approximation (GGA)

A step forward in comparison to LDA was done in another (and probably the most widely used nowadays) method: the generalized gradient approximation (GGA). There, not only information about the density $\rho(\vec{r})$ at a particular point $\vec{r}$, but also information about the gradient of the charge density $\nabla\rho(\vec{r})$ is used in the evaluation of E_{XC}, to account for the non-homogeneity of the true electron density. The general form of the GGA exchange-correlation functional is:

$$E_{XC}^{GGA} = \int f(\rho, \nabla\rho) d\vec{r} \tag{2.25}$$

Such functionals are better suited for molecular systems, where the electron density is clearly not uniform. Several GGA functionals have been suggested[101–103], the most widely used being the PBE functional by Perdew, Burke and Ernzerhof[104]. As it is also the case for the LDA, spin-polarized versions of these functionals (for collinear treatment of spin) have been developed alongside. The DFT-GGA approach has proven to be very reliable for a wide range of applications and has served as a "workhorse" of quantum chemistry for the last twenty years.

However, GGAs still have the disadvantage of yielding only approximate exchange contributions, which result in certain problems expressing the exchange part of the energy[90]. A way to overcome these difficulties has been suggested by including a component of the exact exchange energy calculated from Hartree-Fock theory. Functionals of this type are known as hybrid functionals[105] and have the following general form:

$$E_{XC}^{hybrid} = cE_X^{HF} + (1-c)E_X^{DFT} + E_C^{DFT} \tag{2.26}$$

where the coefficient c defines the HF exchange contribution. Especially successful hybrid functionals include the empirically-parametrized B3LYP[106] and parameter-free PBE0[107].

In the present work most calculations have been carried out using the B3LYP and GGA-PBE functional.

$$\begin{aligned} E_{XC}^{B3LYP} = E_x^{LDA} + a_o(E_x^{HF} - E_x^{LDA}) + a_x(E_x^{GGA} - E_x^{LDA}) + E_c^{LDA} \\ + a_c(E_c^{GGA} - E_c^{LDA}) \end{aligned} \tag{2.27}$$

For comparison the target quantities were also systematically recomputed on the hybrid functional level with the B3LYP and PBE0 functional, without ever obtaining any qualitative changes that would conflict with the conclusions deduced from the standard PBE calculations. Considering the frequent observation that hybrid functional DFT yields results that for 3d transition metal containing systems are at least en par, if not superior to correlated wavefunction approaches[108–112], this supports the reliability of the reported results. The detailed discussion of the computational setup is given within the corresponding chapters. Of course, going beyond the accuracy of GGAs and hybrids is tempting, but more accurate electronic structure theory proves to be extremely computationally challenging when a large number of evaluations is required like in the context of global geometry optimization.

2.3 Basis sets

A basis set is a set of unknown functions through which the wavefunction is expanded. For a single electron, the wavefunction can be written as

$$\psi_i(r) = \sum_j c_j \phi_j(r) \tag{2.28}$$

where ϕ_j(r) are a complete set of functions. Any set of functions could be used as basis functions. In principle, the basis functions should have the same limiting behavior as the real wavefunction, for isolated atom or molecules they should decay to zero, and they should be computationally inexpensive.

2.3.1 Localized basis sets

The wavefunction exponentially decays to zero at large distances for isolated atoms and molecules. This means that the basis functions also should behave in a similar way. Atomic orbitals are the basis functions possessing this property and have two forms: Slater type orbitals (STO) and Gaussian type orbitals (GTO). STOs have the following form in spherical coordinates[113].

$$\phi_{STO}^{nlm\zeta}(r,\theta,\phi) = \alpha Y_{lm}(\theta,\phi) r^{n-1} e^{-\zeta r} \tag{2.29}$$

where α is a normalization constant, $Y_{lm}(\theta, \phi)$ is the spherical harmonic. l, m, and n are quantum numbers, and ζ determines the radius of the orbit. The exponential dependence on distance is the same as for the hydrogen atom.
GTOs in spherical coordinates have a form

$$\phi_{GTO}^{nlm\zeta}(r, \theta, \phi) = \alpha Y_{lm}(\theta, \phi) r^{2n-2-l} e^{-\zeta r^2} \tag{2.30}$$

In both cases the angular dependence of the wavefunction is contained in the spherical harmonics, where the l,m values determine the type of orbital (e.g. $l = 0$ is a s type orbital, $l = 1$ a p orbital, etc). The main difference between STO and GTO is the power of r in the exponent. GTOs have a zero slope at the nucleus (r = 0) whereas STOs have a cusp. GTOs also fall off more rapidly with distance than STOs. These factors suggest that more GTOs are needed to form a suitable basis set than STOs, roughly three times as many are needed to achieve the same accuracy[113]. However, GTOs are computationally more efficient than STOs: the factor r in the exponent requires taking a square root (r = $\sqrt{x^2 + y^2 + z^2}$) which is computationally very slow. This computational efficiency compensates for the additional number of functions needed, hence GTOs are more commonly used in calculations. The size of the basis set has a large effect on the accuracy of the calculation. The smallest basis set possible is the minimum basis set which contains only enough functions to contain all the electrons in the neutral atoms. Increasing the number of basis functions improves the accuracy of the calculation.

2.3.2 Plane wave basis sets

The potential for a periodic system can be explained as

$$V(r + na) = V(r) \tag{2.31}$$

where a is a lattice vector and n is an integer. From Bloch's theorem[114], the wavefunction can be written as a product of a periodic and a wave-like part, *i.e.*,

$$\psi_i(r) = e^{ik.r} \phi_i(r) \tag{2.32}$$

Because of periodicity, $f(\mathrm{r})$ can be expanded as a set of plane waves

$$\phi_i(r) = \sum_G c_i, Ge^{iG.r} \tag{2.33}$$

where G are the reciprocal lattice vectors. Substituting Eq. 2.33 in Eq. 2.32, the wave function can be written as

$$\psi_i(r) = \sum_G c_i, Ge^{i(k+G).r} \tag{2.34}$$

The number of wavefunctions used is controlled by the largest wave vector in the expansion in Eq. 2.33. This is equivalent to a cut-off on the kinetic energy since the kinetic energy of an electron with wave vector k is given by

$$E_k = \frac{\hbar^2 |k|^2}{2m} \tag{2.35}$$

Using the plane waves, the Kohn-Sham equations can be written as[115]

$$\left[\sum_{G'} \frac{\hbar^2}{2m} |k+G|^2 \delta_{GG'} + V_{en}(G-G') + V_{ee}(G-G') + V_{XC}(G-G')\right] c_{i,k+G'} = c_{i,k+G'}\varepsilon_i \tag{2.36}$$

where $V_{en}(G-G')$, $V_{ee}(G-G')$ and $V_{XC}(G-G')$ are the Fourier transforms of electron-nuclei, electron-electron, and exchange-correlation potentials.

Chapter 3

Electronic structure and stabilities of Ni doped Germanium nanoclusters

3.1 Introduction

In this chapter[†], we made an effort to explain the enhanced stability of $Ge_{10}Ni$ cluster in Ge_nNi (n=1-20) series by studying different physical and chemical properties of the theoretical ground state clusters in each size using density functional theory. In the growth pattern Ni-capped Ge_n and Ni-encapsulated Ge_n clusters are mostly appear as theoretical ground state in a particular size. To explain the relative stability of the ground state clusters, variation of different parameters like, average binding energy per atom (BE), embedding energy (EE) and fragmentation energy (FE) of the clusters are studied with the size of he cluster. To explain the chemical stability of the clusters different parameters like, energy gap between the highest occupied and lowest unoccupied molecular orbitals (HOMO-LUMO gap), ionization energy (IP), electron affinity (EA), chemical potential (μ) and chemical hardness (η), polarizability etc. are calculated and discussed. Natural bond orbital (NBO) analysis is applied to understand the electron counting rule applied in the most stable $Ge_{10}Ni$ cluster. Finally, the importance of the calculated results to design Ge-based superatoms is discussed.

[†]Kapil Dhaka, Ravi Trivedi, Debashis Bandyopadhyay, "Electronic structure and stabilities of Ni-doped germanium nanoclusters: a density functional modeling study", *J Mol Model,(2013)*, 19,1473-1488.

3.2 Computational Details

In the present theoretical work, all calculations are performed within the framework of linear combination of atomic orbitals density functional theory. The exchange-correlation potential contributions are incorporated into the calculation using the spin-polarized generalized gradient approximation (GGA) functional proposed by Lee, Yang and Parr popularly known as B3LYP[116]. Different basis sets were used for germanium and nickel with effective core potential using Gaussian'03[117] program package. The standard LanL2DZ-dp and LanL2DZ basis sets were used for germanium and nickel to express the molecular orbitals (MOs) of all atoms as linear combinations of atom-centered basis functions. LanL2DZ-dp (taken from EMSL basis set exchange library) is a double-ζ, 18-Valence electron basis set with a LANL effective core potential (ECP) and with polarization function[118]. All geometry optimizations are performed with no symmetry constraints. During optimization, it is always possible that a cluster with particular guess geometry can get trapped in a local minimum of the potential energy surface. To avoid this several initial geometries in a particular size with different spin states (singlet to quintet) are taken as input in the calculation to search for the theoretical ground-state (GS) isomer during the optimization. In order to check the validity of the applied methodology, trial calculations are carried out on Ge–Ge, Ni-Ni and Ge-Ni dimers. The calculated Ge–Ge bond length in germanium dimer at triplet spin state (ground state) is 2.44 Å (with a lowest frequency of 250 cm^{-1}). These are very close to the values obtained by several groups as shown in Table 3.1. The bond length and the lowest frequency of Ge-Ni dimer in triplet spin state (ground state) are obtained in the present calculation as 2.32 Å and 236 cm^{-1} respectively. The values reported by other groups are 2.25 Å and 239 cm^{-1} as shown in Table 3.1. The bond length of the triplet ground state Ni–Ni dimer obtained in the present method is 2.35 Å, and corresponding frequency is 232 cm^{-1}. These values are close to the values reported in literature (Table 3.1). Comparing the bond lengths and lowest frequencies of different dimers, the present method of calculation can be taken as an appropriate one for nickel doped germanium clusters. The optimized electronic structure is obtained by solving the Kohn–Sham equations self-consistently[93] using the default optimization criteria of the Gaussian'03 program[117]. The initial input geometries of the clusters used in the calculations are constructed on the basis of the reported optimized geometries[42,119,120] and also from their modified versions. With the increasing size of the clusters, the

number of isomer in a particular size increases exponentially. So it is as a challenging job to search a ground-state cluster in a particular size. Tai and Nguyen[121] adopted a stochastic search method that covers a good number of isomeric structures and increase the chance of finding the ground state geometry. To check the stabilities of the structures, a frequency check calculation of the harmonic vibrations of the clusters is also done. If any imaginary frequency was found in a particular vibrational mode, relaxation was performed along that mode until the true local minimum is obtained. Geometry optimizations are carried out to a convergence limit of 10^{-7} Hatre in the total optimized energy. The optimized geometries as well as the electronic properties of the clusters in each size are obtained from the calculated program output.

3.3 Results and discussions

3.3.1 Growth of hybrid $NiGe_n$ nanoclusters

Theoretically calculated optimized ground state structures of $NiGe_n$ clusters within the size range of n = 1-20 are shown in Fig. 3.1. In the present study a number of isomers are calculated in each size. Only selected isomers with energy close to the supposed ground state structures are presented in Figs. A.1, A.2, A.3.

It is well known that nickel is ferromagnetic material with $[Ar]3d^84s^2$ electronic configuration. Whereas, germanium has $[Ar]3d^{10}4s^24p^2$ electronic configuration. With the doped nickel atom in most of the case germanium cluster makes sp^3d^2 type of hybridization. There is a strong mixing affinity between sp- orbitals of germanium with the transition metal d- orbitals to form sp^3d^2 hybridization. When germanium atom in the stable cluster is replaced by transition metal atom or pure germanium cage is doped by transition metal atom, the doped transition metal atom absorbs the dangling bonds present on the surface of the pure germanium cages. Various studies[42,120,122–125] are shown that the metal doped cage like isomers are important because of relatively higher stability compare to the pure semiconductor clusters and also due to wide variation of electronic properties, which are useful for different applications. A bare nickel atom has a triplet spin multiplicity. Therefore, in the present calculations all $NiGe_n$ guess structures are optimized at different spin states starting from singlet to quintet until there is a drop in optimized energies to check whether the spin moment of nickel inside the cage could survive under bonding with germanium or not. It is found that the

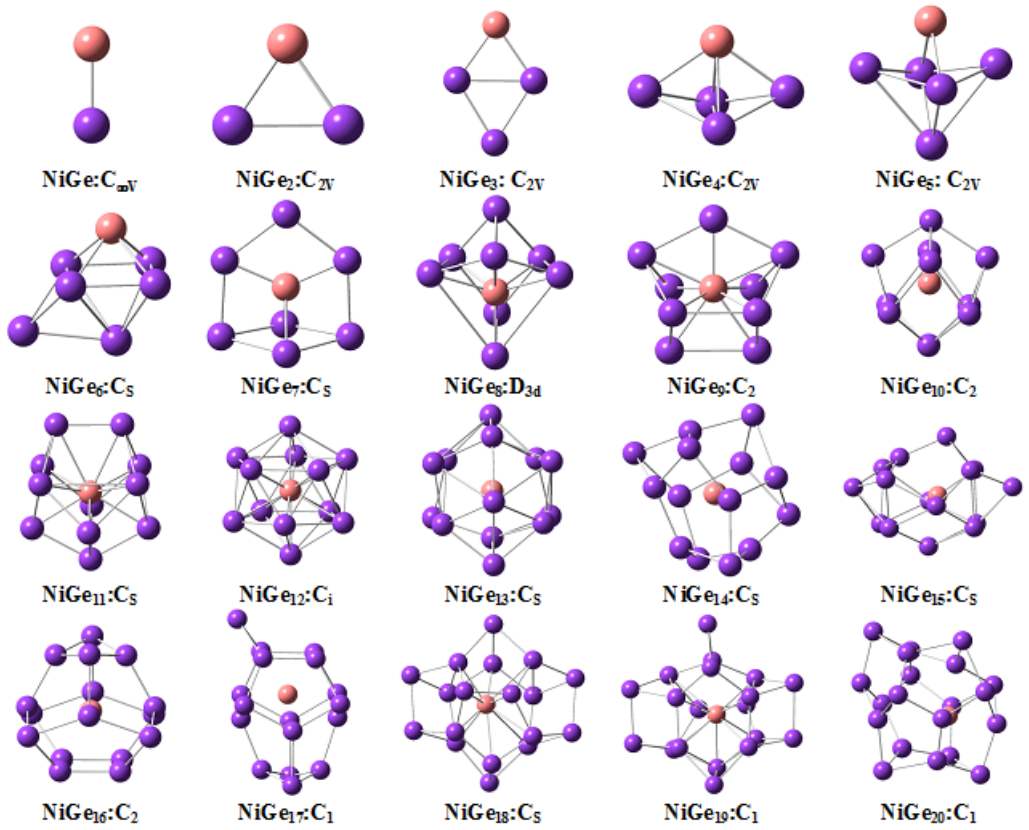

Figure 3.1: Ground state structures of Ni doped Ge_n clusters

Table 3.1: Bond length and frequency of different dimers

Dimer	Bond length (Å)	Lowest frequency (cm^1)
Ge-Ge	2.36–2.42[126–131], 2.46[132], 2.57[133], 2.44(Present work)	258 [G. Frudakis, personal communication], 250(Present work)
Ge-Ni	2.248[134], 2.32(Present work)	239[135], 236(Present work)
Ni-Ni	2.06[136], 2.155[137], 2.13[138], 2.20[139], 2.36[140], 2.35(Present work)	210±25[137], 236[140], 232(Present work)

theoretical ground state of Ge-Ni dimer with $C_{\infty v}$ point group symmetry can hold a triplet spin state as reported by Wang and Han[49] before.

The immediate next higher size also show a triplet ground state. Four different isomers are optimized at this size with the triangular isomer in C_{2v} point group symmetry as ground state. The other two structures are linear chain structures in D_{2h} and C_{2v} point group symmetry as shown in Fig. A.1. Out of the four isomers in Ge_3Ni, the isomer with triplet bend rhombus in $^1A_1$ state with C_{2v} point group symmetry is the theoretical ground state. Other isomers are two different pyramidal structures with very closely degenerate states. Seven stable isomers are found in Ge_4Ni. Out of these four

low energy isomers are presented in Fig. A.1. The Ni capped bend rhombus in $^1A_1$ electronic state with C_{2v} point group symmetry is found as the ground state. Other three structures are plane rhombus with a tail as shown in Fig. A.1. First three low energy Ge_5Ni isomers are shown in Fig. A.1 out of a number of optimized structures in this size. The optimized ground state structure (5C in Fig. A.1) in C_S full point group symmetry can be obtained by replacing one capped germanium atom by Ni in Ge_6 bi-capped pyramidal isomer. Three low energy optimized isomers in Ge_6Ni series are shown in Fig. A.1. These structures can be obtained by adding a Ni atom to Ge_6(A) or by replacing a Ni atom from Ge_6(A) as reported[125]. By replacing one capped germanium atom by Ni from bi-capped hexagonal Ge_8 cluster gives the boat like optimized ground state as shown in 7D in Fig. A.1. The first size that can absorb the nickel atom partially is Ge_8Ni as shown in Fig. A.1. The ground state isomer is in $^1A_1$ electronic state, C_{2v} point group symmetry and in singlet spin state. The first structure that can enclose the nickel atom endohedrally is Ge_9Ni. Starting from n=9, all other isomers with n>9 absorb the nickel atom endohedrally and these structures are always having lower optimized energies compare to the same size exohedrally doped structures as calculated. Therefore, in the present report only endohedral-doped clusters are presented. The isomers marked as 9A, 9C and 9F in Fig. A.1 are very similar with almost same optimized energies. Several geometries are optimized in n=10 size to cover nearly all-possible endohedral-doped structures. Out of them the icosahedral structure (10A in Fig. A.1) in C_s point group symmetry is the supposed ground state. The endohedral Ni atom is almost at the center. 10 valence electrons of Ni are making bonds with all 10 germanium atoms in the cage. Because of the saturation of the dangling bonds this structure is very stable and will be discussed in later section. Little modification of the ground state $Ge_{10}Ni$ structure by adding a germanium atom gives the optimized ground state of $Ge_{11}Ni$. Calculated three very common low energy isomers in $Ge_{12}Ni$ are hexagonal pyramid like, fullerene like and icosahedral like structures as shown in Fig. A.2. Both the ground state structures we found with the size n=10 and 12 are icosahedral and usually very stable because of its symmetry, whereas the ground state structure for other values of 'n' are relatively less symmetrical. This could be the reason for the fluctuation of data in several parameters like charge, chemical potential etc. with the increasing size of the clusters as presented in the later section. The ground state we found in $Ge_{13}Ni$ is a germanium capped $Ge_{12}Ni$ hexagonal prism structure. The structure looks like a bowl with a nickel atom inside. The calculated ground state $Ge_{14}Ni$ has 3-fold symmetry and is a combination of

pentagons and rhombi. The other three structures are like hexagonal prism structures. By adding a germanium atom with one of the vertex of the $Ge_{14}Ni$ hexagonal pyramidal structure, the theoretical ground state of $Ge_{15}Ni$ can be obtained. Other isomers in this size are little modification over pentagonal $Ge_{10}Ni$ isomer with additional five germanium atoms at different positions. Nine different optimized isomers are presented in $Ge_{16}Ni$. The ground state in this size is a cage structure with C_2 symmetry. It is a combination of two widely separated squares and eight pentagons. Each square is connected to four pentagons separately. The isomer, 16B in Fig. A.3 can be constructed from a hexagonal $Ge_{12}Ni$ prism isomer where one side is capped by a Ge_3 triangular plane and the other side by a Ge atom. The total optimized energies of both of these isomers (16A and 16B) very similar. Other isomers are not very symmetrical and their optimized energies are also much higher than the first three isomers in this series. A number of optimized isomers are calculated for $Ge_{17}Ni$. Among these optimized structures, ten isomers are presented in Fig. A.3. The guess geometry of the ground state isomer in n=17 can be obtained by adding one germanium atom with the one arm of the square in the ground state isomer 16C. The next three cage isomers 17B, 17C, and 17D can be obtained by optimizing the guessed structures obtained by adding three Ge atoms to the ground-state isomer 14A at three different positions. The other structures in this size are modified 16F or 12Hexa geometries and are shown in Fig. A.3. The optimized isomers in $Ge_{18}Ni$ can be explained with the help of 17E or 12Hexa isomers. The isomers 18A, 18B, 18C and 18E can be constructed from 17E by adding one Ge atom on the opposite side of the floating Ge atom and then by connecting it to the other Ge atoms in the cage. Adding four germanium atoms at the side arms of hexagonal $Ge_{12}Ni$ structure yields the isomer 18D. Optimization after the addition of three Ge–Ge dimers to three alternate side planes of the hexagonal $Ge_{12}Ni$ geometry gives isomer 18G. Four different optimized isomers in $Ge_{19}Ni$ are shown in Fig. A.3. The ground-state isomer 19A is obtained by adding one Ge atom to the ground-state isomer 18A. The isomers 19B and 19D are tube like structures with hexagonal cross-section and with a Ge capping. The ground-state isomer 20A of $Ge_{20}Ni$ is a combination of 12 pentagons. Each side of a pentagon is connected to another pentagons, so that every pentagon is linked to five other pentagons. The other two structures, 20B and 20C can be obtained by adding two Ge atoms to the isomer 18E in different ways. 20D can be obtained by adding eight Ge atoms to the hexagonal $Ge_{12}Ni$ structure, or by capping the closed side of the isomer

19B with an additional Ge atom. Other structures are very much distorted and their optimized energies are also much higher than the ground state isomer.

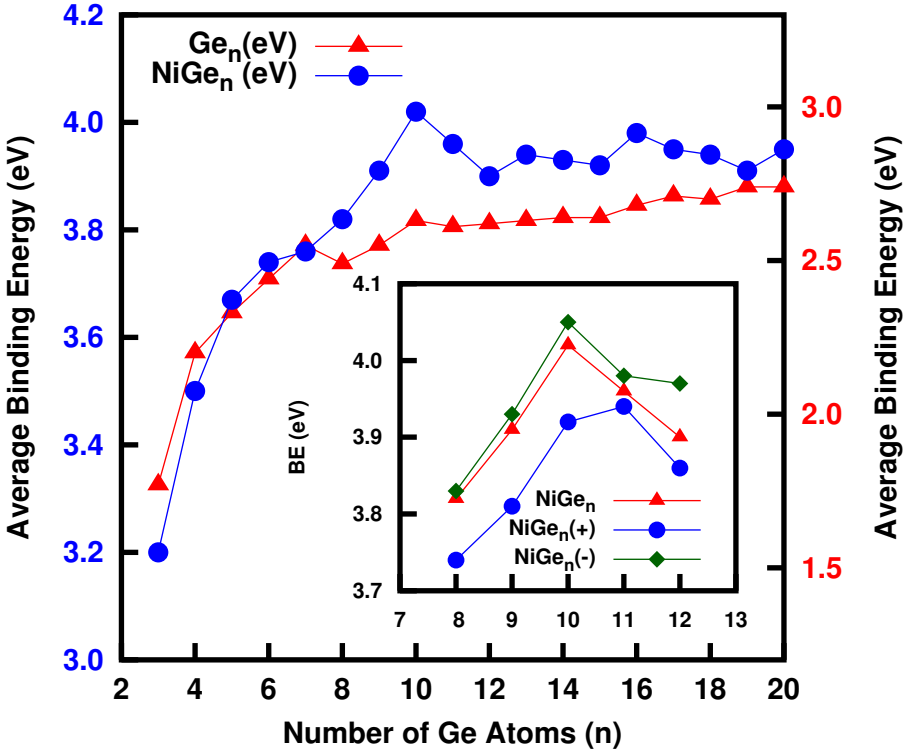

Figure 3.2: Variation of average binding energy of Ge_nNi clusters in neutral and different charged states with the cluster size

Upon examining the growth pattern of $NiGe_n$ clusters, it appears that cluster growth can be classified into three different categories. The first is Ni-capped structures where the Ni atom is added to a small sized pure-Ge cluster to form $NiGe_n$. In the second category a Ge atom in Ge_n cluster is replaced by a Ni to form $Ge_{n-1}Ni$ cluster. Both the categories are observed in the smaller cluster size range, where the cluster starts either from a Ge–Ge or from Ge–Ni dimer; then a nickel or germanium atom is added directly to Ge_n or a Ge added to $Ge_{n-1}Ni$ to form a $NiGe_n$ cluster. In the third category, the Ni atom is partially encapsulated in $NiGe_n$ cluster. Complete encapsulation of the Ni atom by the Ge cluster is found in n=9 and above. After that, it is only possible to add a Ge atom to a $Ge_{n-1}Ni$ cluster to form $NiGe_n$. During this growth process, the shape of the cluster changes from planar to a three-dimensional where the pure germanium cluster absorbs nickel atom exohedrally or endohedrally. It was found that larger clusters prefer to retain the Ni atom as the encapsulated atom in $NiGe_n$ cages.

3.3.2 Electronic structures and stabilities of $NiGe_n$ nanoclusters

The electronic structures and stabilities of Ge_nNi nanoclusters are discussed in this section on the basis of the variations of calculated physical and chemical parameters i.e. the binding energy (BE), the HOMO–LUMO gap (or ΔE), the embedding energy (EE), the stability or the second-order difference in energy, the ionization potential (IP), the electron affinity (EA), and the chemical potential (μ) with the cluster size. By monitoring the behavior of these parameters as the cluster size increases, we investigated whether or not electron counting can explain the relative stabilities of the clusters. To explore the relative stabilities of Ge_nNi clusters with increasing n, we first calculated various thermodynamic parameters of the clusters: the binding energy (BE), the embedding energy (EE), the HOMO–LUMO gap (ΔE), and the relative stability or the second-order energy difference.

The binding energy per atom of Ge_n or $NiGe_n$ clusters, following the work[42] is defined as:

$$BE = -\left[E_{Ge_nNi} - nE_{Ge} - E_{Ni}\right]/(n+1) \tag{3.1}$$

where, BE is the average binding energy per atom of the cluster, and E_{Ge}, E_{Ni} and E_{Ge_nNi} are the energies of germanium and nickel and the ground state energy of the Ge_nNi cluster respectively. For pure germanium clusters in the above equation E_{Ni} is taken as zero and n+1 is replaced by n. The binding energies of charged clusters are also calculated using the same equation. The binding energies of different neutral and charged clusters, along with the binding energy of pure Ge clusters, are shown in Fig. 3.2. Both the graphs show a rapid increase in the average binding energy per atom of the clusters in the small size range (for $n < 7$). This is because of the thermodynamic instability of smaller clusters. For clusters of size $n > 5$, the binding energy curve increases at a relatively slow rate with n, and finally saturate for the larger clusters ($n > 10$). For neutral clusters, the binding energy per atom in the saturation region (n=12–20) varies within 0.1 eV, with the maximum binding energy occurring at $n = 10$, whereas the maximum binding energy is observed for anionic and cationic states at n=10 and n=11, respectively. According to the 18- electron counting rule, the binding energy and other physical parameters (discussed in the next section) should show a local maxima or minima at n=7, 8 and 9 for anionic, neutral and cationic

clusters respectively. Whereas, according to the 20-electron counting rule, the binding energy and other physical parameters (discussed in the next section) should show a local maxima or minima at n=9, 10 and 11 for anionic, neutral and cationic clusters respectively. Thus, 20-electron rule is valid for neutral and cationic $NiGe_n$ clusters, but is not directly valid for anionic clusters. Therefore, to understand the detailed electronic charge distributions in the clusters, Mulliken natural bond orbital (NBO) analysis is performed, which allowed us to see how the valence electrons of Ge and Ni atoms are shared in bonds. In general, Ge is more electro- negative than Ni; the electro-negativities of Ni and Ge on the Pauling scale are 1.91 and 2.01 respectively. Mulliken population analysis also showed that, in this system, charge is always transferred from Ni to Ge, so Ni acts as an electron donor in Ge_nNi clusters. The detailed NBO analysis of the ground state icosahedral $Ge_{10}Ni$ structure in neutral, Ge_9Ni in anionic and $Ge_{11}Ni$ in cationic charged states are shown in Table 3.2.

As mentioned before, according to 20- or 18- electron counting rule, different physical and chemical parameters that can explain the thermodynamic and chemical stabilities of the clusters should show local or global peaks (maxima) or dips (minima) at n =10 or 8 for neutral $NiGe_n$. However, they do show regular behavior at n = 10 for neutral clusters, n=10 for anionic and n =11 for cationic clusters. According to the electron-counting rule, neutral $Ge_{10}Ni$, anionic Ge_9Ni and cationic $Ge_{11}Ni$ are supposed to be a 20-electron cluster. But the present calculated parameters of the clusters in different charged states show maxima or minima for n=10 (neutral and anionic) and 11(cationic), not for cationic Ge_9Ni. However, most of the parameters calculated for anionic clusters show neither local maxima nor a local minimum. Hence NBO analysis is done for neutral and anionic $Ge_{10}Ni$ and cationic $Ge_{11}Ni$ and for anionic Ge_9Ni clusters. With reference to the Table 3.2 in the ground state $Ge_{10}Ni$, $Ge_{10}Ni^-$, $Ge_{11}Ni^+$ and Ge_9Ni^- (as shown in Fig. A.4) clusters, the valence orbital distributions of Ge atoms are limited to s, p_x, p_y, and p_z, whereas those for Ni include s, p_x, p_y, p_z, d_{xy}, d_{xz}, d_{yz}, $d_{(x^2-y^2)}$ and d_{z^2}. The orbital distributions of HOMO, HOMO-1, LUMO and LUMO+1 of $Ge_{10}Ni$, $Ge_{11}Ni^+$ and Ge_9Ni^- are shown in Fig. A.2. From Table 3.2, it is clear that, among the 10 valence electrons of the Ni atom in all those four clusters, all 10 electrons are used to form different number of co-ordinate bonding with the Ge atoms in $Ge_{10}Ni$, $Ge_{11}Ni^+$ and $Ge_{10}Ni^-$ cages with total 10 electrons in number. Therefore, using the free electron theory, we find that approximately 20 electrons are present in the $Ge_{10}Ni$, $Ge_{10}Ni^-$ and $Ge_{11}Ni^+$ cages. Therefore, $Ge_{10}Ni$ cluster in neutral, $Ge_{10}Ni^-$

Table 3.2: Results of natural bond orbital (NBO) analysis of different ground state clusters

Neutral $Ge_{10}Ni$ cluster

Atom	Charge (e)[a]	Core	4s	$4p_x$	$4p_y$	$4p_z$	Rydberg	total
Ge	0.2595	28.00	1.557	0.906	0.774	0.774	0.016	32.027
Ge	0.2807	28.00	1.667	0.798	0.817	0.649	0.018	31.950
Ge	0.2605	28.00	1.558	0.907	0.772	0.772	0.016	32.026
Ge	0.2826	28.00	1.666	0.797	0.780	0.685	0.019	31.946
Ge	0.2832	28.00	1.665	0.797	0.646	0.820	0.018	31.947
Ge	0.2824	28.00	1.666	0.796	0.684	0.782	0.018	31.947
Ge	0.2793	28.00	1.669	0.797	0.780	0.686	0.019	31.951
Ge	0.2813	28.00	1.669	0.797	0.819	0.647	0.018	31.949
Ge	0.2788	28.00	1.670	0.798	0.650	0.816	0.019	31.953
Ge	0.2796	28.00	1.669	0.798	0.687	0.779	0.018	31.951
		Core	4s	$3d_{xy}$	$3d_{xz}$	$3d_{yz}$	Rydberg	
Ni	–2.768	17.99	0.432	1.934	1.934	1.934	0.389	28.351
			$3d_{x^2-y^2}$	$3d_{z^2}$				
			1.852	1.896				

Cationic $Ge_{11}Ni$ cluster

Atom	Charge (e)[a]	Core	4s	$4p_x$	$4p_y$	$4p_z$	Rydberg	total
Ge	0.357	28.00	1.708	0.717	0.782	0.567	0.021	31.789
Ge	0.347	28.00	1.666	0.875	0.713	0.567	0.017	31.838
Ge	0.318	28.00	1.610	0.863	0.747	0.727	0.016	31.964
Ge	0.383	28.00	1.703	0.641	0.639	0.794	0.020	31.797
Ge	0.199	28.00	1.581	0.976	0.711	0.805	0.016	32.088
Ge	0.368	28.00	1.633	0.753	0.738	0.686	0.019	31.830
Ge	0.200	28.00	1.581	0.976	0.710	0.805	0.016	32.088
Ge	0.369	28.00	1.634	0.753	0.740	0.685	0.019	31.830
Ge	0.384	28.00	1.703	0.641	0.638	0.795	0.019	31.798
Ge	0.194	28.00	1.507	1.034	0.776	0.775	0.015	32.107
Ge	0.341	28.00	1.804	0.748	0.534	0.426	0.013	31.524
		Core	4s	$3d_{xy}$	$3d_{xz}$	$3d_{yz}$	Rydberg	
Ni	–2.460	18.00	0.430	1.854	1.935	1.897	0.398	28.345
			$3d_{x^2-y^2}$	$3d_{z^2}$				
			1.929	1.904				

Anionic Ge_9Ni cluster

Atom	Charge (e)[a]	Core	4s	$4p_x$	$4p_y$	$4p_z$	Rydberg	total
Ge	0.100	28.00	1.576	0.818	0.860	0.810	0.011	32.189
Ge	0.140	28.00	1.659	0.845	0.795	0.801	0.108	32.110
Ge	0.140	28.00	1.658	0.796	0.795	0.849	0.108	32.110
Ge	0.114	28.00	1.610	0.786	0.909	0.789	0.012	32.107
Ge	0.140	28.00	1.659	0.732	0.840	0.868	0.108	32.110
Ge	0.115	28.00	1.610	0.863	0.765	0.856	0.124	32.107
Ge	0.101	28.00	1.689	0.766	0.953	0.768	0.011	32.188
Ge	0.140	28.00	1.658	0.855	0.840	0.744	0.011	32.109
Ge	0.207	28.00	1.679	0.685	0.921	0.629	0.009	31.925
		Core	4s	$3d_{xy}$	$3d_{xz}$	$3d_{yz}$	Rydberg	
Ni	-2.199	17.998	0.438	1.877	1.831	1.875	0.193	28.042
			$3d_{x^2-y^2}$	$3d_{z^2}$				
			1.906	1.922				

Anionic $Ge_{10}Ni$ cluster

Atom	Charge (e)[a]	Core	4s	$4p_x$	$4p_y$	$4p_z$	Rydberg	total
Ge	0.155	28.00	1.576	1.064	0.749	0.075	0.017	31.617
Ge	0.051	28.00	1.648	0.882	0.846	0.654	0.018	32.048
Ge	0.153	28.00	1.577	1.064	0.748	0.748	0.017	32.154
Ge	0.048	28.00	1.647	0.882	0.805	0.697	0.018	32.049
Ge	0.049	28.00	1.646	0.882	0.654	0.849	0.018	32.049
Ge	0.048	28.00	1.647	0.881	0.696	0.805	0.018	32.047
Ge	0.051	28.00	1.650	0.880	0.804	0.698	0.018	32.05
Ge	0.051	28.00	1.648	0.881	0.848	0.655	0.018	32.05
Ge	0.053	28.00	1.650	0.880	0.658	0.846	0.018	32.052
Ge	0.052	28.00	1.649	0.881	0.699	0.803	0.018	32.05
		Core	4s	$3d_{xy}$	$3d_{xz}$	$3d_{yz}$	Rydberg	
Ni	0.288	17.998	0.433	1.920	1.920	1.908	0.318	28.288
			$3d_{x^2-y^2}$	$3d_{z^2}$				
			1.889	1.901				

[a]Electronic charge e=-1.6021764610^{-19} Coulomb

and $Ge_{11}Ni^+$ can be considered as 20-electron clusters and show maximum binding energy. The same is true for other thermodynamic and chemical parameters of the system and will be discussed in the later section.

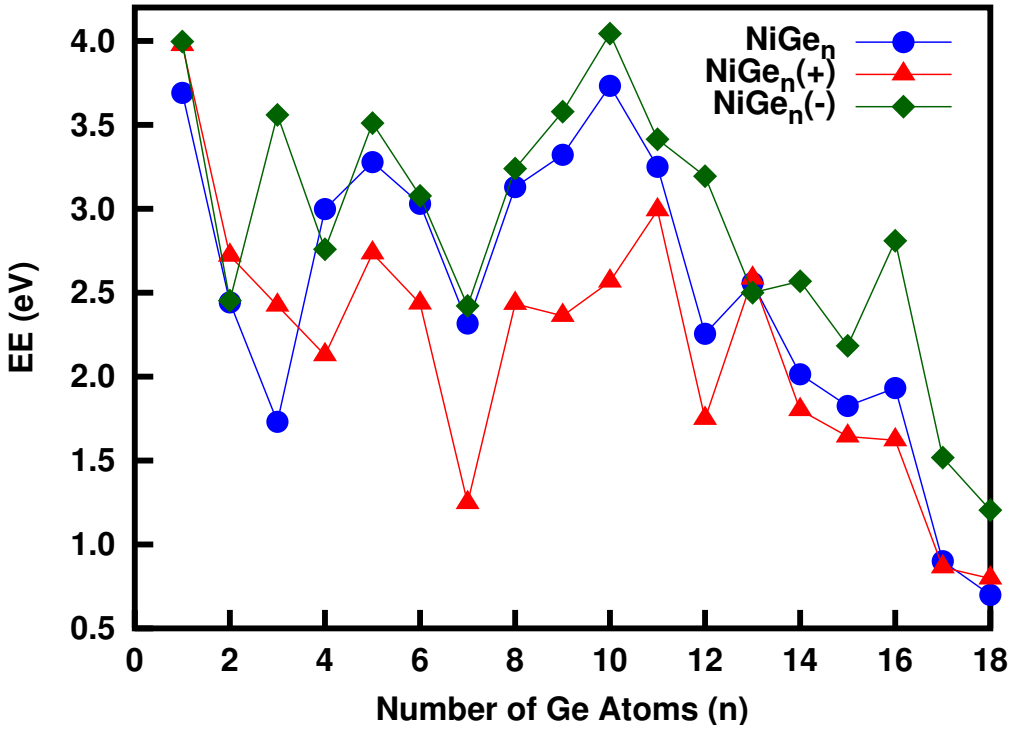

Figure 3.3: Variation of embedding energy of Ge_nNi clusters in neutral and different charged states with the cluster size

The embedding energies (EEs) of the clusters are also calculated to explain the

thermodynamic stabilities. The embedding energy can define in different ways. It can be positive or negative depending on the definition used. In the present study, the embedding energy of a cluster applying the WW spin-conservation rule [141], is defined as:

$$\left.\begin{aligned} EE = E(^{M}Ge_n) - \quad & E(^{0}Ni) - E(^{M}Ge_nNi) \\ or & \\ EE = E(^{0}Ge_n) - \quad & E(^{M}Ni) - E(^{M}Ge_nNi) \end{aligned}\right\} \tag{3.2}$$

where, M is the total spin of the cluster or the atom in units of h/2π is always positive. In this case, we have chosen the higher of the resulting two embedding energies. In the present calculation, all ground states up to n=3 are triplet and above that all are singlet.

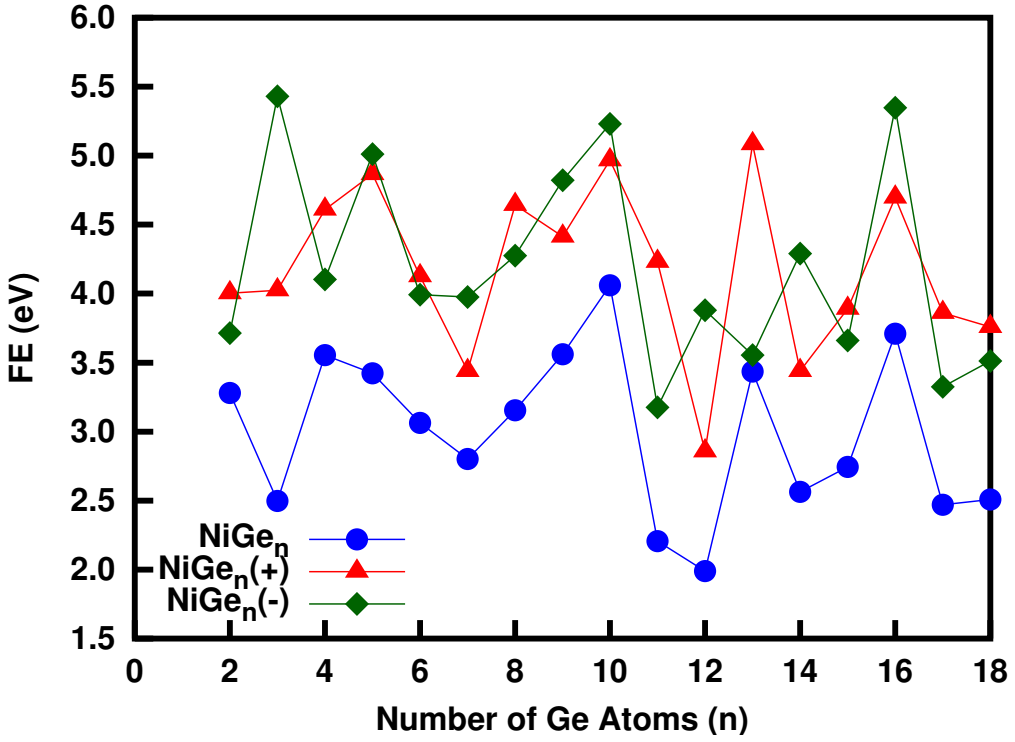

Figure 3.4: Variation of fragmentation energy of Ge_nNi clusters in neutral and different charged states with the cluster size

Therefore, to calculate the embedding energy according to the WW spin-conversation rule, the pure Ge clusters were taken to be in either the triplet or the singlet state. For charged ($\pm$1) clusters of multiplicity M, the embedding energy of such a cluster (say cationic) can be written as:

$$\left.\begin{aligned} EE^{WW} &= E(^2Ge_n^+) - \quad E(^1Ni) - E(^2Ge_nNi^+) \\ &or \\ EE^{WW} &= E(^1Ge_n) - \quad E(^2Ni^+) - E(^2Ge_nNi^+) \end{aligned}\right\} \tag{3.3}$$

Variation of embedding energy with the size of the clusters is shown in Fig. 3.3. Both neutral and anionic clusters show a maxima at n=10, where as the cationic clusters show maximum embedding energy at n=11. Therefore, the neutral and cationic clusters follow 20-electron rule directly. The sharp minima at n=12 for neutral and cationic cluster represent relatively less favorable embedding nature of these clusters. Following the NBO analysis results presented in Table 3.2, one can get much better idea of embedding energy variation for neutral and charged clusters.

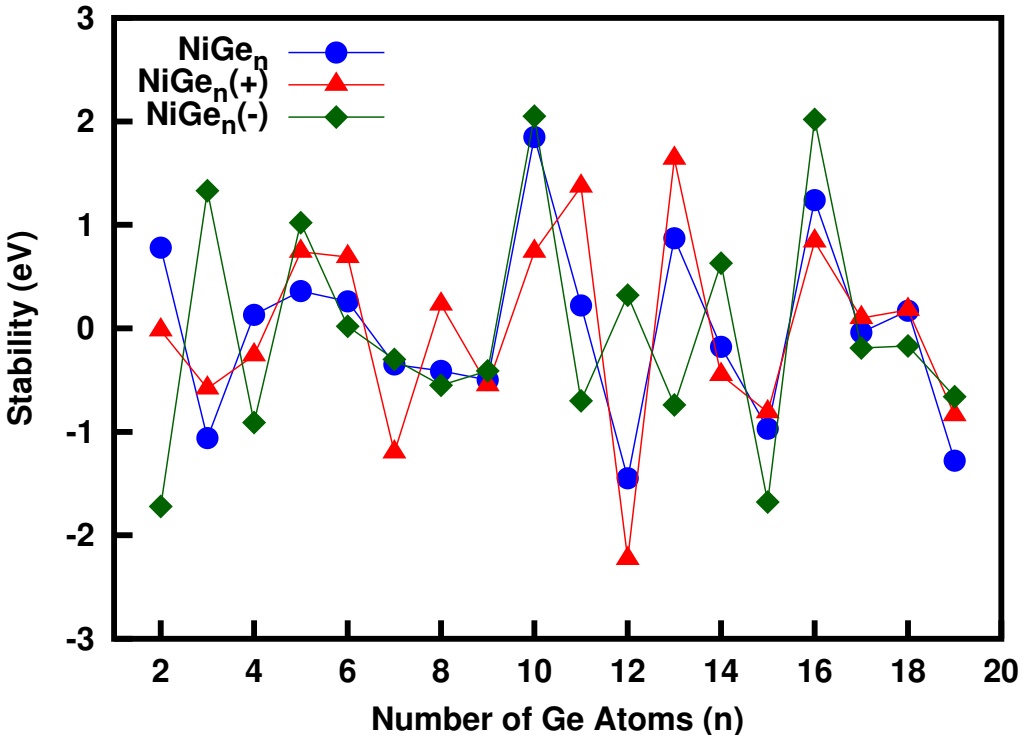

Figure 3.5: Variation of stability of Ge_nNi clusters in neutral and different charged states with the cluster size

The stability parameter or 2^{nd} order energy difference:

$$\left.\begin{aligned} \Delta_2(n) &= [E(Ge_{n+1}Ni) - E(Ge_nNi)] - [E(Ge_nNi) - E(Ge_{n-1}Ni)] \\ &= E(Ge_{n+1}Ni) + E(Ge_{n-1}Ni) - 2E(Ge_nNi) \end{aligned}\right\} \tag{3.4}$$

According to this definition, the more stability means more positive the value of Δ_2(n), as it corresponds to a gain in energy during the growth process from the size immediately below, and less of a gain in energy to the next cluster size up. The stabilities of neutral and charged clusters are shown in Fig. 3.5. The neutral cluster show magic nature for the series n=8, 10, 12 and 14. The anionic cluster show positive stability at n =10 and then show a huge drop in stability for n =11 and 12. So it does not follow any particular series in the stability nature. The cationic cluster at n=11 show local maxima and this is supported by 20-electron rule. The nature of the stability graph and the results presented in Table 3.2 support the relatively higher stability in 20-electron clusters: neutral $Ge_{10}Ni$, cationic $Ge_{11}Ni$ and anionic $Ge_{10}Ni$ clusters. In general, the clusters are known as "magic" clusters because of their positive and relatively higher stabilities.

Again, to investigate the growth behavior of Ge_nNi clusters the fragmentation energy (FF) or Δ(n,n-1) is calculated starting from the Ge–Ni dimer. The fragmentation energy is defined as follows:

$$\Delta(n, n-1) = E(Ge_{n-1}Ni) + E(Ge) - E(Ge_nNi) \tag{3.5}$$

It is clear from the Fig. 3.4, that there is a sharp drop in the fragmentation energy from n = 10 to 11 both in the neutral and anionic state of $Ge_{10}Ni$ cluster, whereas, the fragmentation energy drops sharply from n = 11 to 12 in cationic $Ge_{11}Ni$ cluster. The sharp drop in fragmentation energy for both neutral and charged clusters is an indication of maximum local stability of $Ge_{10}Ni$ cluster. Systematic behaviour of BE, EE, Δ_2(n), and Δ(n,n–1) at n=10 indicate that $Ge_{10}Ni$ has a relatively high thermodynamic stability. To understand the charge exchange between the cage and the embedded Ni atom during hybridization with the germanium clusters in neutral state, the variation of charge on the Ni atom and the average charge per Ge atom in the ground state $NiGe_n$ clusters as a function of the size of the cluster is calculated and presented in Fig. 3.6. Just like the other parameters discussed above, the charge on the Ni and Ge atoms show a local maximum and minimum respectively at n = 10. This result provides further support on the highest relative stability of $Ge_{10}Ni$ cluster in neutral state. It is clear that the charge transferred from the Ni to Ge in the icosahedral $Ge_{10}Ni$ cage and this enhances the electrostatic interaction between the cage and the Ni atom, which plays an important role in stabilizing $Ge_{10}Ni$ cage.

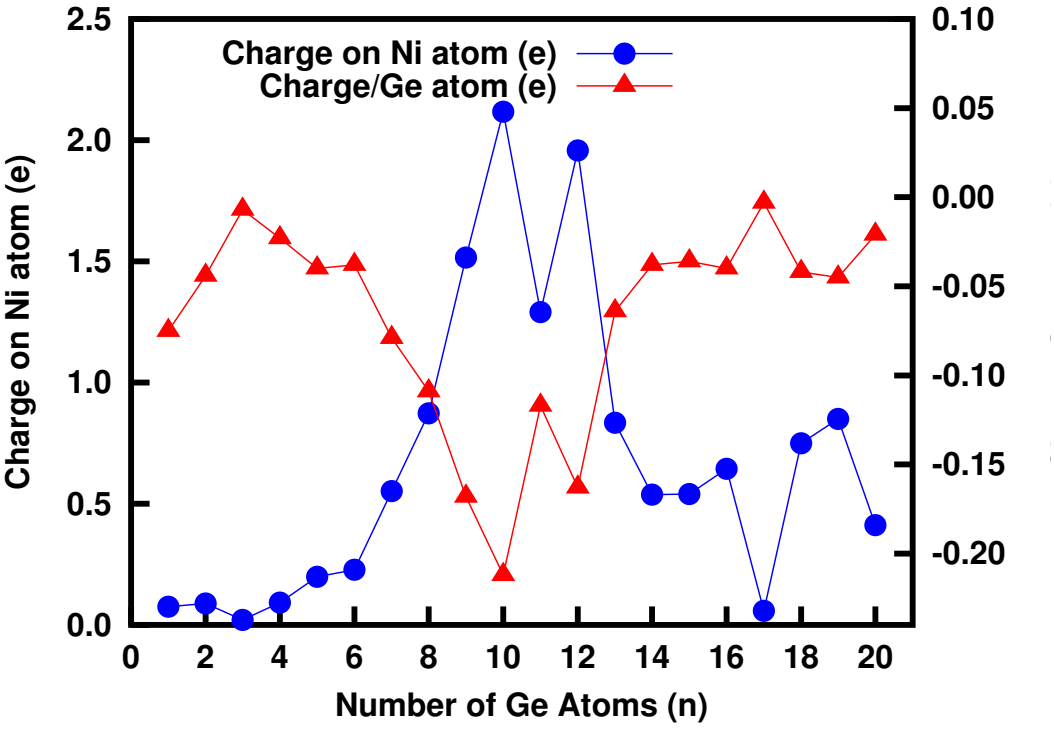

Figure 3.6: Variation of charge on Ni and average charge/Ge atoms in Ge_nNi clusters with the cluster size. Here positive and negative signs represent the charge donated and received respectively

To study the kinetic stabilities of the clusters in a particular environment, the HOMO–LUMO gap (E), ionization potential (IP), electron affinity (EA), chemical potential (μ), chemical hardness (η), and polarizability (α) of each cluster are calculated. In general, as the HOMO–LUMO gap (E) increase, the reactivity of the clusters decrease. The HOMO–LUMO gaps of neutral and charged clusters are plotted in Fig. 3.7. As also seen for other transition metal doped Si and Ge clusters[122,142], a decreasing trend is observed for the HOMO–LUMO gap with the increasing size o the clusters both in neutral and charged states, with some local oscillations. In Fig. 3.7, there are clear local maxima at n = 10, 10, and 11 for neutral, anionic, and cationic Ge_nNi clusters. This is again indicating that the $Ge_{10}Ni$ cluster is unusually stable as it is found from NBO analysis in Table 2. The main focus of the present study is to understand the relative stability of the clusters in terms simple electron counting rule. As reported in the previous study for the metal clusters that according to the electron shell model whenever a new shell starts getting occupied for the first time, the ionization potential (IP) drops sharply[120].

In a report, de Heer[2] has shown that in L_n series, L_{20} cluster is a shell field configuration and there is a sharp drop in ionization potential when the cluster grows

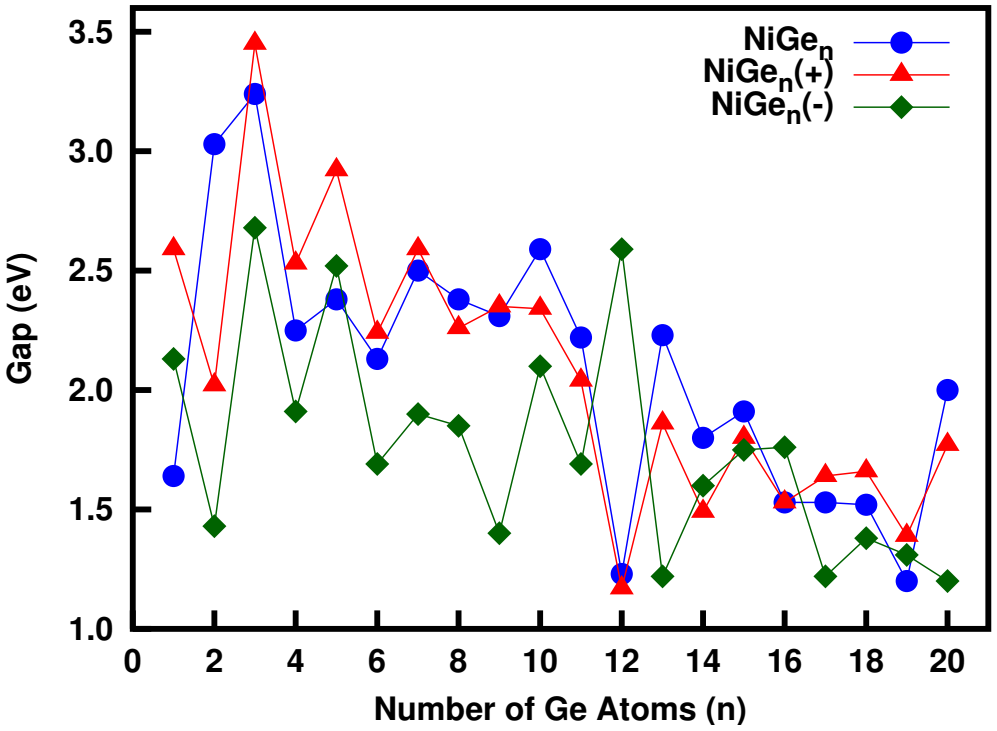

Figure 3.7: Variation of HOMO-LUMO gap of Ge_nNi clusters in neutral and different charged states with the cluster size

from L_{20} to L_{21}. If the enhanced stability in $Ge_{10}Ni$ cluster is due to a shell field configuration then there should be a sharp drop in ionization potential if one more germanium atom is added to it. This is clearly seen in Fig. 3.8. There is a local peak in ionization potential graph at n=10 and then there is a sharp drop in IP from n = 10 to 11. The drop in IP could be the strongest indication of the assumption of nearly free-electron gas inside the $Ge_{10}Ni$ cage cluster. The IP of a $Ge_{10}Ni$ cluster is in the same range as that of the transition metal atoms. Hence, it may be possible to form a number of stable halides using this cluster. Discovery of such stable clusters can be helpful to identify new semiconductor-TM metal based "superatoms" that can be future building blocks for cluster-assembled designer materials.

Other parameter that can help to understand the chemical stability of a system is electron affinity. It can be defined as:

$$EA(eV) = E(Ge_nNi) - E(Ge_nNi^-) \tag{3.6}$$

By the present definition electron affinity (EA) it is always positive and clusters with more electron affinity are more reactive and hence are less stable. Variation of electron affinity with the cluster size is shown in Fig. 3.8 along with the ionization

potential of the clusters. In the graph there is a local minima at n=10. There is a hike in electron affinity from n=10 to 11 and it continues up to n=12. Then again there is a sharp drop in electron affinity from n = 12 to 13. Relative dip in EA at n=10 is an indication of enhanced stability of $Ge_{10}Ni$ clusters in neutral state.

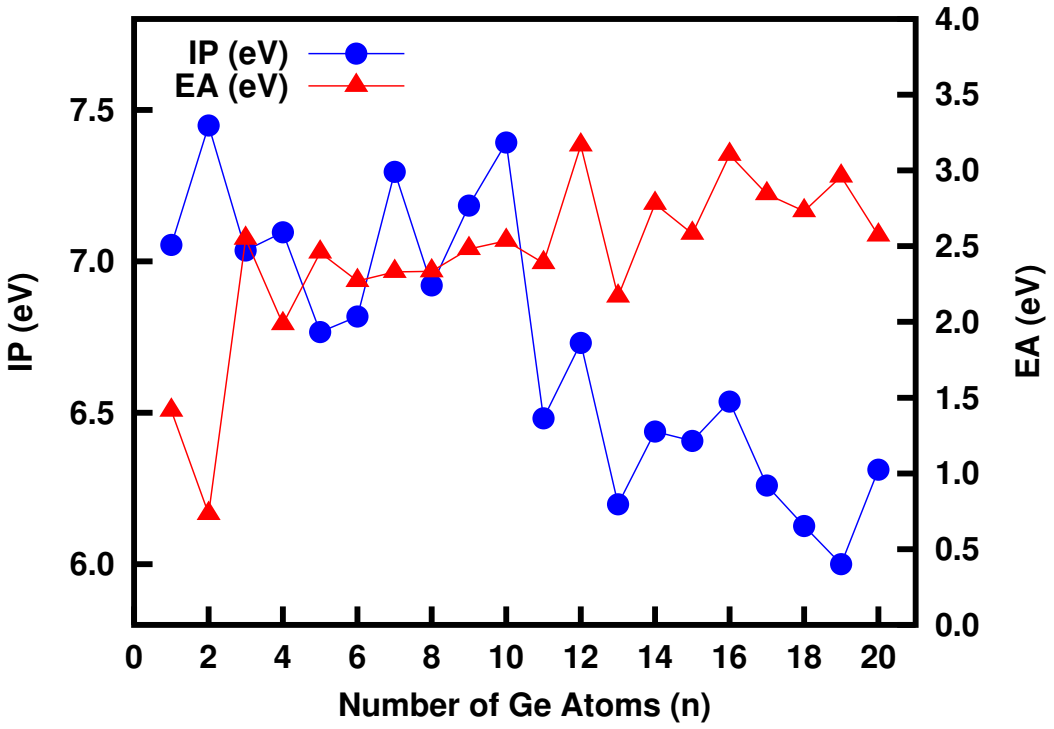

Figure 3.8: Variation of ionization potential and electron affinity of Ge_nNi clusters with the cluster size

Again, the maximum hardness principle (MHP) also can be used to characterize the relative stability of a system. To verify the chemical stability of the Ge_nNi clusters, chemical potential (μ) and chemical hardness (η) of the ground state clusters in each size are calculated. By description of chemical potential and chemical hardness, both the parameters can be expressed in terms of electron affinity and ionization potential. In terms of total energy consideration if $E(n_e)$ is the energy of a 'n_e' electron system, then energy of the system containing $n_e+\Delta n_e$ number of electrons, where $\Delta n_e << n_e$ can be expressed as:

$$E(n_e + \Delta n_e) = E(n_e) + \left.\frac{dE}{dn}\right|_{n=n_g} \Delta n_e + \frac{1}{2}\left.\frac{d^2E}{dn^2}\right|_{n=n_g} (\Delta n_e)^2 + ... \qquad (3.7)$$

Since contribution from the higher order terms is negligible, therefore, μ and η can be defined as:

$$\mu = \left.\frac{dE}{dn}\right|_{n=n_g} \tag{3.8}$$

and

$$\eta = \frac{1}{2}\left.\frac{d^2E}{dn^2}\right|_{n=n_g} = \left.\frac{d\mu}{dn}\right|_{n=n_g} \tag{3.9}$$

By definition,

$$IP = E(n_e - 1) - E(n_e) \tag{3.10}$$

By setting $\Delta n_e = 1$, μ and η are related to IP and EA via the following relations:

$$\mu = -\frac{IP + EA}{2} \tag{3.11}$$

and

$$\eta = -\frac{IP - EA}{2} \tag{3.12}$$

Consider two systems with μ_i and η_i (i=1,2) interacting each other, where some amount of electronic charge (Δq_e) transfer from one system to other. The quantity Δq_e and the resultant energy change (ΔE) due to the charge transfer can be determined in the following way:

If E (n_e+ Δq_e) is the energy of the system after charge transfer then it can be expressed for two different systems 1 and 2 in the following way:

$$E_1(n_e + \Delta q_e) = E_1(n_{1e}) + \mu_1(\Delta q_e) + \eta_1(\Delta q_e)^2 \tag{3.13}$$

and

$$E_2(n_e + \Delta q_e) = E_2(n_{2e}) + \mu_2(\Delta q_e) + \eta_2(\Delta q_e)^2 \tag{3.14}$$

Corresponding chemical potentials become,

$$\mu_1 = \left.\frac{dE_1(n + \Delta q_e)}{dn}\right|_{n=n_{1e}} = \mu_1 + 2\eta_1\Delta q_e \tag{3.15}$$

and

$$\mu_2 = \left.\frac{dE_2(n + \Delta q_e)}{dn}\right|_{n=n_{2e}} = \mu_1 + 2\eta_2\Delta q_e \tag{3.16}$$

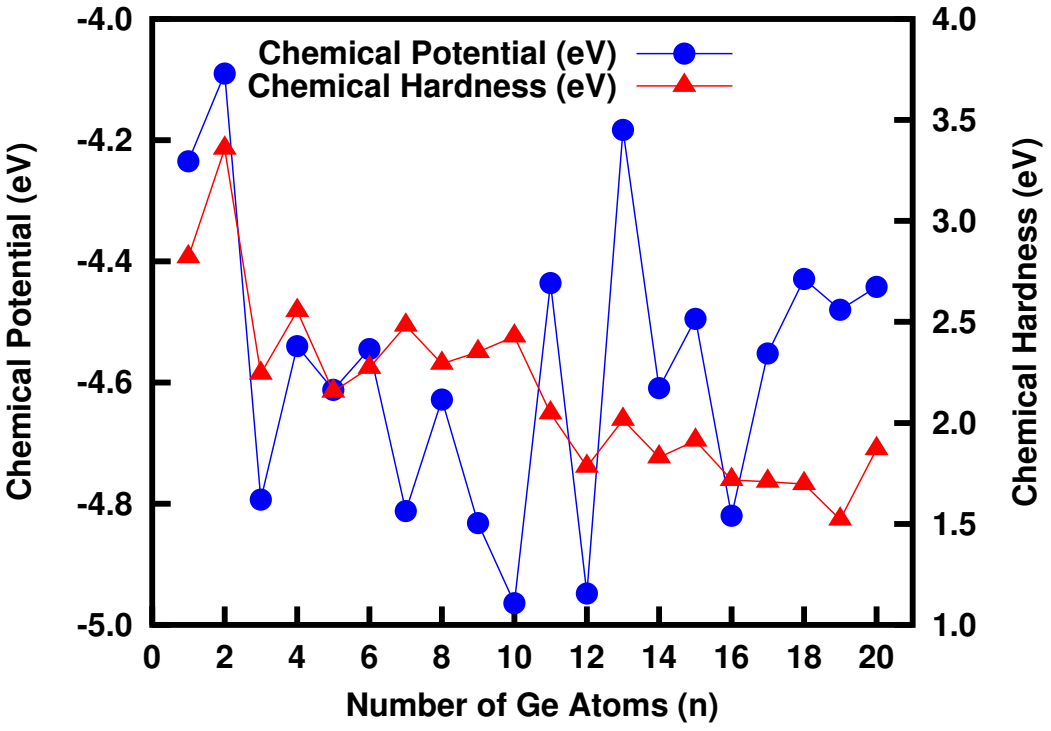

Figure 3.9: Variation of chemical potential and chemical hardness of Ge_nNi clusters with the cluster size

When the systems are in chemical equilibrium, *i.e.*, one can get the charge transfer and energy gain by the following expressions:

$$\Delta q_e = \frac{\mu_2 - \mu_1}{2(\eta_1 + \eta_2)} \tag{3.17}$$

and

$$\Delta E = \frac{(\mu_2 - \mu_1)^2}{2(\eta_1 + \eta_2)} \tag{3.18}$$

In the above expressions, ΔE is the gain in energy by the total system (1 and 2) due to exclusive alignment of chemical potential of the two systems at the same value. So for easier charge transfer from one system to other it is necessary to have a large difference in μ together with low η_1 and η_2. Therefore, Δq_e and ΔE can be taken as the factors to get the idea about the reaction affinity between two systems. Since they are function of the chemical potential and chemical hardness of the systems, so it is important to calculate these parameters to know the chemical stabilities in a particular environment.

Using the above theoretical background, chemical potential (μ) and chemical hardness (η) of $NiGe_n$ clusters are calculated and presented in Fig. 3.9. The local

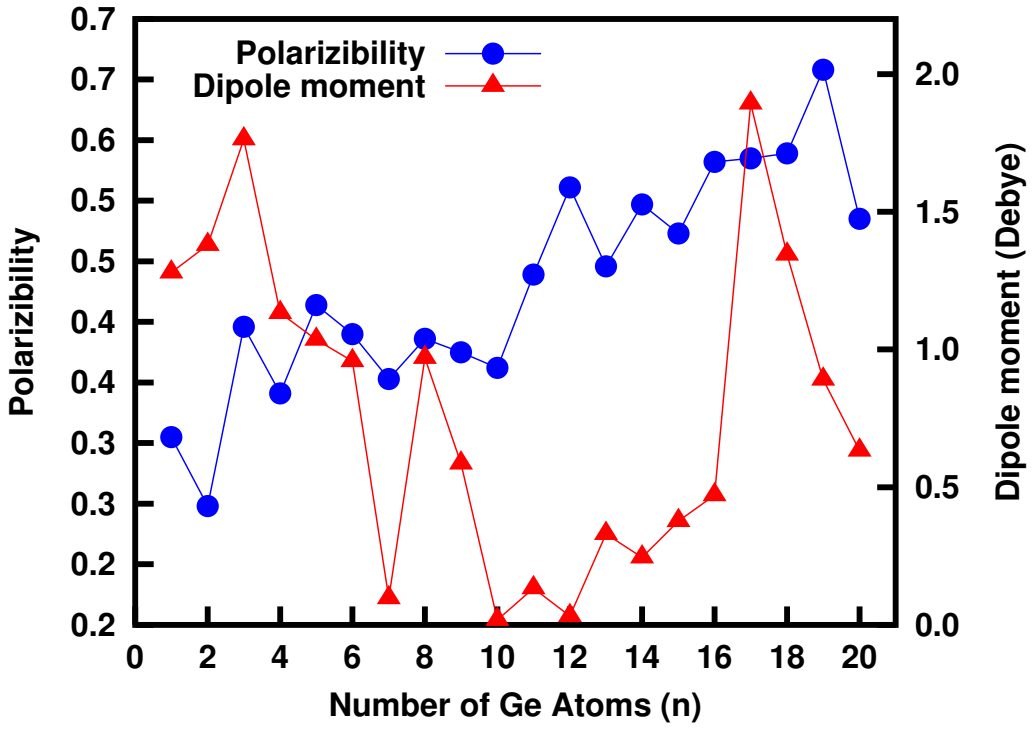

Figure 3.10: Variation of polarizability and electrostatic dipole moment of Ge_nNi clusters with the cluster size

minima of chemical potential at n=10 is an indication of higher stability compare to the surrounding sizes. Variation of chemical hardness, which is a measure of chemical affinity (considering covalent type of bonding) show local maxima at n=10. This local maximum is the measure of hardness of electronic clouds surroundings the cluster to oppose any kind of shearing in chemical bonding with the external agencies. Therefore, the peak at n=10 is indicating the higher stability. Again to understand the effect of chemical hardness on the polarizability, polarizability parameter is calculated and plotted in Fig. 3.10. Following the earlier theoretical works[143,144], in covalent type of bonding more hardness usually indicate lower polarizability. This is clear from the Fig. 3.9 and Fig. 3.10. To some extent electrostatic dipole moment of the cluster is also related to the atomic polarizability and the cluster structure. In a symmetrical cage like structure where Ni atom is at the center of the cage, the electrostatic dipole moment of the cluster is usually very low, as example, ground state 10A clusters. The dipole moments in the clusters suddenly increase when a germanium atom is dropped or added to the clusters. The ground state clusters within the size range between n=9 to 16 are all cage types with endohedrally doped Ni. The dipole moments of these clusters vary from 0 to 0.47 Debye. In the whole range of study first dipole moment of the clusters

decreases to zero or very low value within the range from n=10 to 15 and then again tend to increase when the distortion in the cage starts.

3.4 Conclusions

The present theoretical study reports the growth behaviour, stability, electronic and different chemical and physical properties of Ge_nNi clusters within the size range of n=1 to 20 under spin polarized generalized gradient approximation (GGA) using B3LYP method. Different physical and chemical properties of the optimized clusters are discussed. Based on the results, following conclusions have been drawn:

- The growth pattern of Ge_nNi clusters can be grouped mainly into two categories. In the smaller size range i.e. before encapsulation of Ni atom, Ni or Ge atoms are directly added with the Ge_n or $Ge_{n-1}Ni$ to form Ge_nNi clusters where binding energy of the clusters increase in a much faster rate than the bigger sized clusters. After encapsulation of Ni atom by the Gen cluster for n>7, the size of the Ge_nNi tend to increase by absorbing Ge atoms one by one on its surface keeping Ni atom inside the cage.

- It is found that the addition of Ni–atom to Ge clusters is always favorable at all sizes, as the embedding energy turns out to be positive (following the present definition) in every case of neutral and charged clusters. All clusters with size n > 7 absorb Ni endohedrally in the cage of Ge_n pure cluster.

- From the calculated results of BE, EE, Δ(n,n-1) and Δ_2(n) it is found that the cluster with n=10, 10 and 11 in neutral, anionic and cationic states are most stable. Detailed NBO analysis as discussed show that the neutral and charged clusters those are having nearly 20 valence electrons in total show enhanced stability, in agreement with shell model predictions. It also shows up in the IP values of the Ge_nNi clusters, as there is a sharp drop in IP from n = 10 to 11. Although the signature of stability is not so sharp in the HOMO-LUMO gap of the charged clusters, but there is a local maximum at n = 10 in neutral state. This is an indication of enhanced stability in the 20-electron cluster. Other parameters like, EA, chemical potential are related to the chemical stabilities and hardness along with polarizability and dipole moment of the neutral cluster for n = 10 also supports the identical stability nature of the clusters.

- As mentioned before, the drop in adiabatic ionization potential (IP) during the growth process is one of the strongest evidence of the existence of nearly free-electron gas inside the $Ge_{10}Ni$ cage cluster in the present calculation. In this contest it is important to mention that the B3LYP functional is not very much effective for extended quasi-metallic systems[145]. But in the present calculation it is found effective which could be due to the nano-order clusters of the system. Since the IP of a $Ge_{10}Ni$ cluster is in the same range as that of the transition metal atoms, therefore, it may be possible to form a number of stable halides using this cluster and it is possible to invent new semiconductor-TM metal-based "superatoms" that can be future building blocks for cluster-assembled designer materials and could open up a new field in electronic industry. The present work is the preliminary step in this direction.

Chapter 4

Cr doped Germanium nanoclusters

4.1 Introduction

In this chapter[†], the electronic structure, stability and magnetic quenching of $CrGe_n$ nanoclusters has been carried out using density functional theory (DFT). From the nature of the variation of the different thermodynamic and chemical parameters, the $CrGe_{10}$ and $CrGe_{14}$ ground state clusters are identified as the most stable species. It is observed that the enhanced stability of $CrGe_{10}$ and $CrGe_{14}$ are due to the closed shell filled structure of the Cr-atomic orbitals and follow the 18-electron counting rule. It is found that the strong mixing of the Cr d-orbital with the s- and p-atomic orbitals of the Ge atoms in the cluster are mainly responsible for the stability and quenching of the Cr magnetic moment in the clusters. Calculated CP's also give additional information about the bonding and its effect on the stability of the clusters. Calculated IR and Raman spectra also support these results.

4.2 Computational Details

Complete calculations are split into two parts mainly. All geometry optimizations were performed with no symmetry constraints. During optimization, it is always possible that a cluster with a particular guess geometry is trapped in a local minimum of the potential energy surface. To avoid this, we used a global structure predictor method using USPEX (Universal Structure Predictor: Evolutionary Xtalloraphy)[146] and VASP

[†]Kapil Dhaka, Debashis Bandyopadhyay, "Study of electronic structure, stability and magnetic quenching of $CrGe_n$ (n=1-17) clusters: A density functional investigation", *RSC Adv., (2015)*, 5, 83004-83012.

(Vienna AB-initio simulation package)[147] to get all the possible optimized geometric isomers in each size, from n = 8 to 17. VASP code has been used to relax the structures predicted by USPEX. For this, we have used a combination of the few-set of pseudo-potentials available in VASP. In the next stage of optimizations and post optimization calculations, the last few low energy isomers obtained from USPEX and VASP were reoptimized at different spin states in Gaussian'09[148] to obtain different energy parameters. Here, all calculations were performed within the framework of a linear combination of the atomic orbital's density functional theory (DFT). The generalized gradient approximation (GGA) calculations were carried out under the exchange-correlation potential as proposed by Perdew, Burke and Ernzerhof, commonly known as the PBE method[104,149] available in Gaussian'09. Different basis sets were used for germanium and chromium. The full electron 6-311G standard basis set available in Gaussian'09 for Cr and LanL2DZdp with effective core potential (ECP) obtained from the EMSL basis set exchange[150] for germanium are used to express the molecular-orbitals of all atoms as linear combinations of atom-centered basis functions. LanL2DZdp is a double-basis set with a LANL effective core potential (ECP) and with polarization function.[118,151] Unless specified otherwise, the results presented are obtained using the Gaussian'09 program package. The Demon2k program package[152] is used to calculate the critical points (CPs) inside the ground state clusters.

4.3 Results and discussion

Variations of the different thermodynamic and chemical parameters during the growth process provide the initial evidence to identify the stable nanoclusters. We have studied the growth of the doped clusters within the size range n= 1 to 17.

4.3.1 Ground state structures and relative stabilities

The optimized ground state structures and the corresponding spin magnetic moments along with the calculated bond critical points (BCPs) of $CrGe_n$ clusters are shown in Fig. 4.1 (also see Fig. B.1 and B.2 for other low energy isomers). To study the thermodynamic stability, we have calculated the variation of the average binding energy (BE), embedding energy (EE), fragmentation energy (Δ), stability or the 2^{nd} order change in energy (Δ_2) and ionization potential of the clusters, detachment energies etc. We define the BE, EE, FE, stability, VIP and ADE as follows:

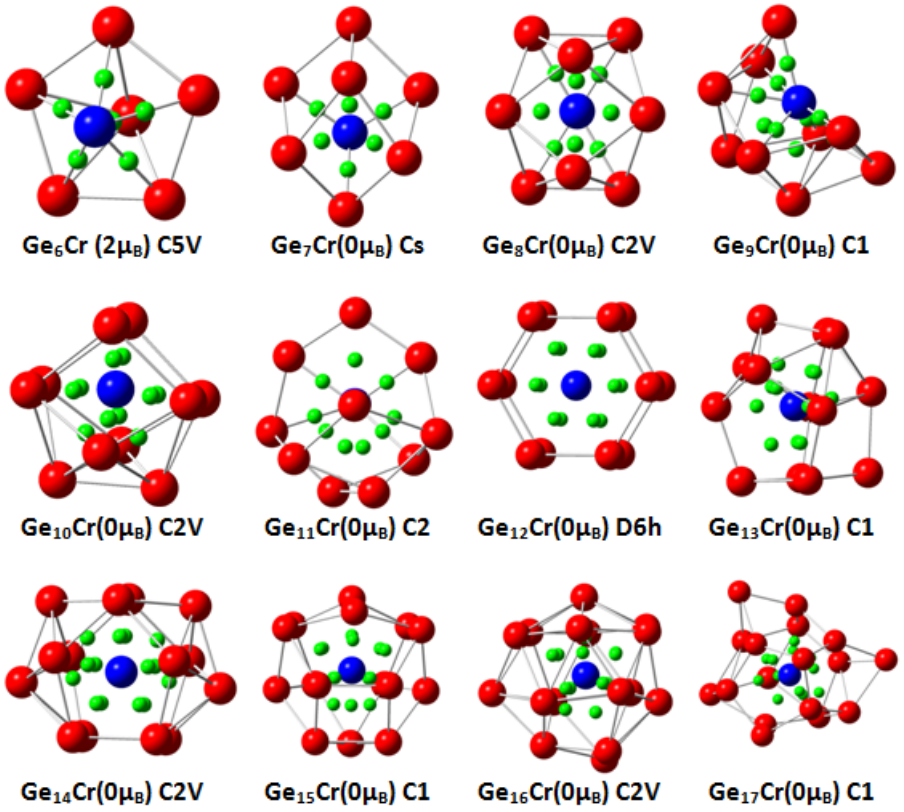

Figure 4.1: Ground state geometries and (3, -1) BCPs of $CrGe_n$ (n = 6–17). Red, blue and green spheres are denoting the Ge and Cr atoms, and the positions of the BCPs belonging to the Cr atom, respectively.

$$\left.\begin{aligned} BE &= -\left[E_{Ge_nCr} - nE_{Ge} - E_{Cr}\right]/(n+1) \\ EE &= E(Ge_n) - E(Cr) - E(Ge_nCr) \\ \Delta(n, n-1) &= E(Ge_{n-1}Cr) + E(Ge) - E(Ge_nCr) \\ \Delta_2(n) &= E(Ge_{n+1}Cr) + E(Ge_{n-1}Cr) - 2E(Ge_nCr) \end{aligned}\right\} \tag{4.1}$$

where, M is the total spin of the cluster or the atom in units of $\hbar$. Since the all ground state $CrGe_n$ clusters in the range n = 1–6 and n = 16 are magnetic, in the present study the binding energy and embedding energy of these clusters are calculated after imposing the Wigner–Witmer spin-conservation rule[141]. Imposing this rule the modified expressions of BE and EE are defined as follows:

$$BE = -\left[E(^{M}Ge_nCr) - nE(^{0}Ge) - E(^{M}Cr)\right]/(n+1) \tag{4.2}$$

$$\left.\begin{aligned} EE^{WW} &= E(^{M}Ge_n) - E(^{0}Cr) - E(^{M}Ge_nCr) \\ or & \\ EE^{WW} &= E(^{0}Ge_n) - E(^{M}Cr) - E(^{2}Ge_nCr) \end{aligned}\right\} \tag{4.3}$$

In the above binding energy and embedding energy expressions, we have chosen the higher of the resulting two BE and EEs. In the region for n < 7, the binding energy of the neutral and cationic clusters increases rapidly. This is an indication of the thermodynamic instability of the clusters. For the clusters with size n > 7, the binding energy increases with a relatively slower rate and then reaches nearly a saturation value with small variations. Between n = 1 to 6 the ground state clusters are in different spin magnetic states. The clusters show a magic nature (stable nature) with localized peaks at n = 10 and 14 (Fig. 4.2). Compared to the binding energy, the magic nature of the clusters are clearer in EE variation. Above n = 6 size, a number of local maxima arise at n = 8, 10 and 14, indicating that these clusters are more stable compared to their nearby clusters (Fig. 4.2). Variation of the fragmentation energy (FE) is another important evidence to check the stability of the clusters. Following the expression, FE indicates the gain in energy by a cluster during its growth process by absorbing germanium atoms one by one, starting from a Ge–Cr dimer.

With reference to the FE variation (Fig. 4.2), at n = 8, 10 and 14 clusters are more stable compared to their neighboring sizes. The variation of the 2^{nd} order change in energy or stability (Δ_2) (Fig. 4.2) shows a magic behavior at n = 10 and 14. On the basis of the thermodynamic parameters we found that the n = 8, 10 and 14 clusters are relatively more stable compared to the other sizes. In the present discussion we are mainly concerned about the endohedrally-doped clusters. Though the ground state isomer at n = 8 is thermodynamically stable, the Cr atom absorbed into the surface of the Ge_8 cage to form a hybrid $CrGe_8$ cluster. Since the Cr atom is exposed, the chemical affinity is higher compared to the endohedrally-doped clusters. Therefore, we are not interested in the thermodynamic stability of this cluster.

In order to understand how the removal or addition of one electron is changing the chemical stability of the clusters, we have calculated ionization potentials (AIP and VIP), the HOMO-LUMO gap, and the detachment energies (VDE and ADE) (Fig. 4.2). Variation of the AIP and VIP nature are similar, with a small difference between these values in a particular size. There are sharp peaks at n = 10 and 14 in the variation of the ionization potential with a maximum value at n = 14 indicating that $CrGe_{14}$

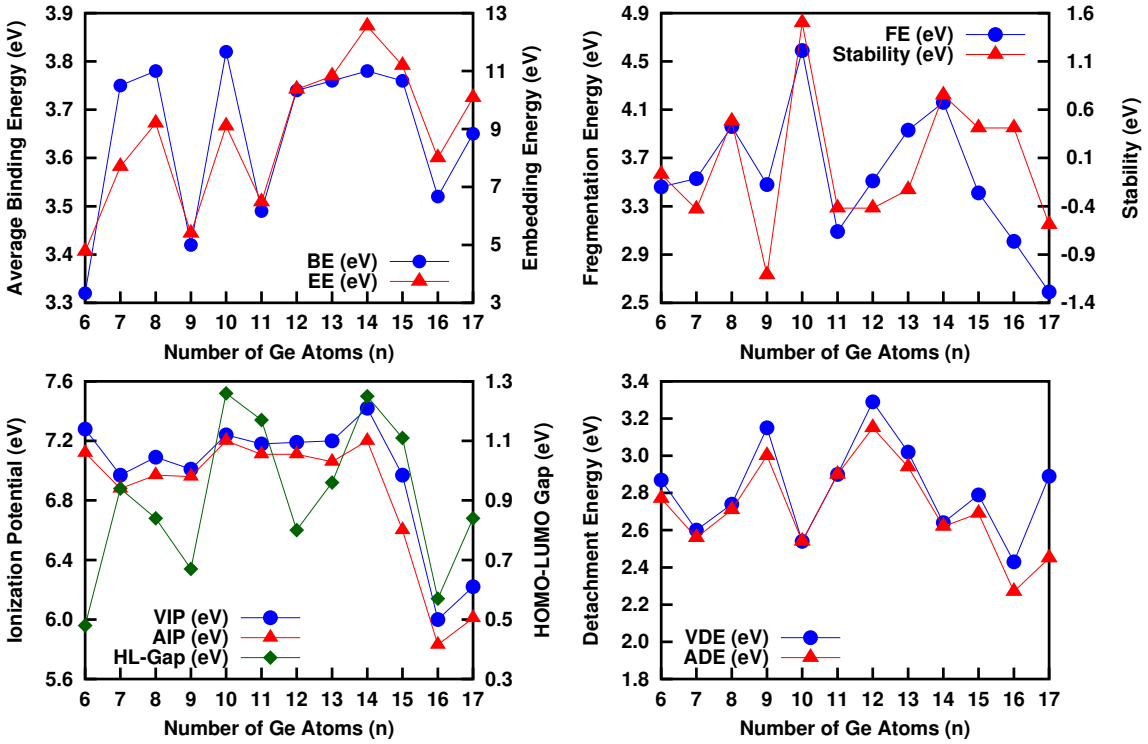

Figure 4.2: Variation of the average binding energy, embedding energy, fragmentation energy, stability, VIP, AIP, HL-Gap, VDE and ADE of the clusters during the growth process.

is the most stable cluster among all. Variation of the HOMO–LUMO gap with the growth of the cluster is one of the important pieces of evidence to understand the closed shell nature of the clusters. With reference to Fig. 4.2, both $CrGe_{10}$ and $CrGe_{14}$ have an almost equal HOMO–LUMO gap of close to 1.29 eV. There is a clear dip in the HOMO–LUMO gap variation at n = 12 and 16 with values of 0.78 eV and 0.57 eV respectively among the endohedrally doped clusters. The cause of the enhanced stability of the n = 10 and 14 clusters will be discussed in the next section on the basis of molecular orbital analysis. We have calculated the vertical detachment energy (VDE) and adiabatic detachment energy (ADE) following the equations mentioned in the previous section. Here, VDEs are the energy differences between the anionic and neutral cluster at a particular size, keeping the geometry of the cluster unchanged. Whereas ADE defines the energy difference between the anionic ground state and neutral ground state in a particular size of a cluster. In the later case, the geometry of these two clusters may be different. The variation of VDE and ADE with the cluster size shown in Fig. 4.2 supports the results obtained from the AIP, VIP and HOMO–LUMO gap variations of the clusters. The clear local minima at n = 10 and 14 indicate that it is easy to remove

electrons from the anionic state in these clusters and hence gives an indication of the enhanced stability of these clusters.

4.3.2 Molecular orbital analysis

With reference to our calculation of thermodynamic and chemical parameters, we found that $CrGe_{10}$ and $CrGe_{14}$ clusters are relatively stable compared to the other clusters in the series. From our previous discussion, it is clear that the n = 10 and 14 clusters can be taken as the stable clusters. We need to make it clear why these clusters are stable but not n = 12. Here we apply molecular and atomic orbital analysis to explain it.

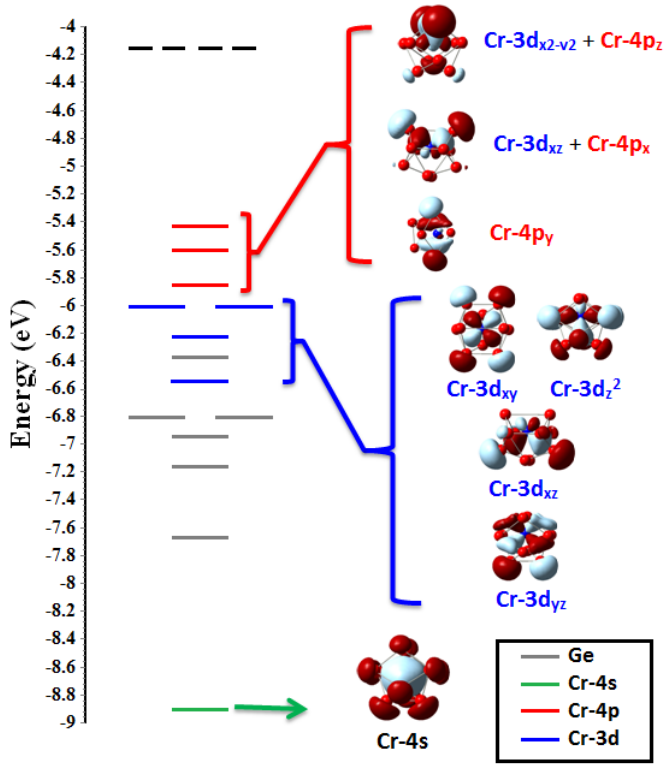

Figure 4.3: Molecular orbitals (MO's) of $CrGe_{10}$ (with the Cr contribution).

First we will discuss the cause of the lower stability of the $CrGe_{12}$ ground state cluster. The $CrGe_{12}$ ground state cluster is a well-known hexagonal prism with D6h symmetry with an endohedrally doped Cr atom between the two hexagonal rings of Ge atoms with 54 valance electrons (6 from Cr: $3d^5$ $4s^1$ and 4 from each Ge: $3s^2$ $3p^2$) in singlet spin states. With reference to Fig. 4.3, the orbital energy levels are assigned based on orbital composition. There are in total 27 filled energy levels with paired electrons, indicating quenching of the Cr spin moment. The electronic distributions can

be written in the following sequence: $1S^2$, $1P^6$, $1D^8$, $1F^8$, $2S^2$, $1D^2$, 1 G^2, $1F^4$, $1G^2$, $2P^4$, $2D^8$, $2P^2$, $2D^4$ (HOMO) and $2D^2$ (LUMO). Here we assign the orbitals following a method adopted by Abreu et al.[22] and we also found that the jellium model[153] is incompatible to explain the electronic structure of this cluster because of the presence of the 12 electrons in the 2D orbital. One of the 2D orbitals ($2D_{z^2}$) appears in the LUMO. This could be due to the crystal-field like splitting[154] in the molecular orbital in the cluster. To understand whether the 18-electron rule can be applied or not, we have analyzed one-electron orbitals of Cr in the $CrGe_{12}$ cluster.

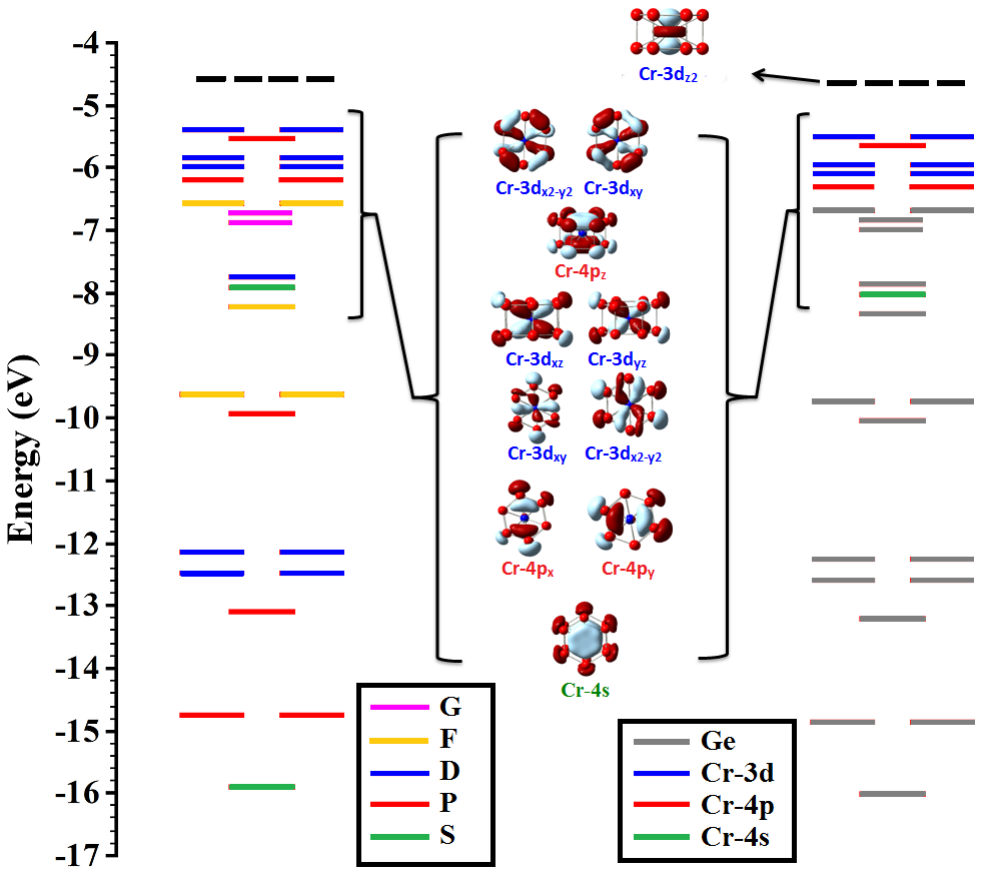

Figure 4.4: Molecular orbitals (MO's) of $CrGe_{12}$ (with the Cr contribution).

With reference to the recent report by Goicoechea and McGrady[34], since Cr is in the 6^{th} column in the periodic table, one of its 3d level will be pushed up to the higher side of the energy level in $CrGe_{12}$. To find out the contribution from Cr in the MOs we have used a fragment analysis where clusters are divided into Cr and Ge_{12} fragments[155]. Using this analysis we found a reasonable amount of contribution from the Cr-$3d_{z^2}$ atomic orbital in the LUMO which is being pushed up from the lower level. This also could be the reason for the good amount of HOMO–LUMO gap of 0.82 eV

in this cluster. The result of the one-electron orbitals is shown in Fig. 4.3. Since the LUMO contains the $3d_{z^2}$ orbital contribution of Cr, which is unfilled, therefore the total number of electrons that occupied these orbitals is 16 (Fig. 4.3).

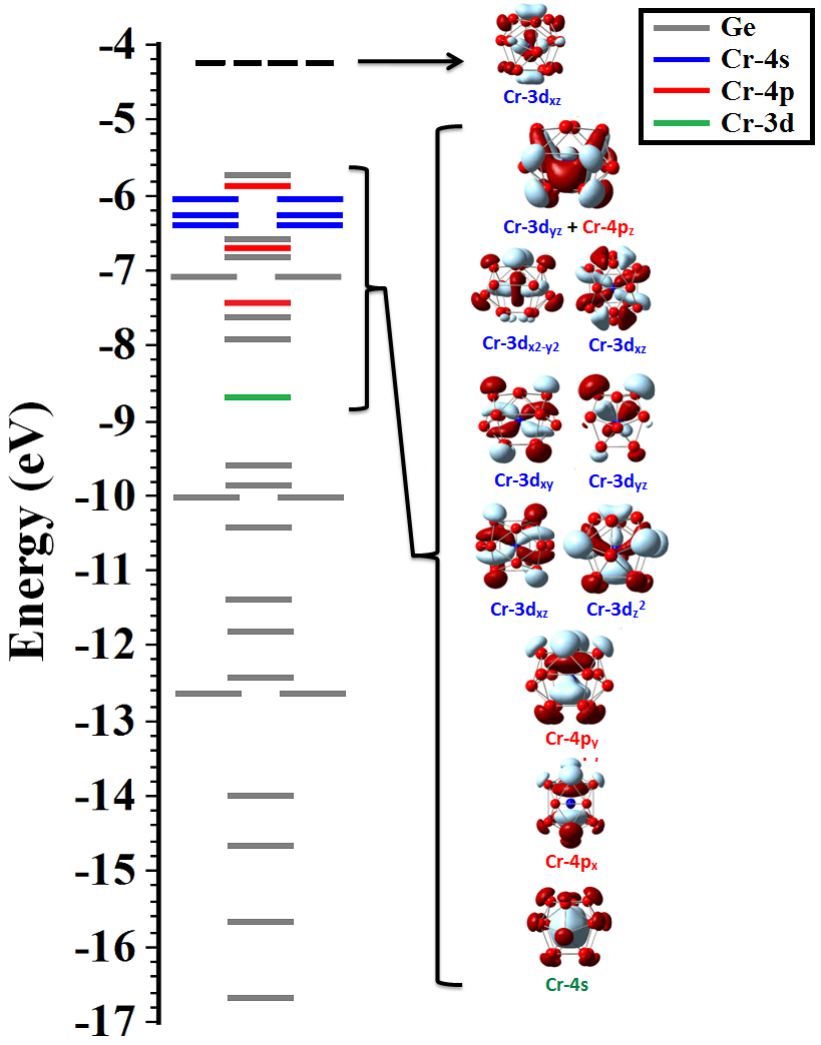

Figure 4.5: Molecular orbitals (MO's) of $CrGe_{14}$ (with the Cr contribution).

Since one 3d orbital (LUMO: $3d_{z^2}$) is unfilled, the 18-electron rule cannot be applied here. This could be the possible reason why $CrGe_{12}$ does not show a stable nature in the thermodynamic and other parameter variation (Fig. 4.2). In this context, we can recall our discussion in an earlier section of this work where we discussed the results of Hiura et al.[156], the WSi_{12} cluster can be taken also as a 16-electron cluster. Compared to $CrGe_{12}$, both $CrGe_{10}$ and $CrGe_{14}$ have higher values of BEs, EEs, FEs, Δ_2s, IPs and HOMO–LUMO gaps. Applying the same method to $CrGe_{10}$ and $CrGe_{14}$ clusters, we found that both of them follow the 18- electron rule. In the case of $CrGe_{10}$, the assigned molecular orbitals may not follow a particular structure, but a signature of

contribution from Cr in these orbitals is clearly seen. The signature supports the Cr contribution results in our calculations. On the basis of that, we have assigned that the Cr-atomic orbitals are filled with a configuration of $4S^2$, $4P^6$ and $3D^{10}$ (Fig. 4.4). Hence all atomic orbitals of Cr are engaged. In this case the Cr metal atom and the cage shared the electron density in such a way that both of them fulfill 18-electron counting. The same is true in the electronic structure of $CrGe_{14}$. In fact, Cr contributions are clearer in the $CrGe_{14}$ cluster due to the hybridization between the Cr-d orbital and the caged Ge-4p orbital, producing two Cr-$3d_{xz}$, one Cr-$3d_{yz}$ and one Cr-($3d_{yz}$+$4p_z$) mixed orbitals (Fig. 4.5). In $CrGe_{14}$ the LUMO is assigned as $3d_{xy}$. Therefore, $CrGe_{10}$ and $CrGe_{14}$ follow the 18-electron counting rule, but it cannot be applied in $CrGe_{12}$ as per our results.

4.3.3 Bond and frequency analysis

To investigate the strength of the Ge–Ge and Ge–Cr interaction with the increasing size of the clusters, and also to understand the bonding nature, we have calculated the number of different bonds present in the clusters. We have calculated the bond critical points (BCPs) and cage critical points (CCPs) (see Fig. B.3 and B.4 for RCPs and CCPs) and their locations in the cage to interpret the nature of bonding present in the cage based on the work reported by Bader[157].

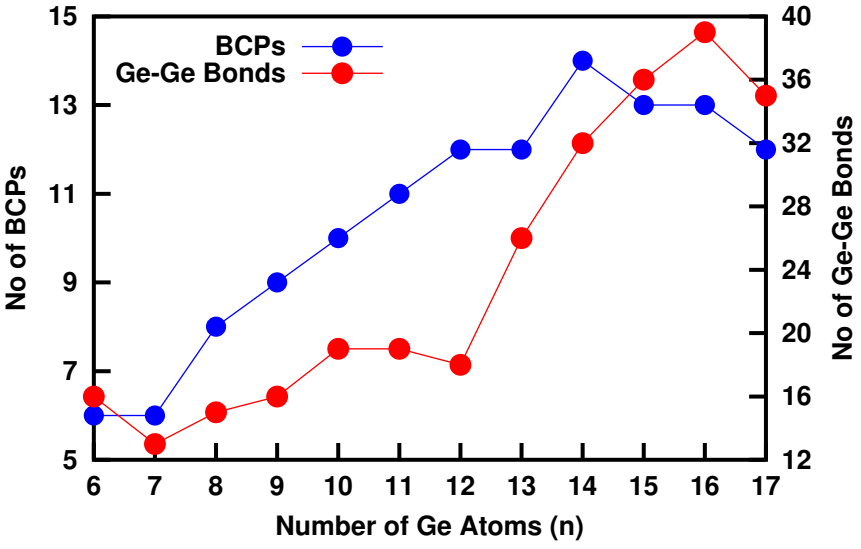

Figure 4.6: Bond critical points (BCPs) and no. of Ge–Ge bonds

The chemical interaction between the fragments of a given set of molecules can be characterized by the Laplacian of electronic densities. When the density is positive it describes closed shell bonding, and when it is negative, it is covalent bonding. The critical point is one where this electron density vanishes in 3-D. Therefore this is a position on the bond and is reflecting the existence of the presence of a bond. A

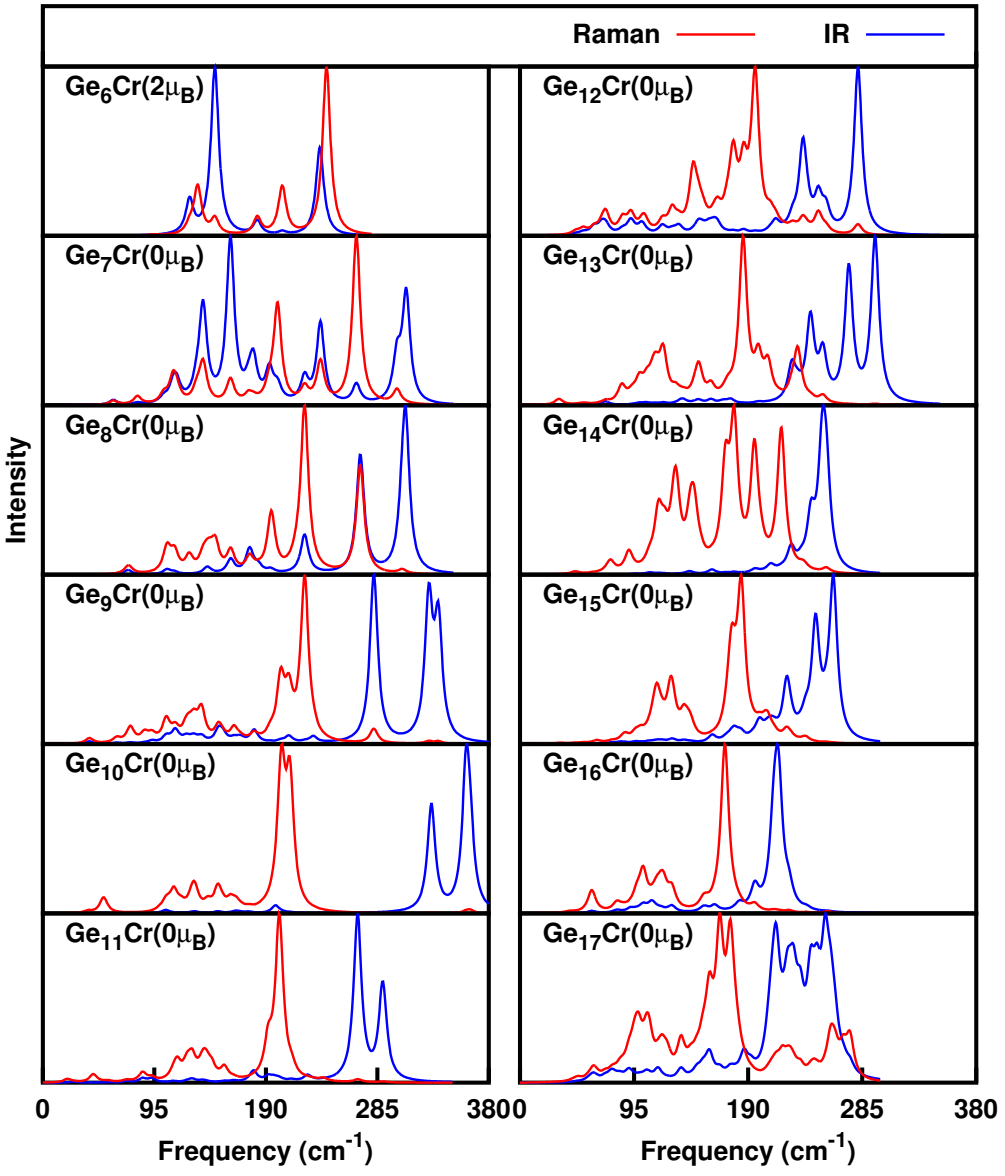

Figure 4.7: Variation of IR and Raman spectrum. The intensity is plotted in an arbitrary unit.

particular CP is characterized by (R, S) where R is the rank of the Hessian matrix of the electron density reflecting the number of Eigen values of the matrix and S is the sign of the sum of the Eigen values (either maxima or minima or saddle) indicating the topological feature. A bond critical point (BCP) in general represented by the

(3, -1) CP reflects the saddle point between two molecules or clusters forming bonds between them. With this background, we have calculated the BCPs and this is shown in Fig. 4.1. First we have calculated the location of the (3, -1) CPs. It is clearly seen that in all endohedrally doped clusters, a number of (3, -1) CPs inside the cages are almost uniformly distributed surrounding the encapsulated Cr atom and the number varies from cluster to cluster. The 10 (3, -1) CPs are indicating the existence of 10 bonds between the Cr and germanium atoms in $CrGe_{10}$. The number of Ge–Ge bonds for the clusters in the size range n = 6–12 varies between 16–18, and then it starts increasing with a maximum value of 39 at n = 16. Among several isomers (10) in $CrGe_{16}$, the ground state structure is a well known Frank–Kasper polyhedron[35], which is stable in general. For the cluster with n = 6 to 15, Cr is attached with all Ge atoms in the cage and hence the number of bond critical points (BCPs) is the same as the number of Ge atoms in the cage. Whereas, due to the larger size of the Ge_{16} and Ge_{17} cages, the Cr atom won't be able to form bonds with a number of the Ge atoms in the cage and hence the number of BCPs drops. This could be taken as the structural phase change from the bonding point of view. Following the variation of the BCPs with the cluster size (Fig. 4.6), it increases linearly from n = 8 to 14. The maximum value of the BCP (3, -1) at n = 14 is an indication of a strong structural stability with C_{2V} symmetry. Though there is no local maxima in the BCPs variation at n = 10, there is a clear increasing trend. The maximum value of the Ge-Ge bond at n = 16 is the indication of the stable nature of the pure Ge_{16} cage. There is also a local peak at n = 10 in the number of the Ge–Ge bond variation. Therefore, variation of the BCPs and also the number of Ge–Ge bonds in the germanium cages help to understand the stability of the clusters from the structural point of view[33].

With reference to the IR and Raman frequencies (Fig. 4.7) of the clusters from n = 6 to 17, at n = 10, 14 and 16, the number of dominating frequencies is much lower than that of the other structures. A lower number of modes in IR is basically the indication of the vibration of the bonds (stretching) present in the structure at an almost constant frequency or within a very small frequency range. This is because of the strong structural symmetry for n = 10, 14 and 16. Raman frequency in general indicates the bending mode in the clusters. The narrow peak at n = 10, 11 and 16 in the Raman spectrum indicates the lower number of bending modes present in these clusters with a breathing mode (where all the molecules in the cage vibrate in phase), with a maximum intensity at 210, 201 and 170 cm^{-1} respectively.

4.3.4 Cr atom contribution in DOS

To understand the strength of the Ge and Cr-d orbital contributions in hybridization and the cause of the magnetic moment quenching of Cr in the clusters, we have studied PDOS (Fig. 4.8, 4.9, 4.10), and the percentage of the Cr d-alpha and beta orbital contribution in hybridization, shown in Fig. 4.11.

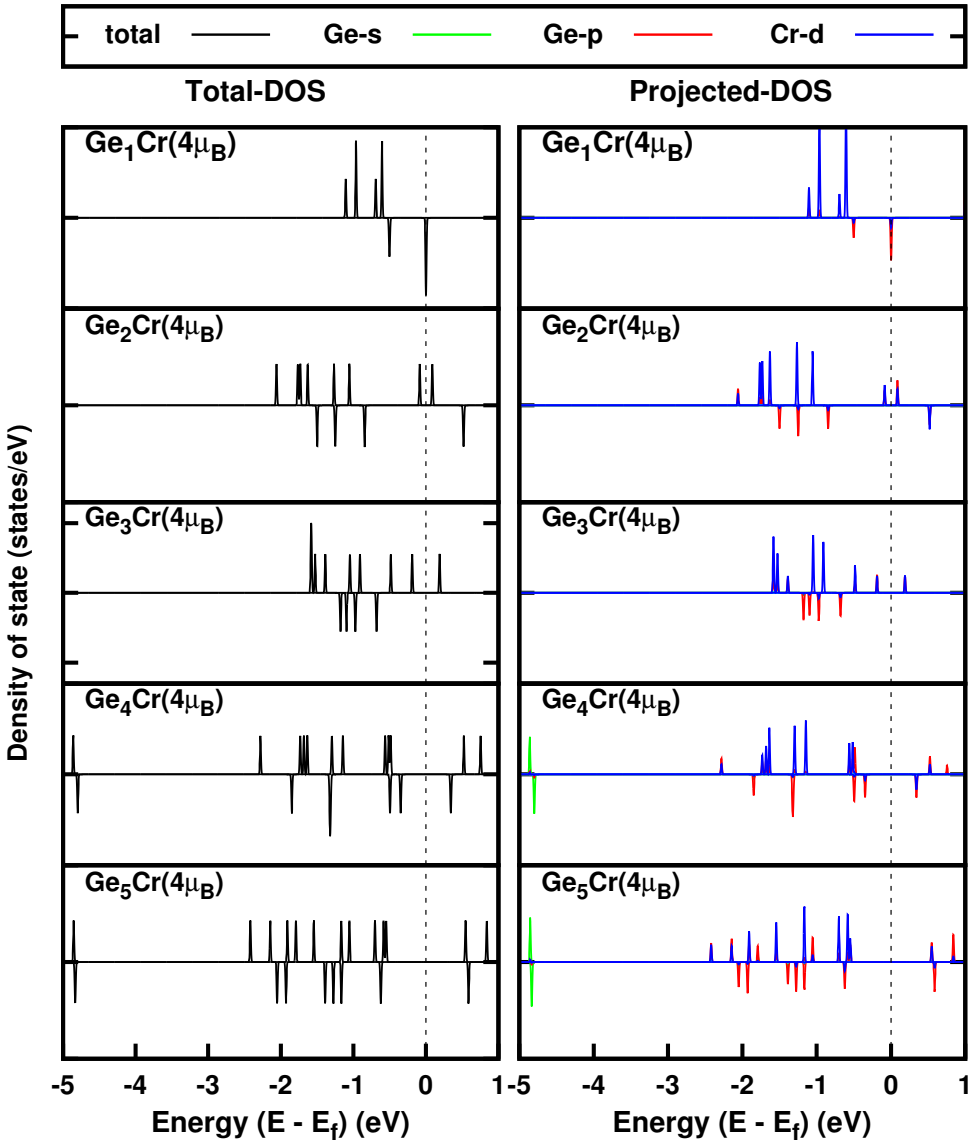

Figure 4.8: Variation of DOS and PDOS of different neutral clusters of $CrGe_n$ (n = 1–5) with shifted energy ($E-E_F$) and Fermi energy set to '0'.

Since n = 1–6 are in quintet or in triplet spin states, their PDOS is asymmetrical (Fig. 4.8, 4.9, 4.10). For other clusters, in singlet spin states, both the alpha and beta contributions in PDOS are identical. In all the stable clusters, there is no contribution

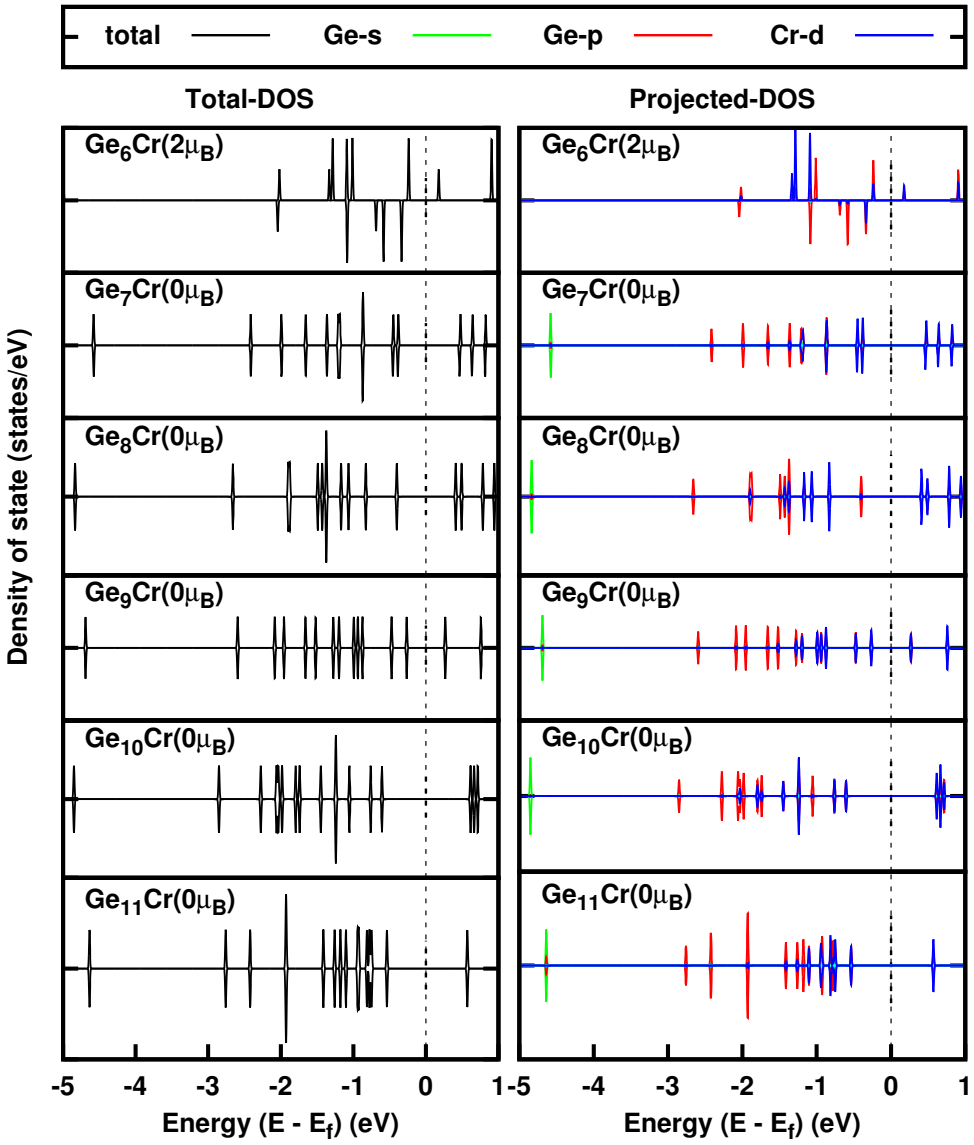

Figure 4.9: Variation of DOS and PDOS of different neutral clusters of $CrGe_n$ (n = 6–11) with shifted energy (E-E_F) and Fermi energy set to '0'.

of DOS on the Fermi level and the HOMO–LUMO orbitals are also clearly separated. The percentage contribution of the Cr d-orbital in hybridization also supports the DOS nature.

For n = 6, the percentage contributions in hybridization of the Cr-d alpha and beta are not the same. Therefore, it is clear that the existence of the magnetic moment is due to the unequal alpha and beta Cr -d orbital contribution in the hybridization. With the increase of the size of the clusters from n = 1 by adding Ge atoms one by one, the chances of hybridization between the Cr and the Ge atoms increases. Due to this hybridization the Cr d-orbital, which is responsible for the magnetic moment of Cr, decreases and

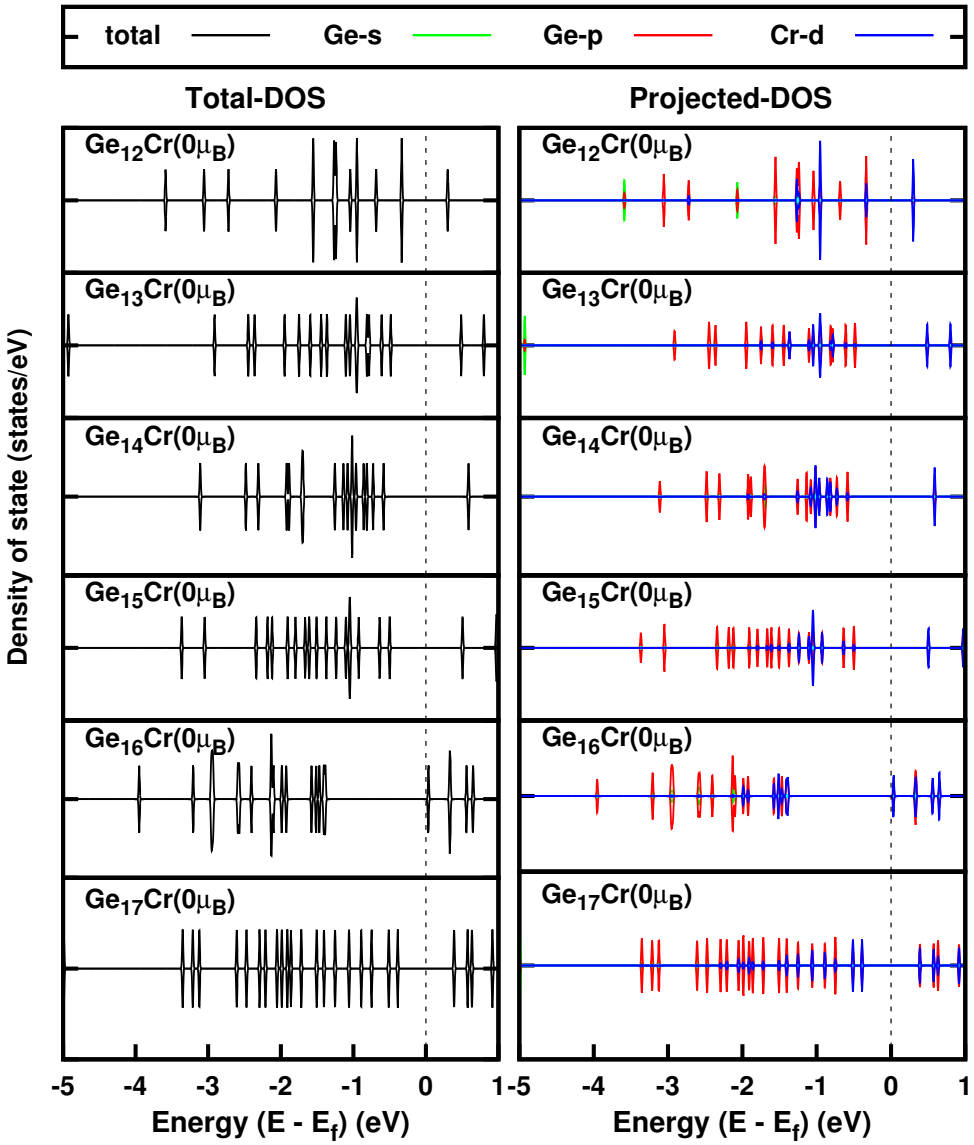

Figure 4.10: Variation of DOS and PDOS of different neutral clusters of $CrGe_n$ (n = 12–17) with shifted energy (E-E_F) and Fermi energy set to '0'.

hence the magnetic moment of Cr quenches. So the existence of the magnetic moment or the quenching of the magnetic moment of $CrGe_n$ is due to the hybridization between the Ge p- and Cr d-orbital contribution. In the case of n = 16, the number of Ge–Ge bonds are at the maximum in the whole series of study (Fig. 4.6). This is the indication of the stable nature of the Ge_{16} germanium cage. In the clusters, the magnetic moment or the quenching of the magnetic moment is due to the hybridization between the Ge p- and Cr d-orbital contribution. In all the stable clusters, there is no contribution of DOS on the Fermi level and the HOMO–LUMO orbitals are also clearly separated.

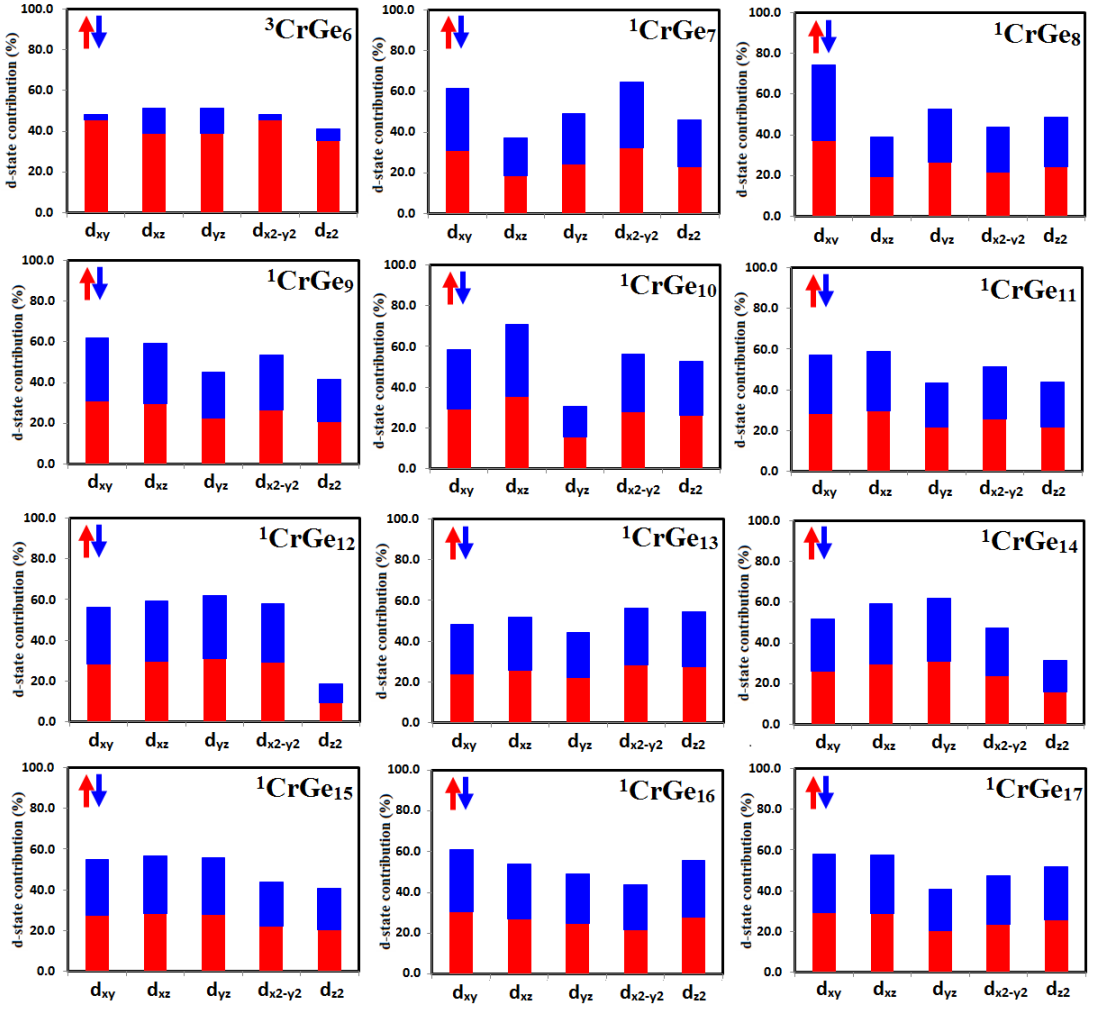

Figure 4.11: Percentage of alpha and beta Cr d-orbital contributions in hybridization with the Gen (n = 6–17) cages.

4.4 Conclusions

The variation of the different energy parameters BE, EE, FE, stability, HOMO–LUMO gap, VIP, AIP, ADE and VDE of the clusters supports the enhanced stability at n = 10 and 14. The above results point to a more unified picture for the stability of $CrGe_n$ clusters. We have verified the electron-counting rule on the basis of the Cr atomic filled shell in molecular orbitals. Analysis of the Cr atomic shell contributions in molecular orbitals explained the stable nature of the $CrGe_{10}$ and $CrGe_{14}$ clusters. However, $CrGe_{12}$ is less stable due to the 16 electrons in the Cr shell, with an electronic configuration of $4S^2$, $4P^6$, $3d^8$. In the $CrGe_{12}$ cluster, due to the crystal field like splitting, Cr- $3d_{z^2}$ pushed up to the LUMO. However, $CrGe_{10}$ and $CrGe_{14}$ both have a Cr atom with the electronic configuration of $4S^2$, $4P^6$, $3D^{10}$, which is a close filled configuration and follow

the 18 electron counting rule. The analysis of the bond critical points indicates that the more stable species have a higher number of BCPs, which leads to an increase in the germanium binding energy. The other significant effect, however, is the mixing between the Cr 3d- and Ge p-states, which was reflected in the PDOS and quenching of the Cr magnetic moments in the clusters. The bonding nature and the vibrational modes present in the clusters can be further understood by the study of the IR and Raman frequencies as discussed. A lower number of modes in the IR and Raman spectra is basically indicating the higher symmetry in the clusters.

Chapter 5

Au doped Germanium nanoclusters and building blocks

5.1 Introduction

In this chapter, the electronic structure, stability and shell closing model of Au doped Ge_n^- nanoclusters has been carried out using density functional theory (DFT). From the nature of the variation of the different thermodynamic and chemical parameters, the $AuGe_7^-$ and $AuGe_{10}^-$ ground state clusters are identified as the most stable species. It is observed that the enhanced stability of $AuGe_7^-$ is due to the closed shell filled structure of the Au-atomic orbitals and follow the magic shell closing number (40). In this chapter, we have examined the building blocks of small sized clusters and taken Au^- as connector or bridge between two Ge_n species.

5.2 Computational Details

Complete calculations are splitted into two parts mainly. All geometry optimizations were performed with no symmetry constraints. We again used a global structure predictor method using USPEX (Universal Structure Predictor: Evolutionary Xtalloraphy)[146] and VASP (Vienna AB-initio simulation package)[147] to get all the possible optimized geometric isomers in each size, from n = 2 to 20. VASP code has been used to relax the structures predicted by USPEX. For this, we have used a combination of the few-set of pseudo-potentials available in VASP. In the next stage of optimizations and post optimization calculations, the last few low energy isomers obtained from

USPEX and VASP were reoptimized at different spin states in Gaussian'09[148] to obtain different energy parameters. Here, all calculations were performed within the framework of a linear combination of the atomic orbital's density functional theory (DFT). The exchange-correlation potential contributions are incorporated into the calculation using the spin-polarized generalized gradient approximation (GGA) functional proposed by Lee, Yang and Parr popularly known as B3LYP[116] available in Gaussian'09. Different basis sets were used for Au and Ge. LanL2DZ with effective core potential (ECP) basis set is used for Au and LanL2DZdp with effective core potential (ECP) obtained from the EMSL basis set exchange[150] are used for germanium to express the molecular-orbitals of all atoms as linear combinations of atom-centered basis functions. LanL2DZdp is a double-basis set with a LANL effective core potential (ECP) and with polarization function[118,151]. Unless specified otherwise, the results presented are obtained using the Gaussian'09 program package.

5.3 Results and discussion

Variations of the different thermodynamic and chemical parameters during the growth process provide the initial evidence to identify the stable nanoclusters. We have studied the growth of the Au doped Ge_n^- clusters within the size range n= 1 to 20.

5.3.1 Structural and growth mechanism of the clusters

A number of isomers have been calculated in each size. The most stable ground state isomer along with few lowest energy isomers (n=8 to 20) size are shown in Fig. C.1, C.2 and C.3 and the ground state structures are shown in Fig. 5.1. Initially, at small size (n=1-6), clusters are having some specific point group symmetries. In the present study, we examined the role of gold atom in Ge_n clusters. Due to the bigger size of gold atom compare to other TM atoms studied in the thesis, gold prefers to stay on the surface of the germanium clusters up to the size n=10. At n=7,8,9 and 10, the structures are interesting due to the gold positions. In the ground state clusters $Au@Ge_7$ and $Au@Ge_{10}$ gold has higher ability to make bonds with other foreign cluster or atoms. We exploit this to use gold as a bridging atom between two germanium clusters. With this aim, we modeled $AuGe_{14}^-$ and $AuGe_{20}^-$ where gold acted at bridging atom and connected to Ge_7 and Ge_{10} clusters respectively. However, particularly on n=7 and 10, it could be possible that gold has dangling bonds and still reactive. For that, we prepared few building

block structures and found some interesting results. Cluster size n=7 gives $AuGe_{14}^-$ (ground state structure) where Au plays a role of connector between two Ge_7 clusters species. Similarly at n=10, Au becomes the connector between two Ge_{10}^- clusters and make $AuGe_{20}^-$. In the bigger sized ground state clusters (n>10), gold always absorbed endohedrally and there is no scope of using Au as a bridging atom. However, the ground state $AuGe_{14}^-$ and $AuGe_{20}^-$ are made of Ge_7 and Ge_{10} clusters as building blocks.

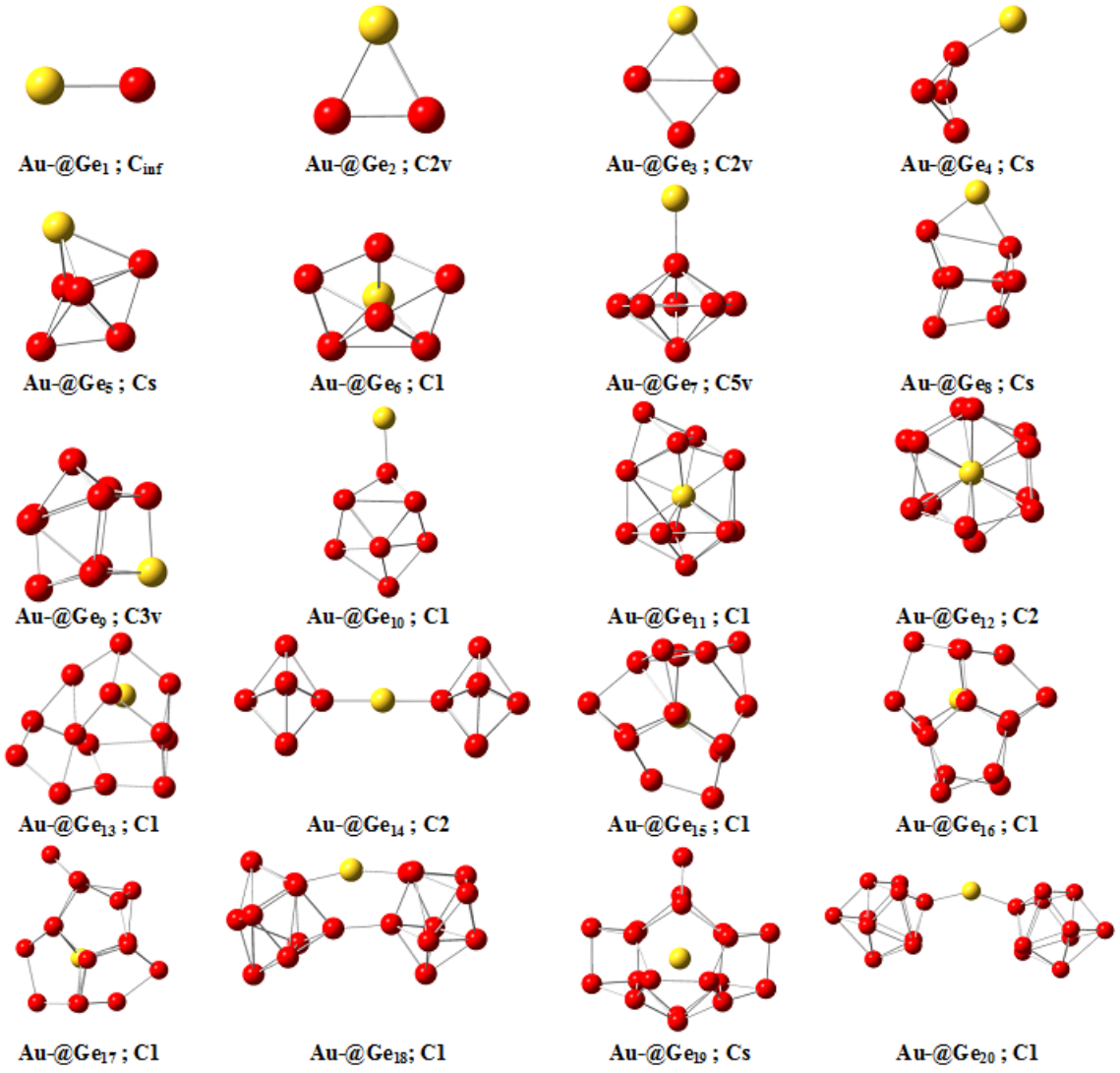

Figure 5.1: Ground state geometries of $AuGe_n^-$ (n = 1–20). Red and yellow spheres are denoting the Ge and Au atoms, respectively.

5.3.2 Energetics of clusters

It is also important to obtain the relative stability of different clusters in a particular composition to identify the most stable size in the series so that it can be used as the building blocks in cluster assembled materials. To explore the relative stability of the clusters with the increase of the cluster size during the growth process, we have studied different thermodynamic and chemical parameters, such as, average binding energy per atom (BE), embedding energy (EE), fragmentation energy and the 2^{nd} order change in energy, as mentioned in various report [42,120,122–125]. These parameters are defined as:

$$\left.\begin{aligned} BE &= -\left[E(Ge_nAu^-) - nE(Ge) - E(Au^-)\right]/(n+1) \\ EE &= E(Ge_n) - E(Au^-) - E(Ge_nAu^-) \\ \Delta(n, n-1) &= E(Ge_{n-1}Au^-) + E(Ge) - E(Ge_nAu^-) \\ \Delta_2(n) &= E(Ge_{n+1}Au^-) + E(Ge_{n-1}Au^-) - 2E(Ge_nAu^-) \end{aligned}\right\} \quad (5.1)$$

Where, E(Au^-), E(Ge), E($AuGe_n^-$) represent the total energies of Au^-, Ge and $AuGe_n^-$ cluster respectively. Again for pure Ge_n cluster E(Au^-) in the above-mentioned equation is taken, as zero and n+1 will be replaced by n.

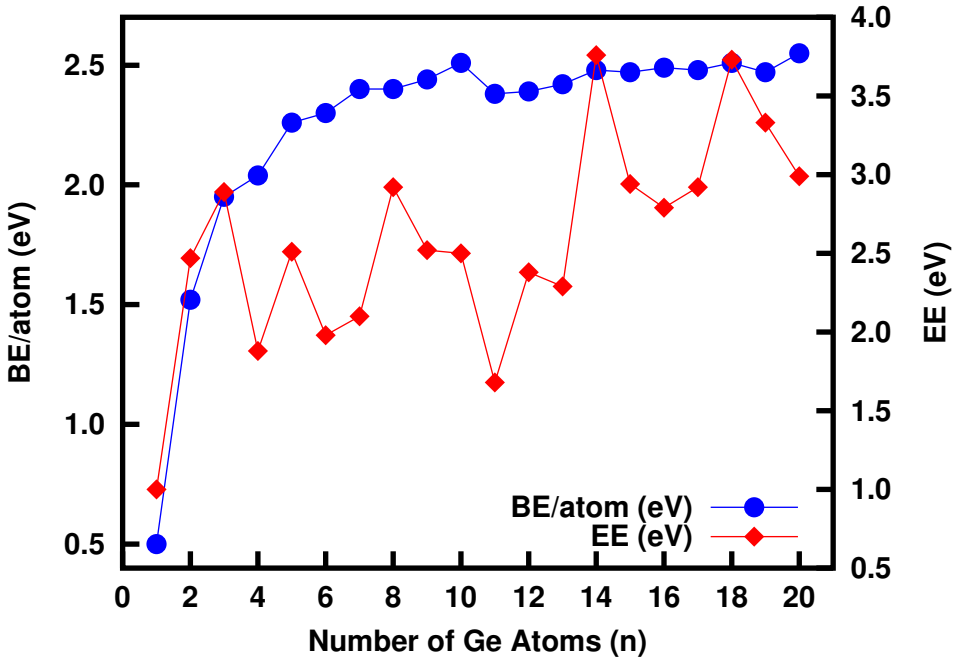

Figure 5.2: Variation of average binding energies and embedding energies with the size of the clusters $AuGe_n^-$ (n = 1–20).

In Fig. 5.2, Variation of average binding energies and embedding energies with the

size of the clusters $AuGe_n^-$ (n = 1–20) are shown. Initially, Average binding energies are showing increasing trend. At n=7, 10, 14, 16, 18 and 20 are the local peaks in BE/atom variation. Embedding energy are showing the local maxima at n=3, 5, 8, 12, 14 and 18. It is interesting to note that embedding energy does not show any peak at n=7 and 10. This is due to the position of gold atom on the Ge_n surface. By definition, embedding energy is the required energy to remove the dopant atom (Au in this case). Since Au atom is already on the surface of Ge_7 and Ge_{10} clusters. So the variation of embedded energy graph does not follow the binding energy graph. In other bigger sized clusters, these two graphs are more or less similar in nature. In Fig. 5.3, The variation of

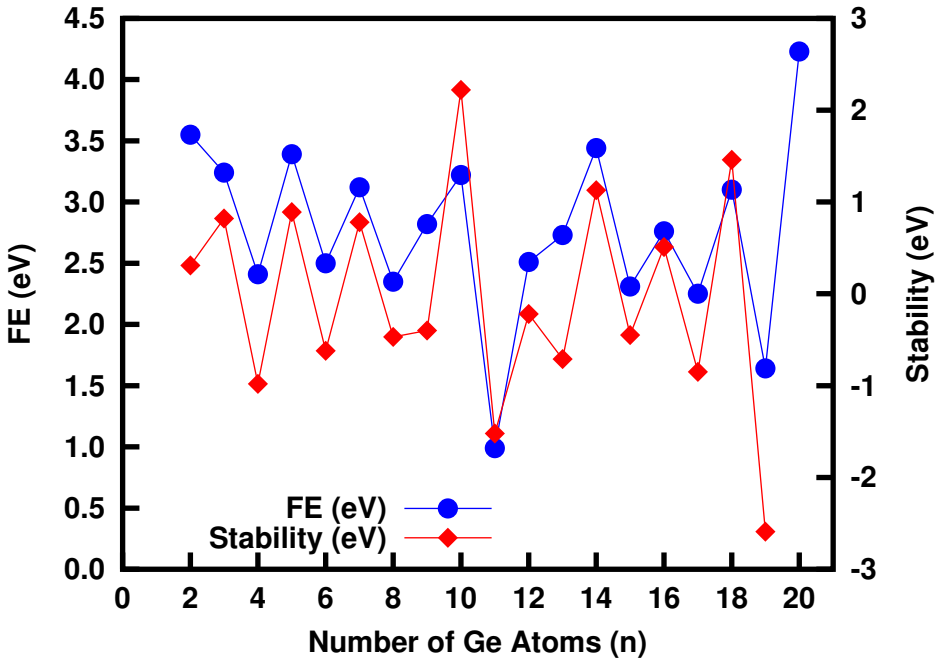

Figure 5.3: Variation of fragmentation energy and stability parameters with the size of the clusters $AuGe_n^-$ (n = 1–20).

fragmentation energy and stability parameters with the size of the clusters $AuGe_n^-$ (n = 1–20) are shown. All the local peaks are identical at n=5, 7, 10, 14, 16, 18 and 20 for both fragmentation energy and stability. In Fig. 5.3, variation of HOMO-LUMO gap with the cluster size are shown. Again n=3, 7, 10, 15, 18 and 20 are showing local peaks. In fact the maximum values are stand at n=7 and n=10 sized clusters which again show that these clusters are thermodynamic and chemically stable. Gap for n= 14 is giving different result. This could be due to the unsaturated dangling bonding in germanium cluster. This is also applicable in $AuGe_{20}^-$ cluster. The variation of detachment energies with the size of the clusters $AuGe_n^-$ (n = 1–20) are shown in Fig. 5.5. Lu et al.[158] measured the

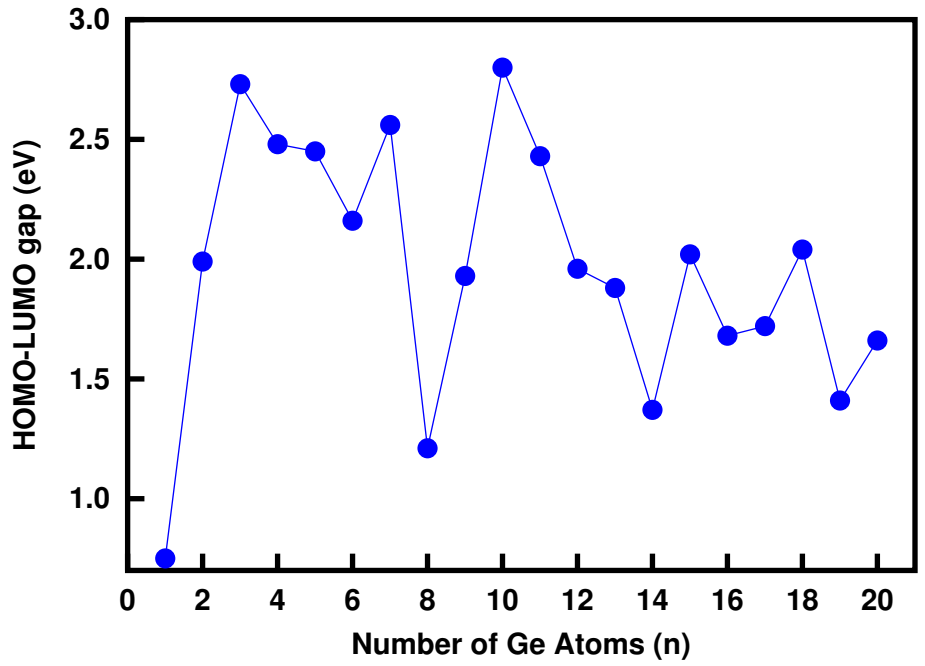

Figure 5.4: Variation of HOMO-LUMO gap with the size of the clusters $AuGe_n^-$ (n = 1–20).

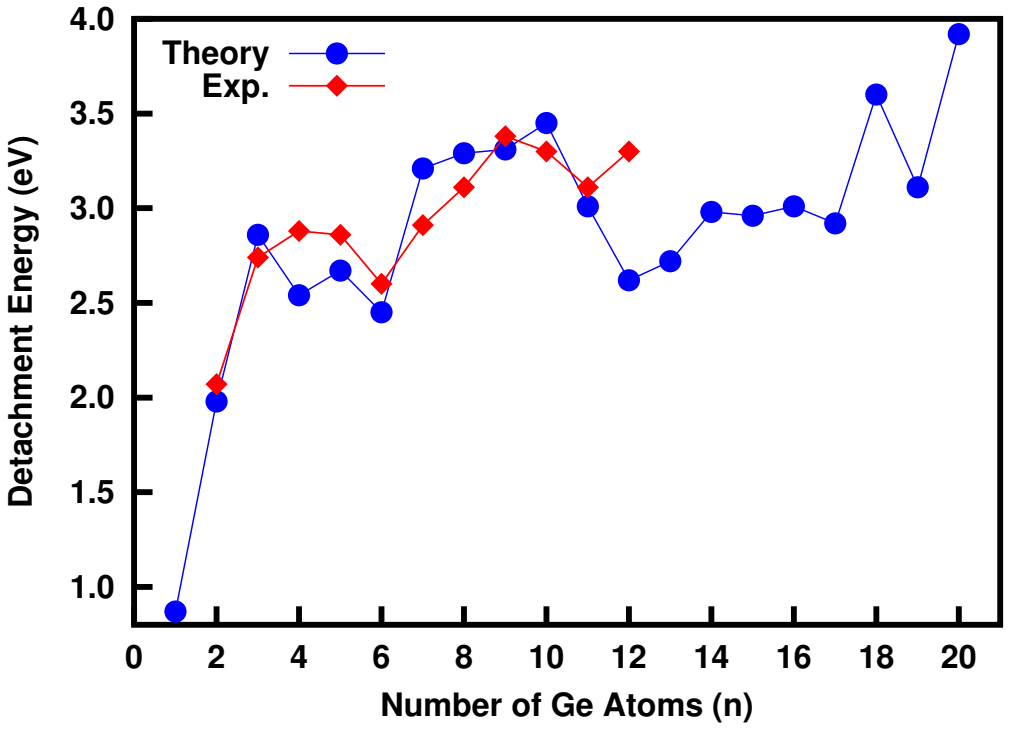

Figure 5.5: Comparison of theoretical results with experimentally predicted detachment energies, where experimental results are measured on the cluster size from n=1 to 12 .

detachment energy and electron binding energy of $AuGe_n^-$ clusters experimentally within the size range of n=1 to 12. Our calculated detachment energies are in good agreement with the experimental results reported by Lu et al.[158]. Theoretical and experimental values are more or less similar. Local peaks are again at n=5, 7, 10, 14, 18 and 20 which compliment our previous results. By applying shell closing model, we can explain the enhanced stability of n=7, 14 and 20 sized clusters. Since each Ge and Au atoms have four and 11 valance electrons respectively, therefore, $AuGe_7^-$, $AuGe_{14}^-$ and $AuGe_{20}^-$ clusters are holding total 40, 68 and 92 number of valance electrons. As per the Hund's rule these numbers are the magic numbers and the clusters holding this numbers are valance electrons are suppose to be the magic clusters.

5.3.3 Stability of $AuGe_7^-$ and $AuGe_{14}^-$ clusters

Following our previous discussion, we have selected $AuGe_7^-$ and $AuGe_{14}^-$ clusters for further investigations. We have calculated the density of states, projected density of states along with IR and Raman spectra of $AuGe_7^-$ and $AuGe_{14}^-$ clusters. Calculated results are shown in Fig. 5.6. Comparing the DOS and PDOS of these two clusters, it can be seen that the reduced value of band gap is mainly due to the presence of Ge orbital contribution. This results supports the reduced value of HOMO-LUMO gap in $AuGe_{14}^-$ cluster. Comparing the modes of IR and Raman spectrum in these two clusters. It is found that the number of modes are always less in $AuGe_{14}^-$ compare to $AuGe_7^-$.

For $AuGe_7^-$, the dominating modes in IR frequencies are 193.22 cm^{-1} and 241.43 cm^{-1}. In Raman spectrum, the dominating frequencies are coming at the same values as IR with 241.43 cm^{-1} as breathing mode. On the other hand in $AuGe_{14}^-$ cluster, the dominating IR modes are coming at 149.27 cm^{-1}, 174.70 cm^{-1} and 232.09 cm^{-1}, whereas the dominating Raman mode is coming at 237.77 cm^{-1} (breathing mode). Comparing the vibrational modes in IR and Raman spectra, it seems that both the visible Raman frequencies shifted towards the lower value when a single Au^- atom joining two Ge_7 clusters. Also, the intensity of the dominating mode is much higher than the other modes present in $AuGe_{14}^-$. As if, the growth of the intensity of the dominating mode in the bigger cluster is in expenses of the lower modes present in $AuGe_7^-$ cluster. This is the indication of higher stability of $AuGe_{14}^-$ cluster.

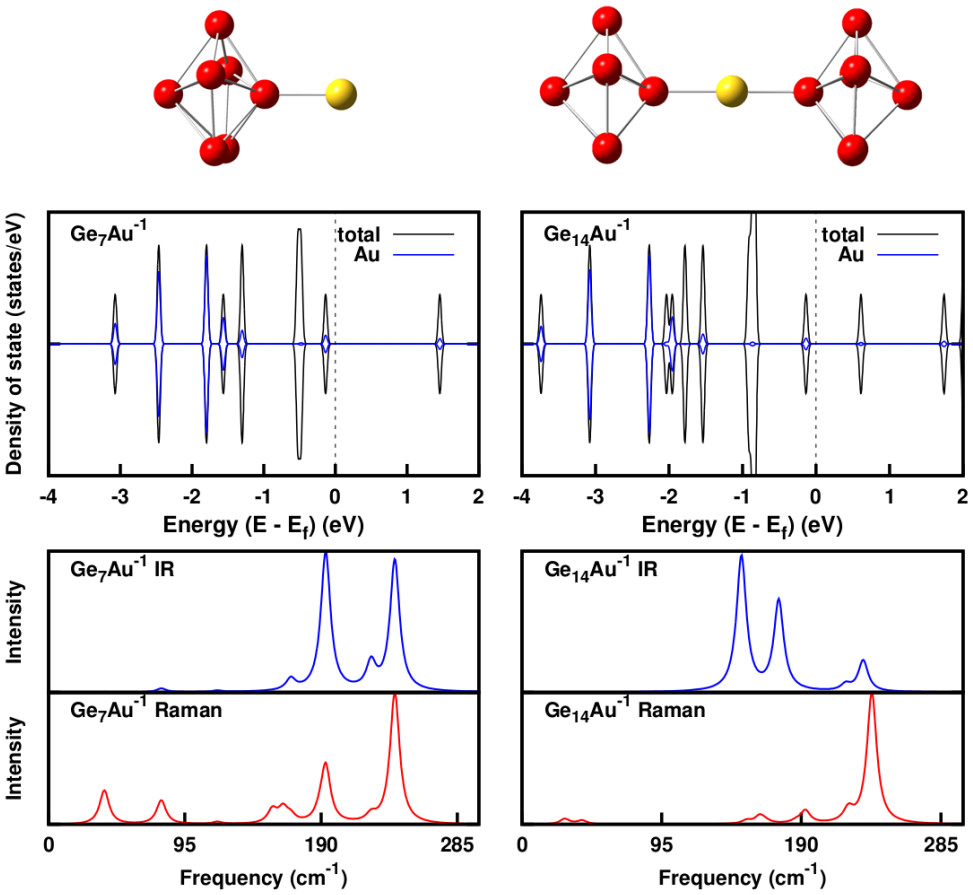

Figure 5.6: Building blocks of $AuGe_7^-$ and $AuGe_{14}^-$. Density of state, IR and raman is also showing.

5.3.4 Stability of $AuGe_9^-$ cluster and $AuGe_{18}^-$ cluster assembly

In the whole series, the second cluster assembly is $AuGe_{18}^-$ which have been formed by adding Ge_9 clusters where Au acted as a bridge. Ugrinov et al.[159], reported the orientation and stability of $[Ge_9{=}Ge_9{=}Ge_9]^{6-}$ cluster. As per the cluster composition and symmetry it is basically two Ge_9^{4-} clusters linked by another Ge_9^{4-} cluster which can be explained by Wade-Mingos rule. It is a nido cluster, so formed a capped square anti-prism. Each Ge vertex of Ge_9^{4-} has a lone pair, so it might be possible that it can remove 2 electrons from the cluster for each Ge-Ge bond between Ge_9 units which would give $(Ge_{27})^{4-}$ [3 x Ge_9^{4-} = $(Ge_{27})^{12-}$ - 8 electrons = $(Ge_{27})^{4-}$].

According to this argument, it explains the 6- charge is that one combination of Ge-Ge anti-bonding orbitals is stabilized because the Ge-Ge bonds do not lie along the

Table 5.1: IR and Raman frequencies of $AuGe_n^-$ (n=7, 9, 10, 14, 18 and 20) clusters and cluster assemblies.

Cluster	IR frequencies (in cm^{-1})	Raman frequencies (in cm^{-1})
$AuGe_7^-$	193.22	193.22
	241.43	241.43
$AuGe_{14}^-$	149.27	161.74
	174.70	192.77
	232.09	222.12
		237.99
$AuGe_9^-$	176.69	174.11
	234.56	203.41
		212.30
$AuGe_{18}^-$	108.05	189.40
	139.02	204.53
	169.55	227.36
	227.36	237.33
		241.63
		247.98
$AuGe_{10}^-$	153.77	72.27
	240.15	196.80
		240.15
$AuGe_{20}^-$	71.15	24.76
	116.89	25.21
	140.06	117.61
	189.91	169.62
	206.73	198.67
	217.18	210.43
		218.57

Table 5.2: Bond lengths of Au-Ge in $AuGe_n^-$ (n=7, 9, 10, 14, 18 and 20) clusters and cluster assemblies.

$AuGe_7^-$	$AuGe_9^-$	$AuGe_{10}^-$	$AuGe_{14}^-$	$AuGe_{18}^-$	$AuGe_{20}^-$
2.49 Å	2.55 Å	2.45 Å	2.58 Å	2.50 Å	2.55 Å
	2.62 Å		2.57 Å	2.58 Å	2.55 Å

'natural' direction of the radial lone pairs, so are strained in some sense.

In our case, by adding two Ge_9 clusters where Au atom acted as a bridge to form $AuGe_{18}^-$ cluster assembly which is comparable to the structure reported by Ugrinov et al.[159].

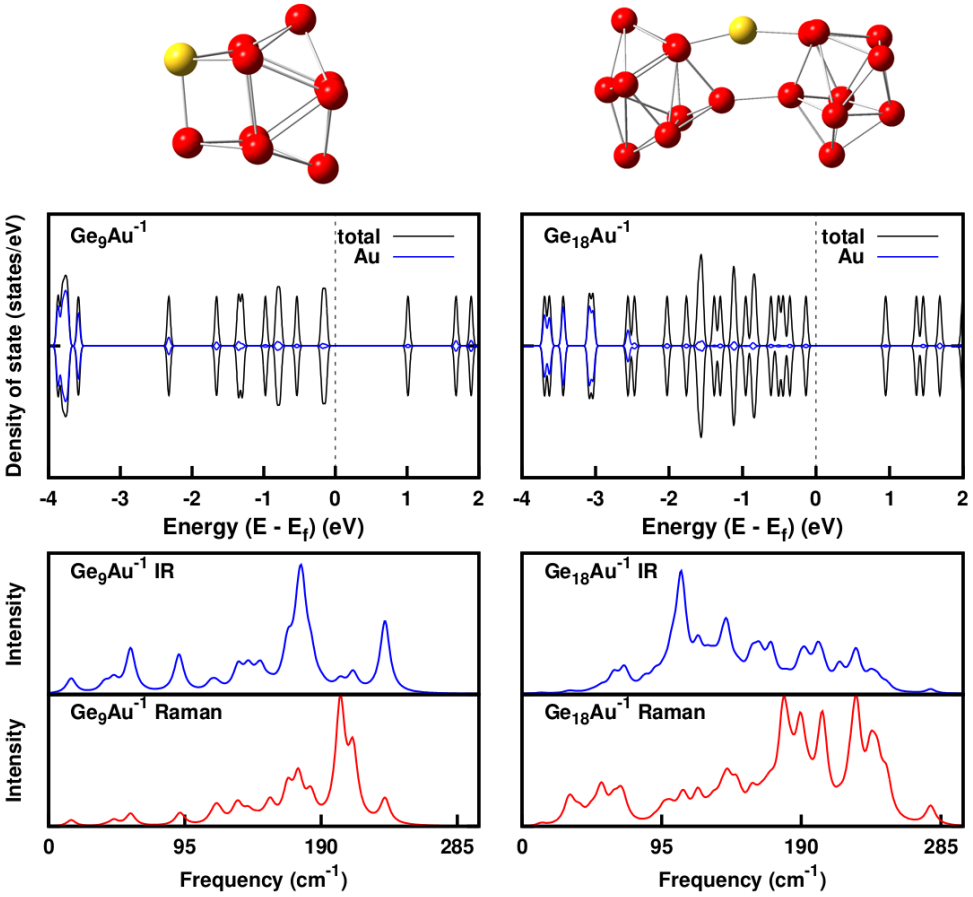

Figure 5.7: Building blocks of $AuGe_9^-$ and $AuGe_{18}^-$. Density of state, IR and raman is also showing.

5.3.5 Stability of $AuGe_{10}^-$ and $AuGe_{20}^-$ clusters

The third stable cluster assembly is $AuGe_{20}^-$ form by two Ge_{10} clusters and Au atom. The DOS and PDOS of $AuGe_{10}^-$ and $AuGe_{20}^-$ cluster are shown in Fig. 5.8 along with IR and Raman spectra. Detailed frequency analysis is given in table. In Fig. 5.8, DOS and PDOS shows a large band gap for $AuGe_{10}^-$ cluster while comparative smaller gap is for $AuGe_{20}^-$ clusters assembly.

In IR spectrum, a dominant peak for $AuGe_{10}^-$ cluster at 240.15 cm^{-1} as shown in breathing modes but after adding the Ge_{10} unit, there are multiple peaks are occurring which is due to the rotation of both the Ge_{10} units in opposite direction. In the other hand in raman spectrum shows a peak shift from 196.05 cm^{-1} to 210.34 cm^{-1} for $AuGe_{10}^-$ and $AuGe_{20}^-$ respectively. This is due to the band at Au docking site with both the additional Ge_{10} units.

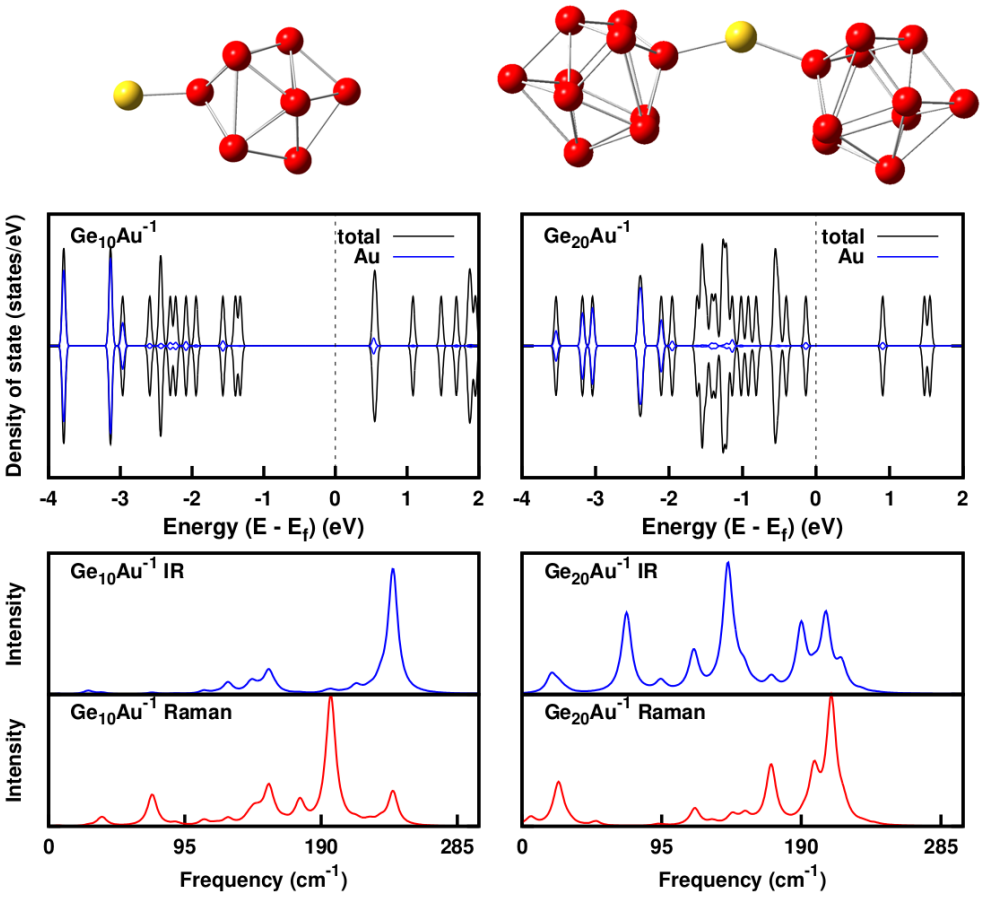

Figure 5.8: Building blocks of $AuGe_{10}^-$ and $AuGe_{20}^-$. Density of state, IR and raman is also showing.

5.4 Conclusions

In summary we have done theoretically study of the electronic and vibrational properties of Au doped Ge_n clusters at different sizes in cationic states. The variation of the different energy parameters BE, EE, FE, stability, HOMO–LUMO gap and DE of the clusters supports the enhanced stability at n = 7, 10, 14, 18 and 20. The above results point to a more unified picture for the stability of $AuGe_n^-$ clusters. Shell closer magic numbers also plays an important role. By applying shell closing model, we can explain the enhanced stability of n=7, 14 and 20 sized clusters. Since each Ge and Au atoms have four and 11 valance electrons respectively, therefore, $AuGe_7^-$, $AuGe_{14}^-$ and $AuGe_{20}^-$ clusters are holding total 40, 68 and 92 number of valance electrons. As per the Hund's rule these numbers are the magic numbers and the clusters holding these numbers of valance electrons are suppose to be the magic clusters. But it needs more detailed analysis to explain the orbital sequence following Hund's rule in these clusters.

Chapter 6

Functionalized Cluster Assembled TM doped Si Nanotubes

6.1 Introduction

In this chapter, we have discussed the transition metal (TM=Cr, Mn and Fe) doped silicon nanotubes with tunable band structure and magnetic properties by the careful selection of cluster assembly as building blocks using first-principle density functional theory. We found that the transition metal doping or hydrogen termination process can stabilize the pure silicon nanoclusters or cluster assemblies and it could be extended as ferro- and antiferro- magnetic nanotubes with finite magnetic moments. Study of the band structures and density of state (DOS) of different empty and TM doped nanotubes (Type 1 to Type 4) show that these nanotubes are useful as metal, semiconductor, semi-metal and half–metals. These designer magnetic materials could be useful in spintronic sand magnetic devices of nanoscale order.

6.2 Computational Details

Density-functional calculations are performed by using plane-wave pseudo-potential methods.[92,160] The density functional is treated by the generalized gradient approximation (GGA) with the exchange-correlation potential parameterized by Perdew, Burke and Ernzerh(PBE)[104]. All the calculations are performed in VASP (Vienna Ab Initio Simulation Package) computational code[161]. Relaxations are carried out using conjugate-gradient algorithm[162]. The kinetic-energy cutoff of plane wave is set

at different values depending upon the TM doping in between 320 eV to 360 eV. Lattice parameters and ionic positions are adjusted until all components of Hellman-Feynman force on each ion were less than 0.001 eV/Å. We have checked the band structure and DOS calculation using both hybrid functional Heyd-Scuseria-Ernzerhof (HSE) as well as Becke 3-parameter, Lee-Yang-Parr (B3LYP) in addition to PBE at the initial stage of the work. We find negligible difference in band gap by the band structures, and DOS in calculated using PBE, PBE0, HSE and B3LYP hybrid functional (Fig. D.5). The main cause of this is involved in the presence of lesser number of electrons in the d-block of the transition metal elements used in each cell of the nanotubes. To construct the nanotubes, we use 2 d-block transition metal atoms. The total number of the d-electrons in these atoms is much lesser than the number of electrons in Si atoms present in the cell. Hence, the effective correction of the hybrid functional does not show visible changes in the band structure and DOS behavior. This is very common in a system where number of d-block elements and d- block electrons are less in unit cell. Two set of calculations are preformed to achieve the minimization of energy, volume variation for cell relaxation, and ion relaxation. In case of non-periodic systems, such as the individual cluster or cluster dimer or higher, we have used a large super cell with a sufficiently large cell length. During optimization, all internal coordinates of the Si, Cr, Mn and Fe atoms are allowed to relax with respect to any one atom among them. At the same time the lattice constants are kept constant. Following this restrictions in optimization a cluster is separated from nearest cell's cluster by 12-13 Å to make the external force on a particular cell zero or negligible. For the infinite nanotube, k-mesh is taken as 1D system for all the nanotubes. Cell is taken in such a way that tubes can form in one direction as like 1D system. In each calculation 12 sets of k-points are taken to define the cell.

6.3 Results and discussions

6.3.1 Empty nanotubes

The main restriction to form empty finite silicon nanotubes or tube like cluster-assembled materials is the sp^3 type of hybridization in Si-Si bonding. It leads to deform the finite size nanotubes formed by cluster assemblies. To verify the effect of hydrogen terminations, we have added hydrogen atoms at the two ends of the tubular structures.

Formation of stable transition metal doped or hydrogenated tubular cluster indicates the possibility of formation of nanotubes of different types using small clusters as units. As an initial step of calculations, we first select the stable isomers in the sizes Si_{12}, Si_{16}, Si_{20} and Si_{24}empty cages[163,164].

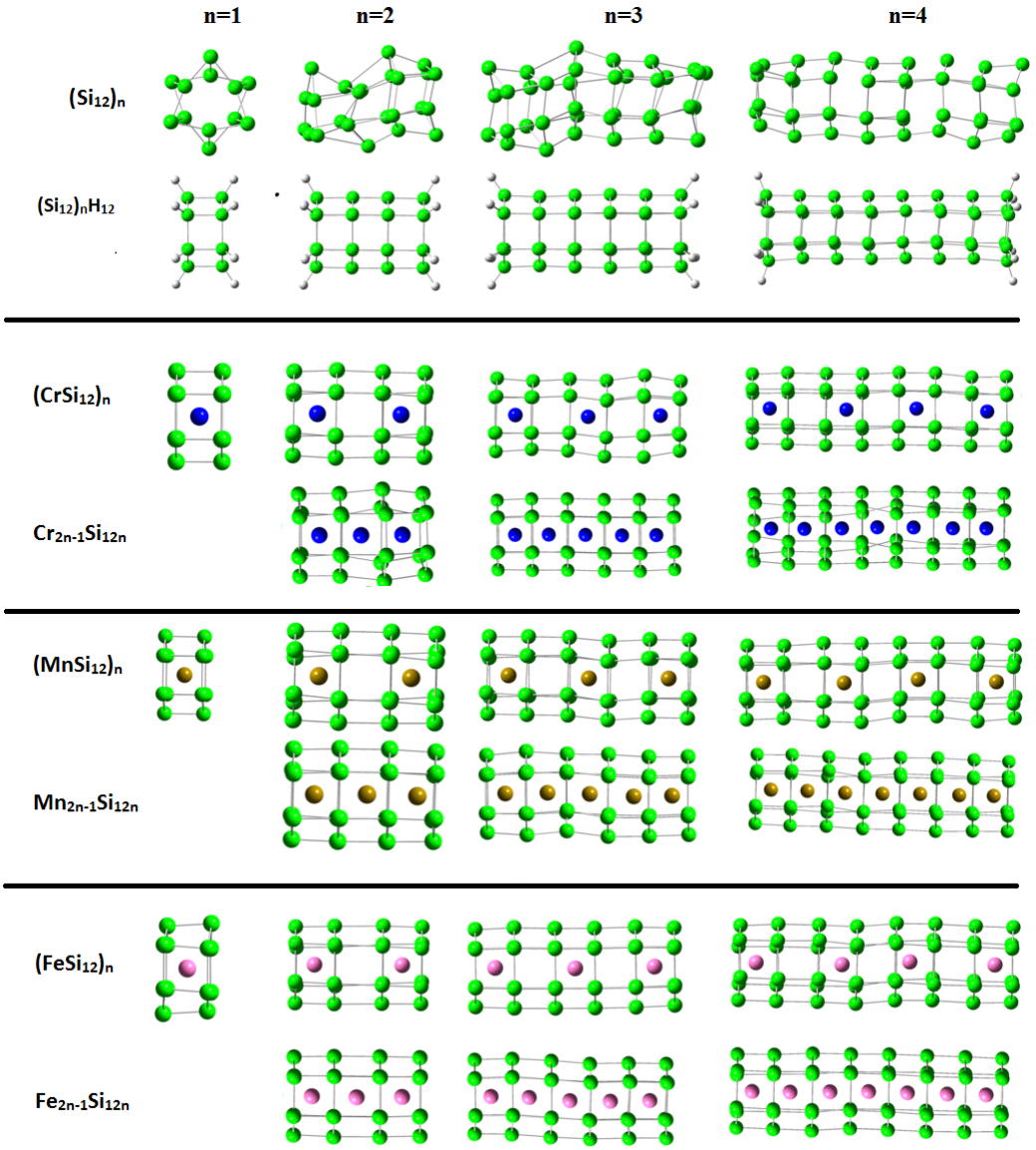

Figure 6.1: Structures of hollow finite silicon nanotubes based on the most stable structures of empty Si_{12} clusters as well as the effect of hydrogen termination and different transitional metal atom doping.

Out of many possible orientations to form cluster assembly using these four units as building blocks separately, we choose few most stable orientations that can form finite cluster assembly and infinite nanotubes. To investigate the hydrogen termination effect on the finite nanotube or cluster assembly made of hexagonal prism Si_{12} structure forms

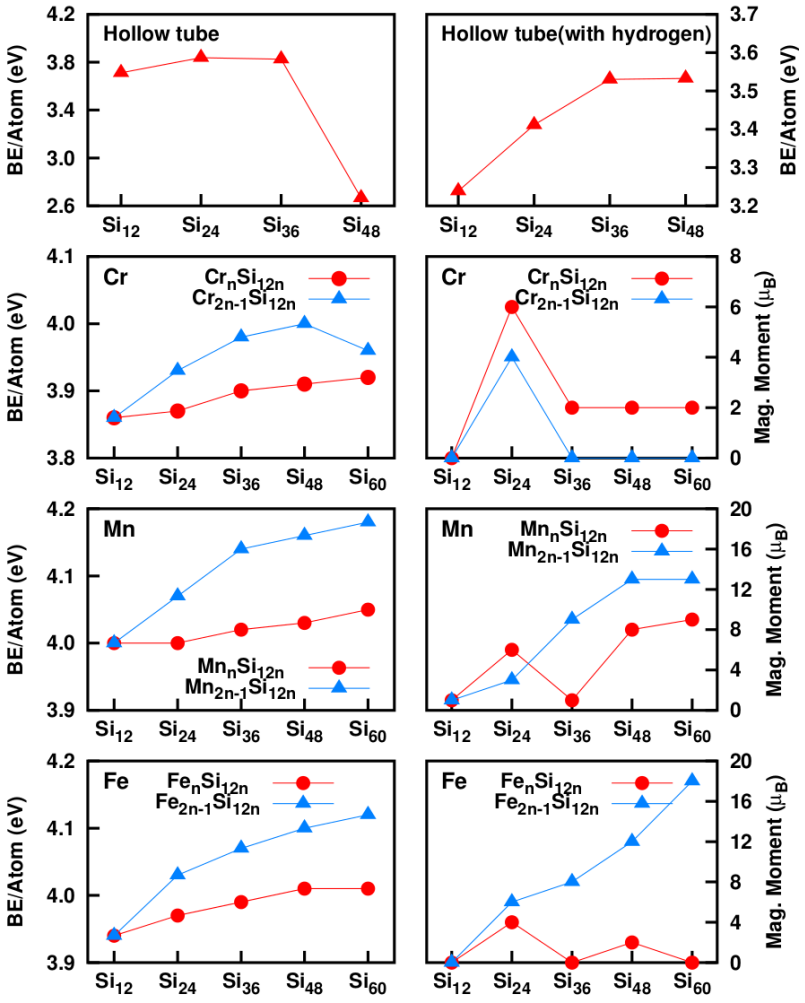

Figure 6.2: Variation of average binding energy and corresponding magnetic moment of different TM doped Type 1 and Type 2 nanotubes.

1-D finite nanotube (Fig. 6.1), we calculate the variation of average binding energy (BE) and is shown in (Fig. 6.2). We forms two different types of cluster assemblies based on the density of TM atom doping using Si_{12} as base unit with chemical compositions $(CrSi_{12n})_n$ and $Cr_{2n-1}Si_{12n}$.

The average binding energy of the empty clusters are almost constant (3.8 eV) with a small variation up to the size with n=36. Then suddenly it drops to 2.6 eV at n=48 size. This indicates the thermodynamical instability of the clusters. However, after hydrogen termination, the BE increases and then stabilize at n=36 with a value of 3.52 eV. Therefore, hydrogen termination is actually converting the finite sized assembly to a section of infinite nanotube like structure with thermodynamical stability.

The effect of hydrogen termination is similar in the finite nanotubes or cluster assemblies made of Si_{16} as base unit, and also in other bigger sized clusters useful to

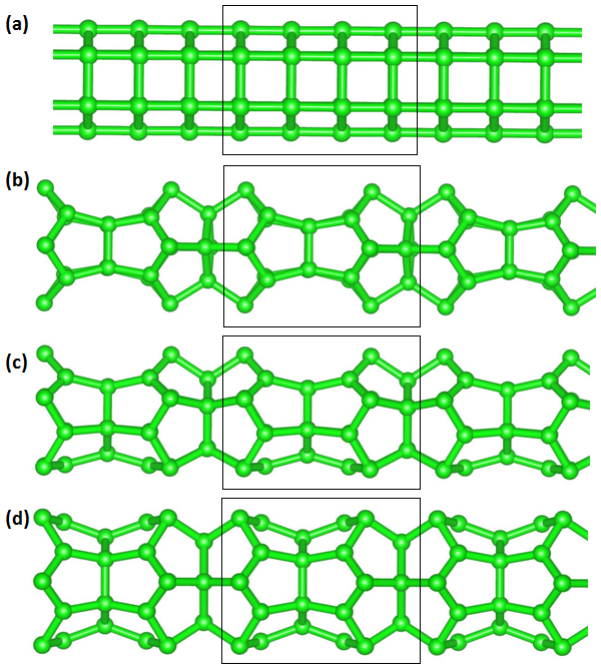

Figure 6.3: Type 1 to Type 4 hollow nanotubes modeled by (a) Si_{24}, (b) Si_{24}, (c) Si_{30} and (d) Si_{36} units respectively as building blocks. The region enclosed by black rectangular block represents the unit cell to form infinite empty nanotube.

design nanotubes. The lesser possibility of formation of finite nanotubes using the units Si_{24} (Type 1), Si_{24}(Type 2), Si_{30} (Type 3)and Si_{36}(Type 4) as base units is also due to the atomic influences of a particular cell on the next cell. In the case of clusters (finite nanotubes) the separation between the base units is selected on the basis of non-interacting system, as if, they are in gaseous phase, where, the two periodic images are separated by 12-13 Å whereas, the cells, where the clusters are encapsulated, are connected. Under this condition, clusters are free from the interaction of the neighboring clusters or from the interacting force produced by the periodic images. For small sized clusters, the cell size is taken as $20\times20\times20$ $(Å)^3$. However, it is also a function of the cluster size. It is worth to mention here that we increase the cell size when the cluster size is relatively bigger and the criteria of the minimum separations are not achieved. We generally use cubic cell to explain the clusters. But if the building block (that may formed by using a number of small clusters to make cluster assemblies) size is long enough in one direction (in case of nanotubes), then we change the shape of the cell from cubic to cuboid. Usually, we do not disturb the cell volume and shape, means; we apply constraints on the cells during a particular type of calculation. The optimized empty or hollow nanotube structures with chemical compositions:$(Si_{24})_n$:Type 1; $(Si_{24})_n$: Type 2; $(Si_{30})_n$: Type 3 and $(Si_{36})_n$: Type 4 are shown in Fig. 6.3. As

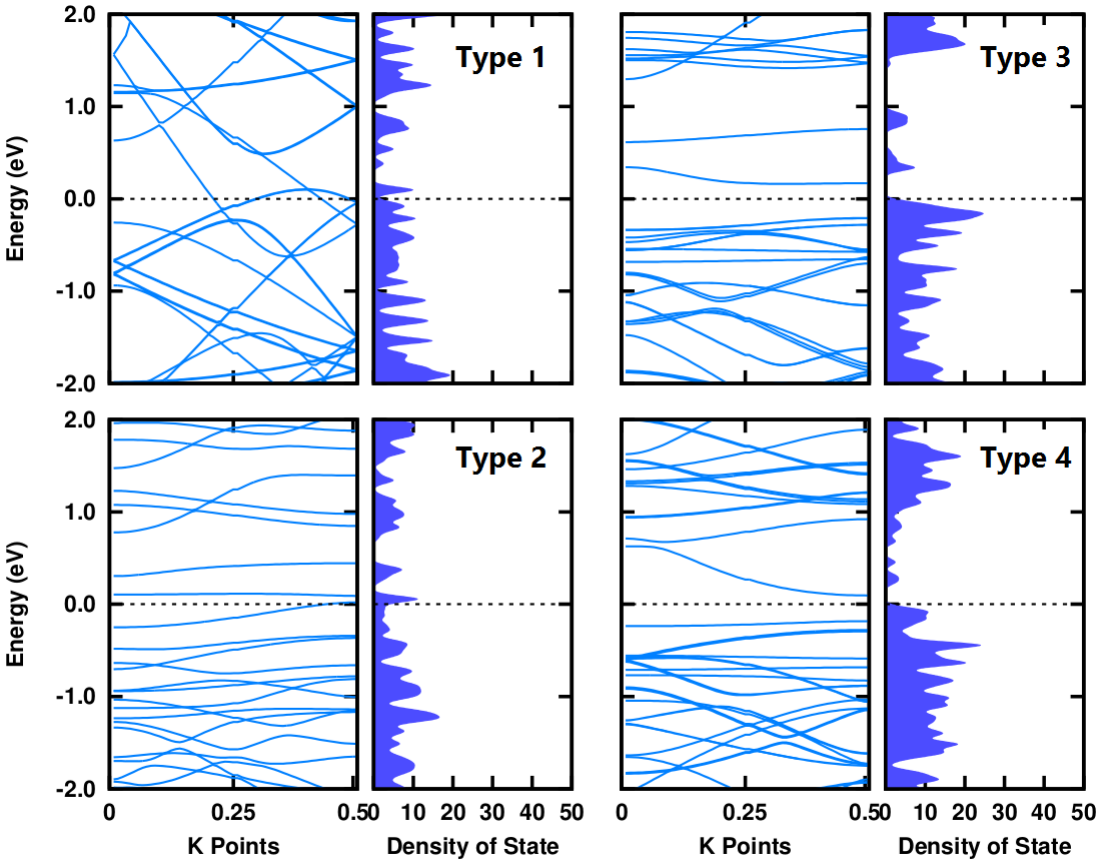

Figure 6.4: Band structure and DOS of hollow silicon nanotubes: (a) Type 1, (b) Type 2, (c) Type 3 and (d) Type 4. Dotted line shows the position of Fermi levels.

per the structural symmetry of the finite nanotubes without hydrogen termination are concerned, Si_{12} based structure is more symmetrical than nanotube made of Si_{16} cluster in pure (or empty) nanotubes(Fig. 6.3). To check the properties of these four types (Type 1 to Type 4) of hollow nanotubes, we calculate their band structures and density of states(DOS) and the results are shown in Fig. 6.4. Both in Type 1 and in Type 2 nanotubes, there are clear contributions of bands surrounding the Fermi energy level as well as on the Fermi level. Therefore,both the nanotubes are characterize as metallic in nature. Sometimes the bands are very similar to flat bands in bulk materials. The flatness of the spin-polarized bands in Si_{16} based hollow nanotube indicates that the electronic states are heavily localized. In the relatively bigger cross-sectional hollow nanotubes, (Type 3 and Type 4) the band structures and DOS both are different from Type 1 and Type 2 nanotubes. In Type 3 and Type 4 nanotubes, the bands touches the Fermi level, with a clear band gap of 0.38 eV and 0.29 eV respectively. In Type 4 nanotube, there is flat band just below the Fermi level with a dispersive nature of the

first valance band along Γ-K axis. Hence,the Type 3 and 4 nanotubes could be taken as semi-metallic in nature. Overall, the increase of the size of the unit cells, the hollow nanotubes, change from metallic nature to semi-metallic nature in the present study. It is worth to mention here that in previously reported work hollow Si nanotube with zig-zag, arm-chair and chiral structures, show semiconductor nature [165].

6.3.2 TM doped Type 1 to Type 4 finite nanotube like cluster assemblies

The structures of the two types of TM doped Type 1 finite nanotubes are based on the optimized $TMSi_{12}$hexagonal prism structure with D6h symmetry. Other possible structures are anti-prism structure, bi-capped pentagonal prism and fullerene structures. But in the assembled clusters we find $TMSi_{12}$ prism structure is only useful geometry to form stable $(TMSi_{12})_n$ and $(TM_{2n-1}Si_{12n})$ cluster assemblies.

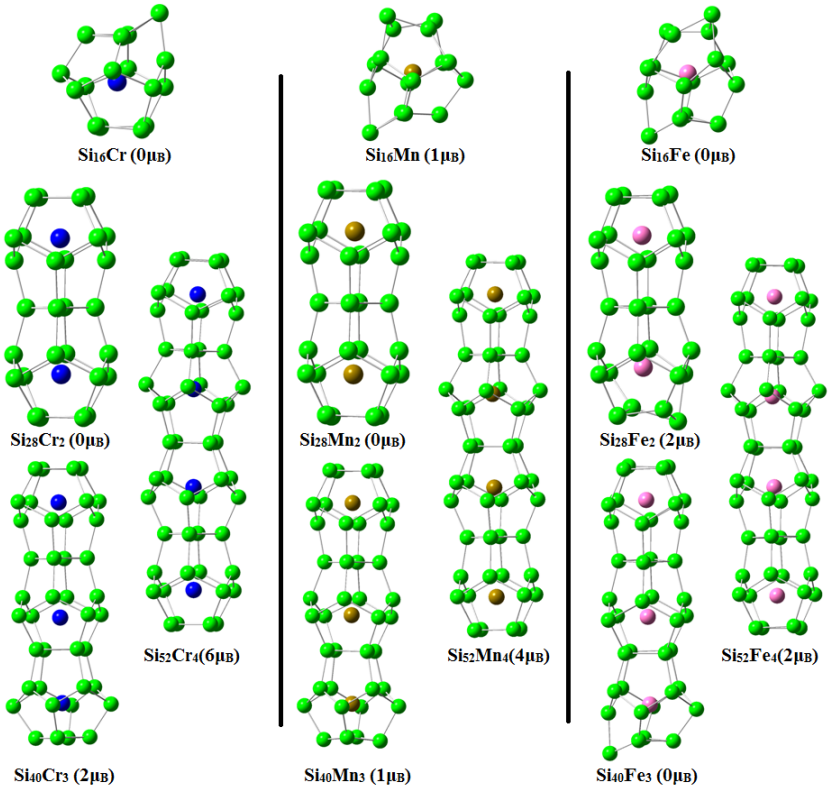

Figure 6.5: Structures of finite silicon nanotubes TM doped Si_{16} (type 2) clusters and the building blocks

Hence, it is fit for finite and infinite nanotubes. After confirming the stability of the above structures we start to stack $TMSi_{12}$ units along the hexagonal cross-sectional

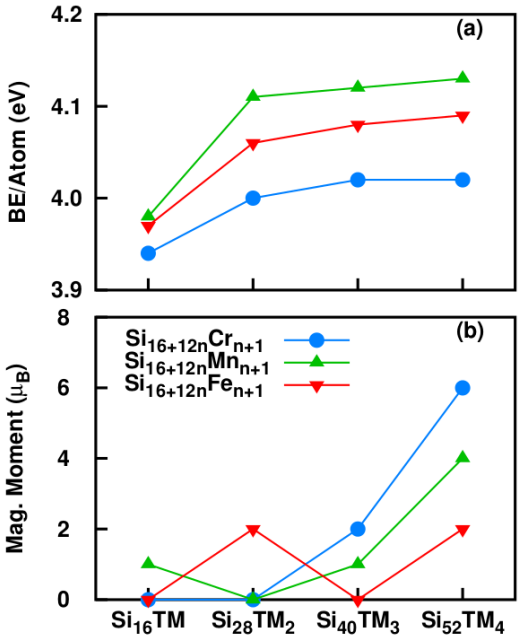

Figure 6.6: Variation of average binding energy and corresponding magnetic moment of different TM doped Type 2 Si nanotubes.

side of the cluster in two different ways (as shown in each of the section in Fig. 6.1) to form $(TMSi_{12})_n$and $TM_{2n-1}Si_{12n}$, where the number density of transition metals are different. As a result, the average binding energy in the 2^{nd} case leads to an increase and it helps to improve the geometry from slightly distorted planner cross-section in hollow cluster assembled system to nearly planner nanotube hexagonal cross-section (Fig. 6.2). It is clearly seen that the average BE of $TM_{2n-1}Si_{12n}$ is reasonably higher as compare to the BE of $TM_{2n-1}Si_{12n}$ (where, TM=Cr, Mn, Fe) for all transition metal doping. Interestingly, the magnetic moment of TM doped assembly show different behavior in different sizes and types, as well as it depends on the doped atoms. In Cr doped assemblies, the magnetic moment quench quickly in both in Cr_nSi_{12n} and $Cr_{2n-1}Si_{12n}$at n=1(Fig. 6.2). It increases for higher 'n' in Cr_nSi_{12n}, whereas, in $Cr_{2n-1}Si_{12n}$, the magnetic moment quenched again for n=3 and 4. For Fe and Mn doped $TM_{2n-1}Si_{12n}$ assembly the magnetic moment increases with the size of the clusters. In $TM_{2n-1}Si_{12n}$, this variation does not follow any systematic trend (Fig. 6.2). There is quenching of Mn magnetic moment at n=3 and then again it increases at the higher sizes. In Fe doped $Fe_{2n-1}Si_{12n}$ finite nanotubes, the magnetic moment variation shows unstable pattern within the size range of the finite nanotube from n=1 to 4. The variation of magnetic moments in the TM doped finite nanotube like clusters assemblies could be due to the

presence of different unsaturated interactions, which varies with the size of the cluster assembly and also as a function of number of doped transition metal atoms. Details of the magnetic moments are given in Table 6.1.

Geometry optimization shows a number of different low energy isomers in $TMSi_{16}$ composition. Among these we find that the fullerene kind of structure, which is combination of two rhombi and eight pentagonal closed loops Si rings is suitable for making cluster assembly or finite nanotube. Following the work reported by Palaria et al.[164]. We have studied the hollow nanotube of the similar kinds. To form finite Type 2 nanotube structure we added the units of $TMSi_{12}$(which is the part of $TMSi_{16}$) with the optimized $TMSi_{16}$ (TM=Cr, Mn and Fe) isomer(Fig. 6.5). The magnetic moment and average binding energy variation is presented in Fig. 6.6.

Average binding energy variations are clearly indicating that addition of each $TMSi_{12}$ unit is increasing the stability of the clusters, which is an indication of the formation of infinite nanotubes. It is worth to mention that when the cluster assembly contains even number of transitional metal atoms, the magnetic moment of the finite nanotubes drops compare to the clusters made of odd number of transition metal atoms. Similar to TM doped Type 1 and Type 2, cluster assembly, we also attempt to form TM doped Type 3 and Type 4 cluster assemblies. But we did not find any optimized structure, which could be taken as the initial stage of Type 3 or Type 4 nanotube. However, after hydrogen termination, the optimized assemblies form Type 3 and Type 4 finite nanotubes(Fig. 6.7). Corresponding variation in binding energies are shown in the Fig. 6.8. We have applied hydrogen termination to the Type 1 and Type 2 finite nanotubes also. After optimization we found more symmetric structures compare to Type 1 to Type 4 finite nanotubes with finite amount of magnetic moments and high value of binding energies for all TM doping (Fig. 6.7 and Fig. 6.8). This gives an indication of possible formation of infinite nanotube with finite magnetic moments.

6.3.3 Doped Si-nanotubes: Type-1$(TM_4Si_{24})_n$, Type-2 $(TM_2Si_{24})_n$, Type-3 $(TM_2Si_{30})_n$ and Type-4 $(TM_2Si_{36})_n$

Transition metal doped Type 1 nanotubes and corresponding band structures as well as DOS are shown in Figs. 6.9 and 6.10 respectively. The calculated magnetic moments per

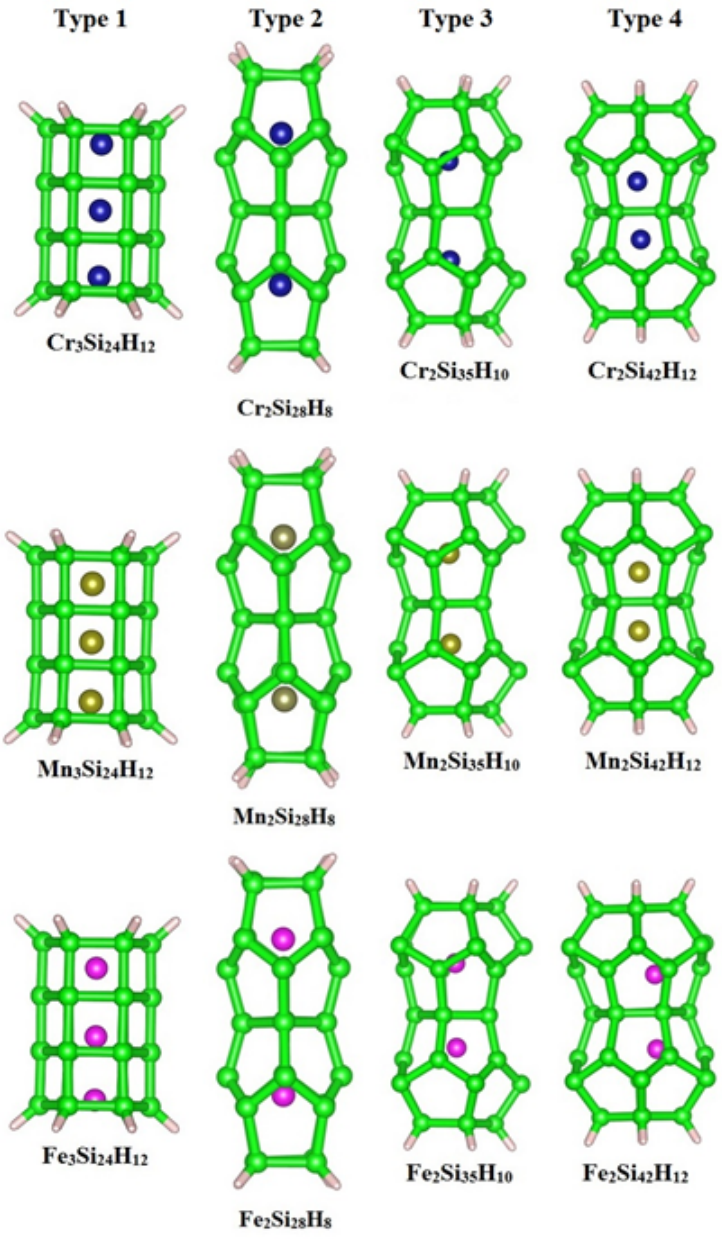

Figure 6.7: Structures of doped Type 1 to Type 4 finite TMSiNTs with hydrogen termination

unit cell of Cr, Mn and Fe doped nanotubes are 1.36 μ_B, 8.0 μ_B and 8.02 μ_B respectively. The density of states in spin-up and spin-down Cr doped nanotube are comparable.

There is a small change in band shift towards the upward direction in spin-down band structure compare to the spin-up state. Both in spin-up and spin-down band structures, there is considerable amount of band crossing over the Fermi energy level. In DOS also clear contribution of states on the Fermi level indicates the metallic nature of this nanotube. Comparing the band structure of hollow nanotube of similar kinds, it can be seen that the bands in the doped nanotubes are much more denser and it also

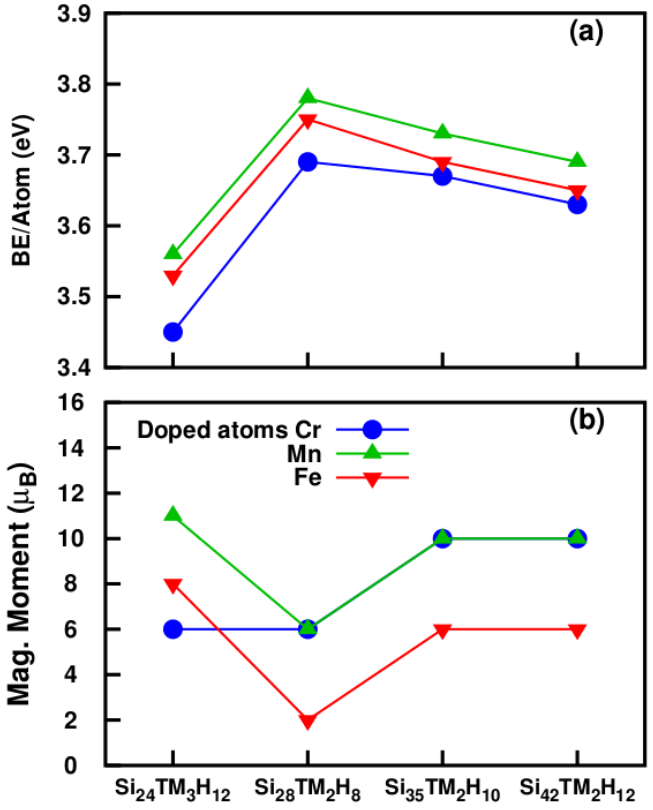

Figure 6.8: Variation of average binding energy and corresponding magnetic moment of different TM doped Type 1 to Type 4 nanotubes with hydrogen termination.

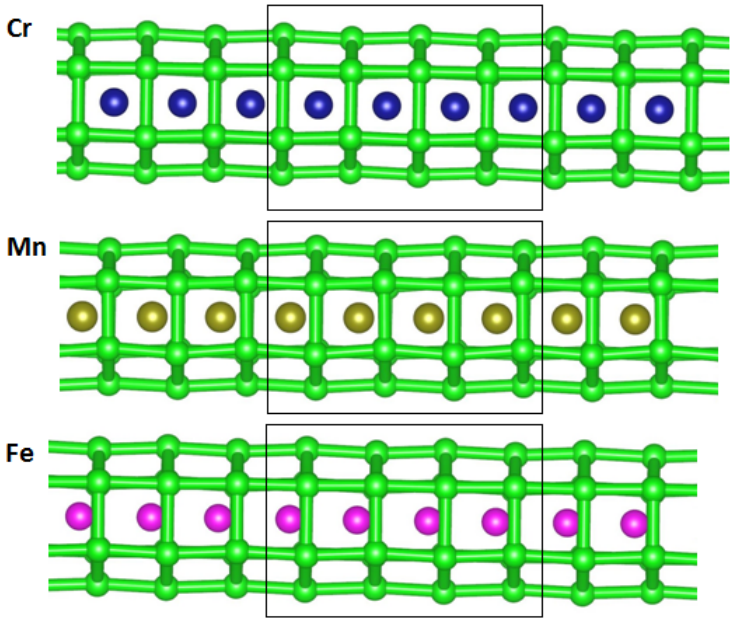

Figure 6.9: Transition metal (TM=Cr, Mn, Fe)doped Type 1 silicon nanotubes. Green, brown, blue and pink spheres are representing Si, Mn, Cr and Fe respectively.The region enclosed by black rectangular block represents the unit cell to form infinite empty nanotube.

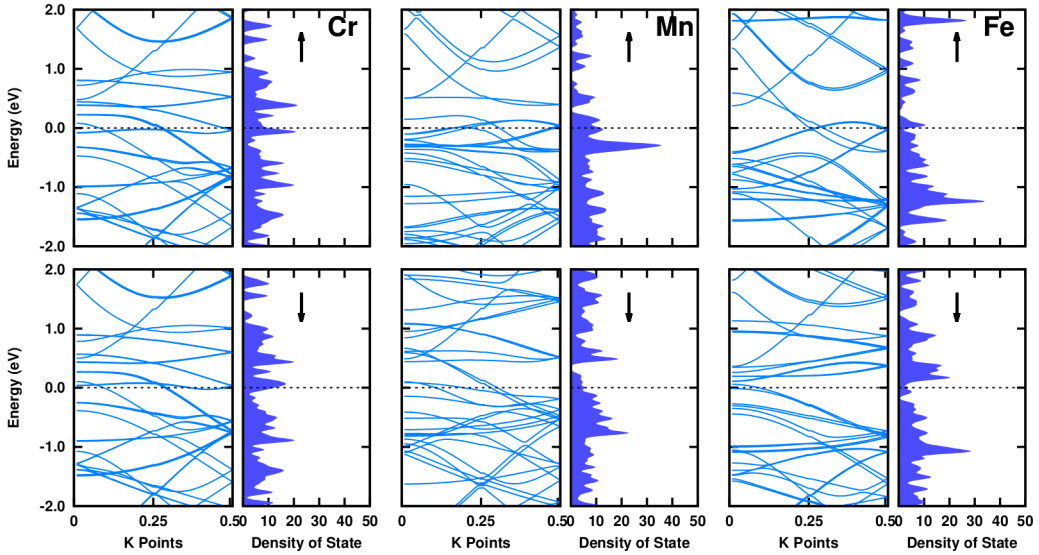

Figure 6.10: Band structure and density of state of transition metal (TM=Cr, Mn and Fe) doped Type 1 silicon nanotubes. Upper one and lower one are denoting spin up and spin down states, respectively. Dotted line shows the position of Fermi level.

reflects in density of states (DOS) plot. In all TM doped nanotubes of this particular structure, the projected density of states (PDOS) show that most of the contribution in DOS below Fermi energy level is due to d- states of the doped transition metal atom and overall there is contribution from Si p-states, which are relatively small. The band structure of spin-up and spin-down states in Mn and Fe doped nanotubes are different in nature.

In both compositions, DOS near Fermi level in spin-down states is relatively higher than the spin-up state. This shows metallic behavior of the spin down state with a band crossing at the Fermi level in spin-down components, indicate metallic behavior of the nanotubes. The band structure of the Mn-doped ferromagnetic nanotube shows a gap above the Fermi energy in spin-up component. In previous report it was found that the majority of states for Mn lie well below the Fermi energy and the Si 3p states contribute mostly to the states near the Fermi level which also could be the cause of magnetic moment fluctuations (from 1.66 μ_B to 2 μ_B)[163]. In the present Mn doped Type 1 nanotube, the anti-ferromagnetic configuration is only 0.09 eV lower in energy than the corresponding ferromagnetic configuration. Therefore, the transformation from anti-ferromagnetic to ferromagnetic coupling could be achievable by application of a weak magnetic field. This suggests the possibility of spin-polarized current controlling via application of small magnetic field.

In Fe-doped nanotube, the interaction between Fe-Fe is ferromagnetic in nature with

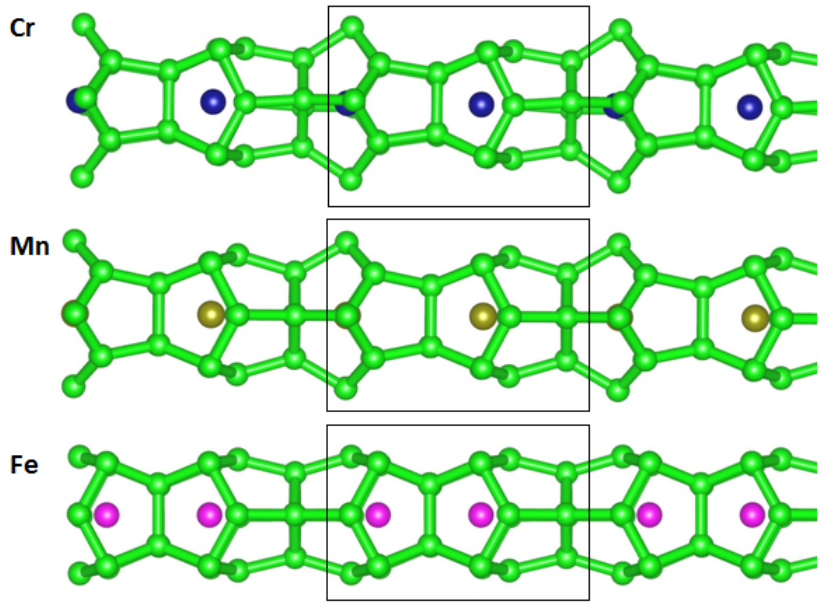

Figure 6.11: Transition metal (TM = Cr, Mn and Fe)doped Type 2 silicon nanotubes. Green, brown, blue and pink spheres are representing Si, Mn, Cr and Fe respectively. The region enclosed by black rectangular block represents the unit cell to form infinite empty nanotube.

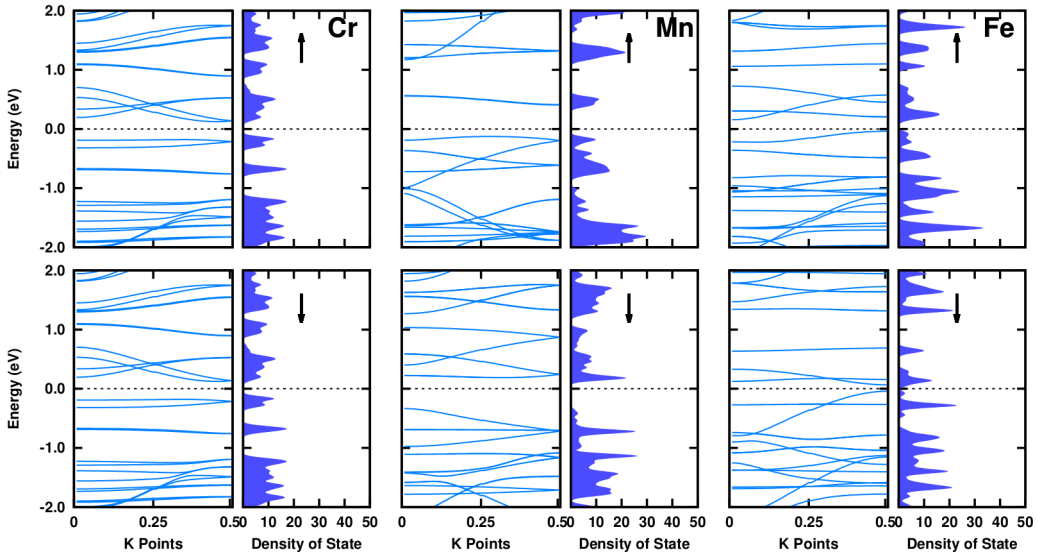

Figure 6.12: Transition metal (TM = Cr, Mn and Fe)doped Type 2 silicon nanotubes. Green, brown, blue and pink spheres are representing Si, Mn, Cr and Fe respectively. The region enclosed by black rectangular block represents the unit cell to form infinite empty nanotube.

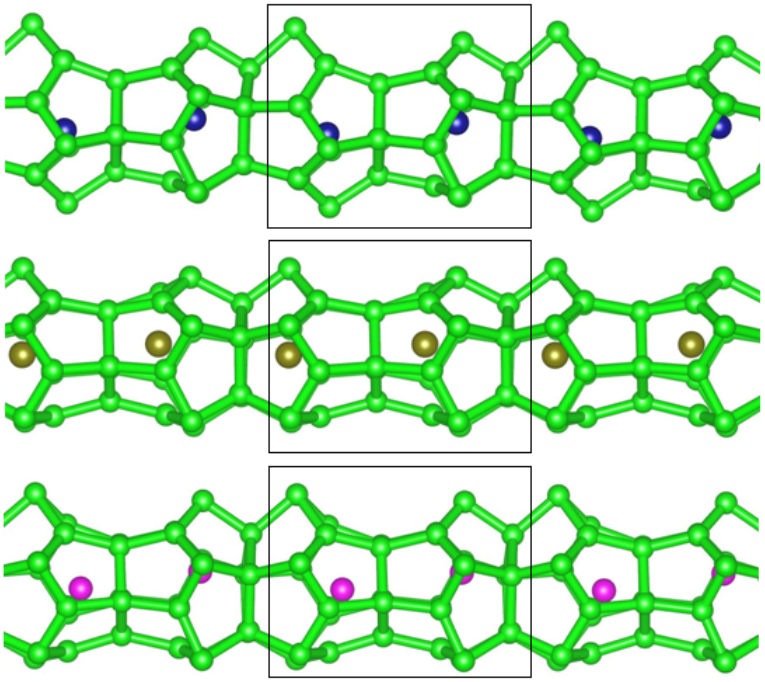

Figure 6.13: Transition metal doped (TM=Cr, Mn and Fe) Type 3 silicon nanotubes. Green, brown, blue and pink spheres are representing Si, Mn, Cr and Fe respectively. The region enclosed by black rectangular block represents the unit cell to form infinite empty nanotube.

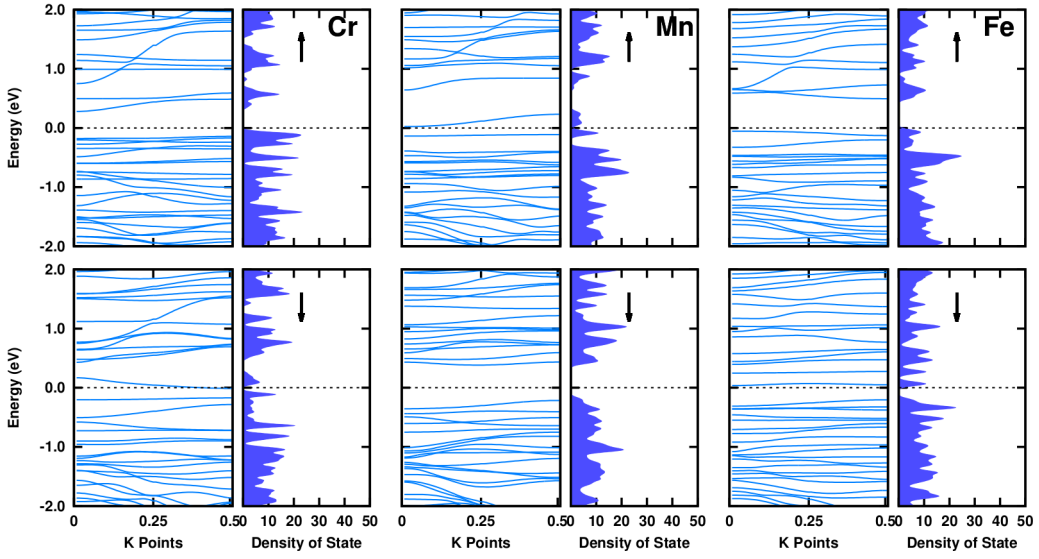

Figure 6.14: Band structure and density of state of transition metal (TM = Cr, Mn and Fe)doped Type 3 silicon nanotubes. Upper one and lower one are denoting spin up and spin down states, respectively. Dotted line shows the position of Fermi level.

a high magnetic moment of 2.1 μ_B per Fe atomic site, which is nearly the same as the Fe atomic magnetic moment in bulk iron. It is important to mention here that Fe- doped silicon nanotubes with pentagonal and hexagonal cross-sectional structures exhibits metallic behavior both in finite and infinite structures[166]. The visible one-dimensionality of this nanotube along with its high moment makes it attractive as a nanoscale magnet. Optimized structure of Type 2 nanotube is shown in Fig. 6.11. This nanotube is based on the ground state unit of $TMSi_{16}$ optimized clusters. Corresponding band structure and DOS is shown in Fig. 6.12. In some of the spin-up or in spin-down state of Type 2 nanotube, the band structure below fermi energy level is almost flat as like in hollow Type 2 nanotube for different doping. This indicates the presence of localized electronic state and hence the localized magnetic moment at the substitution site of Si[167]. In our study we did not find any band crossing the Fermi level but the gap between occupied and unoccupied bands are very low (0.08 eV to 0.1 eV) with considerable amount of DOS contributions around Fermi level both in spin-up and down states. The band structure and DOS imply the nanotube is similar to semi-metallic materials in nature as there is higher DOS in spin-up state compare to its spin-down state. Hence, due to doping of Cr and Fe, the Type 2 empty nanotube with metallic character changes to semi-metallic in nature with redistributions of the bands.

The band structure and DOS of Mn doped Type 2 nanotube are different from the Cr and Fe doping. Doping of Fe gives more structural symmetry compare to Cr and Mn because of different electronic configurations and therefore, configuration interactions between the doped elements and with the nanotube. In both the spin states there is clear band gap with is different nature in band structure, which assigned this nanotube as semiconductor in nature. Since the band structures and DOS are different in different transition metal doping, therefore, the variation in conduction and transport properties are also expected to be different. Now, moving to the nanotubes made of bigger units $(TM_2Si_{30})_n$ (Type 3) and $(TM_2Si_{36})_n$ (Type 4), the band structure and DOS are find different from Type 1 and Type 2 nanotubes.

The optimized structure and corresponding DOS/band structures of Type 3 nanotube are shown Figs. 6.13 and 6.14. In this nanotubes, spin up and spin down states are different in all transition metal doping. The nature of band structure and DOS in Cr and Fe doped nanotubes are quite similar around the Fermi level, whereas, this is different in Mn doped nanotube with a relatively larger gap in spin down state and a clear contribution of DOS on Fermi level. For Cr and Fe doping, the spin down

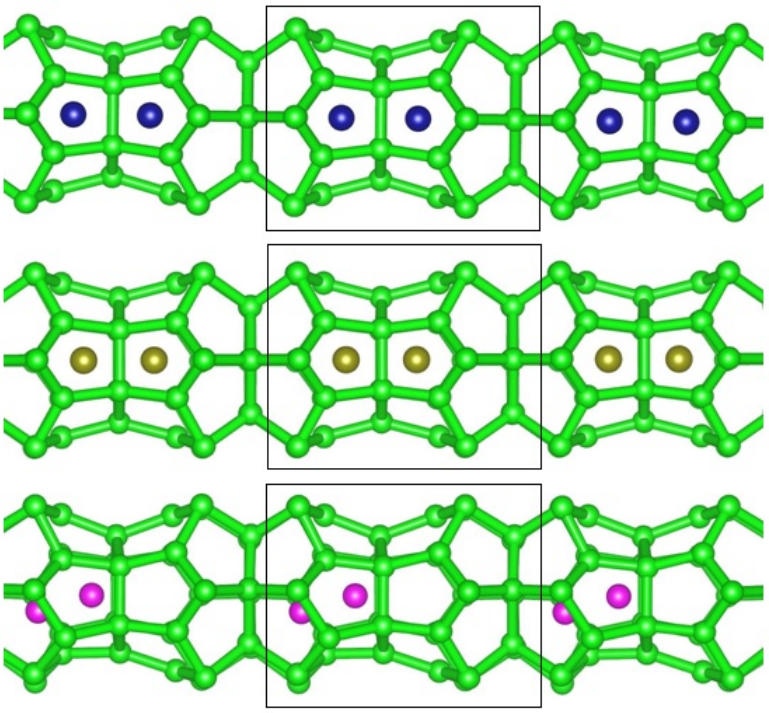

Figure 6.15: Transition metal doped (TM = Cr, Mn and Fe) Type 4 silicon nanotubes. Green, brown, blue and pink spheres are representing Si, Mn, Cr and Fe respectively. The region enclosed by black rectangular block represents the unit cell to form infinite empty nanotube.

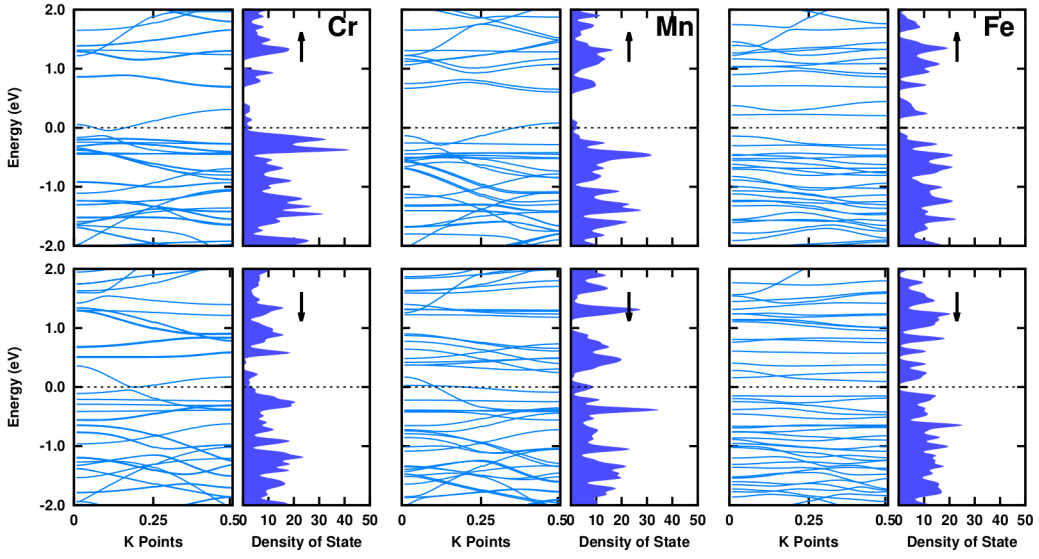

Figure 6.16: Band structure and density of state for transition metal (TM = Cr, Mn and Fe)doped Type 4 silicon nanotubes. Upper one and lower one are denoting spin up and spin down states respectively. Dotted line shows the position of Fermi level.

Table 6.1: Magnetic moment variation of both (Type 1 and Type 2) the TM doped SiNT's with the number of cluster units (n) and m_{TM} is the number of dopant TM atoms.

Type 1	Magnetic moments (in μ_B) for different cluster units (n)			
Doping	n=1	n=2	n=3	n=4
	m_{TM}=1	m_{TM}=3	m_{TM}=5	m_{TM}=7
Cr	0	4	0	0
Mn	1	3	9	13
Fe	0	6	8	12
Type 2	Magnetic moments (in μ_B) for different units (n)			
Cr	0	0	2	6
Mn	1	0	1	4
Fe	0	2	0	2

and spin up band structures are metallic in nature. The LUMO of the spin up states are approximately 0.4 eV and 0.5 eV above than the Fermi level for Cr and Fe doping respectively. Therefore, the Cr and Fe doped Type 3 nanotube can take as half-metallic in nature. When the Type 3 hollow nanotube doped with Cr and Fe, the bands structure and DOS changes with a wide gap in the spin-up state as in half-metallic system. Due to Mn doping, density of states in spin-up state below Fermi energy level drastically decreases compare to Cr doping with the presence of DOS on Fermi level and with a wider band gap in spin down state. Effectively the lower DOS in spin down state can decrease the transport and conduction properties. Complete band structure and DOS picture of Type 3 nanotube doped with Cr, Mn and Fe assigned their character as half-metallic in nature. It is to be noted that, in Type 3 nanotube, the doped transition metal atoms are not in a line inside the nanotube. The distortions are different in different TM doping. This is the direct evidence of the size effect of the transition metal atom doping in Type 3 nanotube. The size effect can be seen clearly in Type 4 nanotube where Cr and Mn atoms are in a straight line inside the nanotube, whereas, Fe is distorted (Fig. 6.15).

To optimize the nanotube doped with Fe atom (relatively smaller size compare to Cr and Mn), the Fe atoms shift from the axis of the nanotube. With reference to the band structure and DOS of Cr, Mnand Fe doped Type 4 nanotube; we assign them as metallic, half-metallic and semi-metallic respectively in character (Fig. 6.16). Therefore, with the variation of the size of the nanotube and transition metal doping, the conducting behavior of the nanotube varies from one regime to other as reported by others[168,169].

Table 6.2: Magnetic moments of the cluster assembly and TM doped SiNT's (TM = Cr, Mn, Fe).

Cluster Assembly	Magnetic moments for Doping (in μ_B)		
	Cr	Mn	Fe
Type 1 (TM_3Si_{24})	4.00	3.00	6.00
Type 2 ($TM_2Si_{28}H_8$)	6.00	6.00	2.00
Type 3 ($TM_2Si_{35}H_{10}$)	10.00	10.00	6.00
Type 4 ($TM_2Si_{42}H_{12}$)	10.00	10.00	6.00

Table 6.3: Characteristics and magnetic moment of one unit cell of different types of nanotubes

Type	TM-Doping		
	Cr	Mn	Fe
Type1 $(TM_4Si_{24})_n$	Metallic ($1.36\mu_B$)	Metallic ($8\mu_B$)	Metallic ($8.02\mu_B$)
Type2 $(TM_2Si_{24})_n$	Semi-metallic ($0\mu_B$)	Semiconductor ($6\mu_B$)	Semi-metallic ($2\mu_B$)
Type3 $(TM_2Si_{30})_n$	Half-metallic ($8\mu_B$)	Half-metallic ($8\mu_B$)	Half-metallic ($6\mu_B$)
Type4 $(TM_2Si_{36})_n$	Metallic ($10\mu_B$)	Half-metallic ($9.33\mu_B$)	Semi-metallic ($4\mu_B$)

Hence, same nanotube can be used as metallic, semi-metallic and half-metallic with different magnetic behavior by proper choice of transition metal doping with a wide range of applications as conductive wires[170,171] energy storage and energy conversion devices[172,173], flat panel displays[174] and radiation sources[175] as well as probes[176] (such as an STM and AFM tip) and chemical sensors[177]. This can enhanced its application part and can be used as a tunable magnetic material in the industries.

6.4 Conclusions

The present study reports the modeling of four different types of empty and transition metal (TM = Cr, Mn, Fe) doped nanotubes. We examine the stability of these nanotubes and then the variation of band structures, DOS, magnetic properties with the variation of TM doping in the empty nanotubes. The overall results can be summarize as follows:

- It is found that the specific size and structure of the nanocluster and cluster assemblies can be used to generate empty as well as transition metal doped stable nanotubes. Sometimes these cluster assemblies does not show the stability, but the proper choice of the assembly can form stable nanotubes.

- Out of four hollow nanotubes (Type 1 to Type 4), Type 1 and 2 show metallic characteristics with clear band contributions on the Fermi level. However, the nanotubes with relatively bigger cross-sectional area (Type 3 and 4) show semiconductor characteristics with band gap of 0.39 eV and 0.28 eV respectively. The flat bands in Type 2 nanotube shows its nature similar to that in bulk materials. The flatness of the spin-polarized bands indicates that in Si_{16} based hollow nanotube the electronic states are heavily localized and such metallic character caused by these bands is highly stable to any perturbation.

- The TM doping does not affect the band structure and DOS in Type 1 nanotube and hence it is metallic in character for all doping. In addition, the transition metal (TM=Cr, Fe and Mn) doping added finite magnetic moments of amount 1.35 μ_B, 8.02 μ_B and 8.0 μ_B respectively to the Type 1 nanotube. Whereas, the same doping reduces the magnetic moments to 0.0 μ_B, 2.0 μ_B and 6.0 μ_B respectively in Type 2 nanotube. This indicates the strong interaction between the transition metal atoms with Type 2 nanotube. Hence, the Cr doped Type 2 nanotube is non-magnetic metallic species in nature. However, the same doping increases the magnetic moments of the nanotubes in Type 3 and Type 4 as shown in Table 6.2.

- We found that the Mn doped Type 1 nanotube; the anti-ferromagnetic configuration is only 0.09 eV lower in energy than the corresponding ferromagnetic configuration. Therefore, the transformation from anti-ferromagnetic to ferromagnetic coupling may be achieved by application of low magnetic field, suggesting that spin-polarized current flow could be controlled through application of a magnetic field.

- The characteristic of different nanotubes after doping by transition metals is given in Table 6.3. Based on this results, we can conclude that the combination of the type of nanotube (Type 1 to Type 4) and the proper choice of doping, can vary the characteristic of the nanotubes to metallic, semi-metallic, half-metallic and semiconductor in nature with wide range of applications[168–177]. These tunable magnetic materials are useful in the industries. Since the transition metal doping changes the property of the nanotube, therefore the variation in conduction and transport properties are also expected to be different.

Chapter 7

Conclusions and future scope

7.1 Conclusions

The present thesis systematically assesses the feasibility of using transition metal (TM) doped silicon and germanium clusters to design novel functionalized cluster-assembled materials using density functional theory. In Chapter 1, a concise introduction to the various employed methodologies, concepts to explore the configurational space and description of the electronic structure and properties of doped silicon and germanium clusters is discussed. In Chapter 2, we have discussed the methodology in used in our studies. From Chapter 3 to Chapter 5, a thorough analysis of the nature of chemical bonding within exohedrally and endohedrally TM doped Ge_n (TM = Ni, Cr, Mo, Au) clusters, have been done. The stability of such clusters have been explained from the study of variation of energetics and the chemical bonding between dopant and host atoms. We have found that the shell closure number plays an important role in the structural stabilization. This further explains the adaptive capability of the TM-Ge bonding, which is more as a result of a complex hybridization than the originally proposed mere formal charge transfer. Other additional reason for the stabalization of these clusters is the localization of the electrons which can be theoretically measured by nuclear independent chemical shift (NICS) values. In Chapter 6, we have studied the building blocks of small sized TM doped Si_n clusters (TM = Cr, Mn, Fe). It is worst mention here that we found few tunable magnetic species whose

structural properties can be manipulated by changing the structural orientation and concentration of the atoms.

7.2 Future Scope

In our studies, we have chosen few cluster systems. There are many other systems and possibilities that can be investigated and analyzed. Few of them have been mentioned below.

7.2.1 Catalytic properties of TM doped Si/Ge clusters

Investigation of catalytic properties of TM doped Si/Ge clusters could be interesting. While catalysis is an active technological application of transition metal related nanoparticles, there are relatively few theoretical studies attempted to understand how transition metal atom act as a catalyst in chemical reaction. Catalytic reactions can be considered by studying the energy-barrier of reaction paths therefore finding the most favorable reaction path. As in our studies, we have examined that the dopant atom is not just acting like a dopant atom but the also controlling all over properties. It seems that the electronic distribution of dopant TM atom/atoms are spread over the surface of Si/Ge clusters. In Chapter 5, we have studied Au doped doped Ge_n clusters, where Au is playing a role of bridging atom in between the 2 separate Ge_n cluster species. Au is working as catalyst, so it is interesting to study its modified properties in the germanium or silicon clusters. Treating this problem may sound easy, but comparing to the number of configurations of reactants and products is a challenging job.

7.2.2 Legend protected clusters

Small sized cluster's properties are sensitive with size and compositions. Legend protection is a process to preserve the clusters properties to use it as an industrial material. There are various clusters those exhibit unique properties but due to the less stability of the clusters it is difficult to store these properties. Organic molecules are known best to add on non-organic cluster's surface. Heaven et al.[178] investigated the crystal structure of the thiolate protected gold

nanoparticle $[N(C_8H_{17})_4][Au_{25}(SCH_2CH_2Ph)_{18}]$. Recently, Chauhan et al.[179] modeled $Ni_9Te_6(PEt_3)_8C_{60}$ a legend protected cluster. The PEt_3 ligands are shown to create an internal coulomb well that lifts the quantum states of the Ni_9Te_6 cluster lowering its ionization potential to 3.39 eV thus creating a super-alkali motif.

7.2.3 Functionalized cluster assembled materials

As we studied in Chapter 5 and Chapter 6, assembling clusters is the best way to design or model designer new materials. There are other possibilities that can be explored by forming different cluster assemblies to model 1D, 2D and 3D materials. There are few theoretical attempts[1,70–73] to make such assemblies by the "bottom up" approach. Recently, Liu et al.[180] have reported such functionalized material on In_nAs_n system. They have investigated a new family of $In_{12}As_{12}$ cluster-assembled materials using a bottom-up approach together with DFT calculation. There are several possibilities in this direction to create new materials.

7.2.4 Multi TM atoms doped Si/Ge nanoclusters

The possibility of multi-doping in Si and Ge clusters in order to achieve high spin states beyond the single-dopant atom which has been reported as a potential future candidate. It also can be explored further on conserving both the structural integrity of the host cage and the high spin state of the guest dimer dopant which can thereby increase the magnetic moment. Moreover, the possibility of increasing the cluster spin state further by encapsulating various number of dopant atoms into a suitably sized Si/Ge cage could be quite interesting. Such multiple doping phenomena could also be used in functionalized assembled materials. These developments indicate many potential future applications beyond the specific problems of single doped semiconductor clusters.

7.2.5 Other possibilities

Application of shell closer number following the Hund's rule can be an interesting parameter to examine in TM doped semiconductor clusters. Sometimes, molecular

orbital magic numbers may not be able to explain the clusters stabilities. In our chapter 5, few $AuGe_n^-$ clusters holds the molecular electrons which is equal to the magic numbers but the distribution of orbitals are quite different and disagree with the shell closer phenomena. So it is a challenging problem on Si/Ge based clusters to co-relate the shell closing model and orbital distributions. In the present thesis, we need more focus to understand this problem.

Bibliography

[1] S. A. Claridge, A. Castleman Jr, S. N. Khanna, C. B. Murray, A. Sen, and P. S. Weiss, Acs Nano **3**, 244 (2009).

[2] W. A. De Heer, Reviews of Modern Physics **65**, 611 (1993).

[3] V. M. Medel, J. U. Reveles, S. N. Khanna, V. Chauhan, P. Sen, and A. W. Castleman, Proceedings of the National Academy of Sciences **108**, 10062 (2011).

[4] W.-D. Knight, K. Clemenger, W. A. de Heer, W. A. Saunders, M. Chou, and M. L. Cohen, Physical review letters **52**, 2141 (1984).

[5] K. Clemenger, Physical Review B **32**, 1359 (1985).

[6] M. Brack, Reviews of modern physics **65**, 677 (1993).

[7] M. Chou, A. Cleland, and M. L. Cohen, Solid state communications **52**, 645 (1984).

[8] W. Ekardt and Z. Penzar, Physical Review B **38**, 4273 (1988).

[9] Z. Penzar and W. Ekardt, Zeitschrift für Physik D Atoms, Molecules and Clusters **17**, 69 (1990).

[10] S. Yoshida and K. Fuke, J. Chem. Phys. **111**, 3880 (1999).

[11] J. Wang, J. Zhao, L. Ma, B. Wang, and G. Wang, Physics Letters A **367**, 335 (2007).

[12] J.-G. Han and Y.-Y. Shi, Chemical Physics **266**, 33 (2001).

[13] C. Xiao, F. Hagelberg, I. Ovcharenko, and W. Lester, Journal of Molecular Structure: THEOCHEM **549**, 181 (2001).

[14] S. Mahtout and M. Belkhir, Physics Letters A **360**, 384 (2006).

[15] V. Kumar, C. Majumder, and Y. Kawazoe, Chem. Phys. Lett. **363**, 319 (2002).

[16] V. Kumar, T. M. Briere, and Y. Kawazoe, Physical Review B **68**, 155412 (2003).

[17] K. Koyasu, J. Atobe, M. Akutsu, M. Mitsui, and A. Nakajima, The Journal of Physical Chemistry A **111**, 42 (2007).

[18] F.-C. Chuang, Y.-Y. Hsieh, C.-C. Hsu, and M. A. Albao, Journal of Chemical Physics **127**, 144313 (2007).

[19] G.-f. Zhao, X.-f. Sheng, L.-l. Zhi, J.-m. Sun, and Y.-z. Gu, Journal of Molecular Structure: THEOCHEM **908**, 40 (2009).

[20] T.-g. Liu, G.-f. Zhao, and Y.-x. Wang, Physics Letters A **375**, 1120 (2011).

[21] R. Zhao-Yu, H. Ru, G. Ping, G. Ji-Kai, D. Gong-He, and W. Zhen-Yi, Chinese Physics B **17**, 2116 (2008).

[22] M. B. Abreu, A. C. Reber, and S. N. Khanna, J. Phys. Chem. Letters **5**, 3492 (2014).

[23] M. B. Abreu, A. C. Reber, and S. N. Khanna, The Journal of chemical physics **143**, 074310 (2015).

[24] X.-J. Deng, X.-Y. Kong, X.-L. Xu, H.-G. Xu, and W.-J. Zheng, ChemPhysChem **15**, 3987 (2014).

[25] X.-J. Deng, X.-Y. Kong, H.-G. Xu, X.-L. Xu, G. Feng, and W.-J. Zheng, The Journal of Physical Chemistry C **119**, 11048 (2015).

[26] G. Espinoza-Quintero, J. C. Duckworth, W. K. Myers, J. E. McGrady, and J. M. Goicoechea, Journal of the American Chemical Society **136**, 1210 (2014).

[27] S. Neukermans, X. Wang, N. Veldeman, E. Janssens, R. Silverans, and P. Lievens, International Journal of Mass Spectrometry **252**, 145 (2006).

[28] S. Furuse, K. Koyasu, J. Atobe, and A. Nakajima, J. Chem. Phys. **129**, 064311 (2008).

[29] J. Atobe, K. Koyasu, S. Furuse, and A. Nakajima, Physical Chemistry Chemical Physics **14**, 9403 (2012).

[30] X. Li, P. Claes, M. Haertelt, P. Lievens, E. Janssens, and A. Fielicke, Physical Chemistry Chemical Physics **18**, 6291 (2016).

[31] Y. Li, N. M. Tam, P. Claes, A. P. Woodham, J. T. Lyon, V. T. Ngan, M. T. Nguyen, P. Lievens, A. Fielicke, and E. Janssens, The Journal of Physical Chemistry A **118**, 8198 (2014).

[32] Y. Li, J. T. Lyon, A. P. Woodham, A. Fielicke, and E. Janssens, ChemPhysChem **15**, 328 (2014).

[33] V. Chauhan, M. B. Abreu, A. C. Reber, and S. N. Khanna, Physical Chemistry Chemical Physics **17**, 15718 (2015).

[34] J. M. Goicoechea and J. E. McGrady, Dalton Transactions **44**, 6755 (2015).

[35] V. Kumar and Y. Kawazoe, Phys. Rev. B **65**, 073404 (2002).

[36] L.-j. Guo, G.-f. Zhao, Y.-z. Gu, X. Liu, and Z. Zeng, Phys. Rev. B **77**, 195417 (2008).

[37] H. Kawamura, V. Kumar, and Y. Kawazoe, Materials Transactions. **45**, 1429 (2004).

[38] S. Khanna, B. Rao, P. Jena, and S. Nayak, Chemical physics letters **373**, 433 (2003).

[39] K. Koyasu, M. Akutsu, M. Mitsui, and A. Nakajima, Journal of the American Chemical Society **127**, 4998 (2005).

[40] X. Kong, H.-G. Xu, and W. Zheng, The Journal of chemical physics **137**, 064307 (2012).

[41] W. Zheng, J. M. Nilles, D. Radisic, and K. H. Bowen Jr, J. Chem. Phys. **122**, 071101 (2005).

[42] D. Bandyopadhyay, Journal of molecular modeling **18**, 3887 (2012).

[43] J. Wang, L. Ma, J. Zhao, and G. Wang, Journal of Physics: Condensed Matter **20**, 335223 (2008).

[44] W.-J. Zhao and Y.-X. Wang, Chemical Physics **352**, 291 (2008).

[45] X.-J. Deng, X.-Y. Kong, X.-L. Xu, H.-G. Xu, and W.-J. Zheng, RSC Advances **4**, 25963 (2014).

[46] N. Kapila, V. Jindal, and H. Sharma, Physica B: Condensed Matter **406**, 4612 (2011).

[47] W.-J. Zhao and Y.-X. Wang, Journal of Molecular Structure: THEOCHEM **901**, 18 (2009).

[48] S. Mahtout and Y. Tariket, Chemical Physics **472**, 270 (2016).

[49] J. Wang and J.-G. Han, The Journal of Physical Chemistry B **110**, 7820 (2006).

[50] Y.-Y. Jin, Y. Tian, X. Kuang, C. Lu, J. L. Cabellos, S. Mondal, and G. Merino, The Journal of Physical Chemistry C (2016).

[51] J. Wang and J.-G. Han, Chemical Physics **342**, 253 (2007).

[52] R. Trivedi, K. Dhaka, and D. Bandyopadhyay, RSC Advances **4**, 64825 (2014).

[53] X.-J. Hou, G. Gopakumar, P. Lievens, and M. T. Nguyen, J. Phys. Chem. A **111**, 13544 (2007).

[54] J. Wang and J.-G. Han, The Journal of Physical Chemistry A **110**, 12670 (2006).

[55] X. Jin, G. Espinoza-Quintero, B. Below, V. Arcisauskaite, J. M. Goicoechea, and J. E. McGrady, Journal of Organometallic Chemistry **792**, 149 (2015).

[56] S. Zhang, C. G. Luo, H. Y. Li, C. Lu, G. Q. Li, and Z. W. Lu, Materials Chemistry and Physics **160**, 227 (2015).

[57] R.-N. Zhao, J.-G. Han, and Y. Duan, Thin Solid Films **556**, 571 (2014).

[58] P. Shao, X.-Y. Kuang, L.-P. Ding, M.-M. Zhong, and Z.-h. Wang, Physica B: Condensed Matter **407**, 4379 (2012).

[59] S. Zhang, Y. Zhang, X. Yang, C. Lu, G. Li, and Z. Lu, Journal of Materials Science **50**, 6180 (2015).

[60] C. Yang, S. H. Jia, M. F. Ma, S. Zhang, C. Lu, and G. Q. Li, The European Physical Journal D **69**, 1 (2015).

[61] X.-X. Ji, J. Li, C. Wang, S. Zhang, C. Lu, and G.-Q. Li, Molecular Physics **113**, 3567 (2015).

[62] J.-G. Han, R.-N. Zhao, and Y. Duan, The Journal of Physical Chemistry A **111**, 2148 (2007).

[63] X. Huang, H.-G. Xu, S. Lu, Y. Su, R. King, J. Zhao, and W. Zheng, Nanoscale **6**, 14617 (2014).

[64] L. Xia, Z. Gao-Feng, G. Ling-Ju, W. Xian-Wei, Z. Jun, J. Qun, and L. You-Hua, Chinese Physics **16**, 3359 (2007).

[65] W. Ji and C. Luo, International Journal of Quantum Chemistry **112**, 2525 (2012).

[66] V. Kumar and Y. Kawazoe, Physical review letters **90**, 055502 (2003).

[67] H.-G. Xu, X.-Y. Kong, X.-J. Deng, Z.-G. Zhang, and W.-J. Zheng, The Journal of chemical physics **140**, 024308 (2014).

[68] H.-G. Xu, Z.-G. Zhang, Y. Feng, J. Yuan, Y. Zhao, and W. Zheng, Chemical Physics Letters **487**, 204 (2010).

[69] H.-G. Xu, Z.-G. Zhang, Y. Feng, and W. Zheng, Chemical Physics Letters **498**, 22 (2010).

[70] M. Torres, E. Fernández, and L. Balbás, The Journal of Physical Chemistry C **115**, 335 (2010).

[71] T. Iwasa and A. Nakajima, The Journal of Physical Chemistry C **116**, 14071 (2012).

[72] R. Robles and S. N. Khanna, Physical Review B **80**, 115414 (2009).

[73] A. Willand, M. Gramzow, S. A. Ghasemi, L. Genovese, T. Deutsch, K. Reuter, and S. Goedecker, Physical Review B **81**, 201405 (2010).

[74] R. Siegel, Annual Review of Materials Science **21**, 559 (1991).

[75] C. Casari, A. L. Bassi, L. Ravagnan, F. Siviero, C. Lenardi, P. Piseri, G. Bongiorno, C. Bottani, and P. Milani, Physical review B **69**, 075422 (2004).

[76] G. E. Johnson, R. Mitric, E. C. Tyo, V. Bonacic-Koutecky, and A. Castleman Jr, Journal of the American Chemical Society **130**, 13912 (2008).

[77] Y. Yong, B. Song, and P. He, The Journal of Physical Chemistry C **115**, 6455 (2011).

[78] C. Ashman, S. Khanna, F. Liu, P. Jena, T. Kaplan, and M. Mostoller, Physical Review B **55**, 15868 (1997).

[79] Y. Shichibu, Y. Negishi, T. Watanabe, N. K. Chaki, H. Kawaguchi, and T. Tsukuda, The Journal of Physical Chemistry C **111**, 7845 (2007).

[80] P. Melinon, V. Paillard, V. Dupuis, A. Perez, P. Jensen, A. Hoareau, J. Perez, J. Tuaillon, M. Broyer, J. Vialle, et al., International Journal of Modern Physics B **9**, 339 (1995).

[81] A. Perez, P. Melinon, V. Dupuis, P. Jensen, B. Prevel, J. Tuaillon, L. Bardotti, C. Martet, M. Treilleux, M. Broyer, et al., Journal of Physics D: Applied Physics **30**, 709 (1997).

[82] E. Schrödinger, Physical Review **28**, 1049 (1926).

[83] M. Born and R. Oppenheimer, Annalen der Physik **389**, 457 (1927).

[84] A. Szabo and N. S. Ostlund, *Modern quantum chemistry: Intro to advanced electronic structure theory* (1996).

[85] W. Pauli, Zeitschrift für Physik A Hadrons and Nuclei **31**, 373 (1925).

[86] J. C. Slater, Physical Review **34**, 1293 (1929).

[87] D. R. Hartree, in *Mathematical Proceedings of the Cambridge Philosophical Society* (Cambridge Univ Press, 1928), vol. 24, pp. 111–132.

[88] V. Fock, Zeitschrift für Physik **61**, 126 (1930).

[89] C. C. J. Roothaan, Reviews of modern physics **23**, 69 (1951).

[90] W. Koch and M. C. Holthausen, *A chemist's guide to density functional theory* (John Wiley & Sons, 2015).

[91] R. G. Parr, *Density functional theory of atoms and molecules* (Springer, 1980).

[92] P. Hohenberg and W. Kohn, Physical review **136**, B864 (1964).

[93] W. Kohn and L. J. Sham, Physical review **140**, A1133 (1965).

[94] G. E. Scuseria and V. N. Staroverov, *Progress in the development of exchange-correlation functionals* (2005).

[95] m. F. Bloch, Zeitschrift für Physik **57**, 545 (1929).

[96] P. A. Dirac, in *Mathematical Proceedings of the Cambridge Philosophical Society* (Cambridge Univ Press, 1930), vol. 26, pp. 376–385.

[97] S. Vosko, L. Wilk, and M. Nusair, Canadian Journal of physics **58**, 1200 (1980).

[98] J. P. Perdew and A. Zunger, Physical Review B **23**, 5048 (1981).

[99] L. A. Cole and J. Perdew, Physical Review A **25**, 1265 (1982).

[100] J. P. Perdew and Y. Wang, Physical Review B **45**, 13244 (1992).

[101] J. P. Perdew, J. Chevary, S. Vosko, K. A. Jackson, M. R. Pederson, D. Singh, and C. Fiolhais, Physical Review B **46**, 6671 (1992).

[102] G. J. Laming, V. Termath, and N. C. Handy, The Journal of chemical physics **99**, 8765 (1993).

[103] M. Filatov and W. Thiel, Molecular Physics **91**, 847 (1997).

[104] J. P. Perdew, K. Burke, and M. Ernzerhof, Physical review letters **77**, 3865 (1996).

[105] A. D. Becke, The Journal of Chemical Physics **98**, 1372 (1993).

[106] P. Stephens, F. Devlin, C. Chabalowski, and M. J. Frisch, The Journal of Physical Chemistry **98**, 11623 (1994).

[107] C. Adamo and V. Barone, The Journal of chemical physics **110**, 6158 (1999).

[108] G. Frenking, I. Antes, M. Böhme, S. Dapprich, A. W. Ehlers, V. Jonas, A. Neuhaus, M. Otto, R. Stegmann, A. Veldkamp, et al., Reviews in Computational Chemistry, Volume 8 pp. 63–144 (1996).

[109] A. Veldkamp and S. F. Vyboishchikov, Reviews in Computational Chemistry **8**, 63 (2009).

[110] T. R. Cundari, M. T. Benson, M. L. Lutz, and S. O. Sommerer, Reviews in Computational Chemistry, Volume 8 pp. 145–202 (1996).

[111] C. Garoufalis, A. D. Zdetsis, and S. Grimme, Physical review letters **87**, 276402 (2001).

[112] C. J. Cramer and D. G. Truhlar, Physical Chemistry Chemical Physics **11**, 10757 (2009).

[113] F. Jensen, *Introduction to computational chemistry* (John Wiley & Sons, 2013).

[114] S. Schnatterly and J. Blakemore, *Solid state physics* (1970).

[115] M. C. Payne, M. P. Teter, D. C. Allan, T. Arias, and J. Joannopoulos, Reviews of Modern Physics **64**, 1045 (1992).

[116] C. Lee, W. Yang, and R. G. Parr, Physical review B **37**, 785 (1988).

[117] M. J. Frisch, G. W. Trucks, H. B. Schlegel, G. E. Scuseria, M. A. Robb, J. R. Cheeseman, V. G. Zakrzewski, J. A. J. Montgomery, R. E. Stratmann, J. C. Burant, et al., *Gaussian 03, revision e. 01, suite of programs for ab initio calculation.*

[118] P. J. Hay and W. R. Wadt, The Journal of Chemical Physics **82**, 299 (1985).

[119] M. Kumar, N. Bhattacharyya, and D. Bandyopadhyay, J. Mol. Model. **18**, 405 (2012).

[120] D. Bandyopadhyay, P. Kaur, and P. Sen, J. Phys. Chem. A **114**, 12986 (2010).

[121] T. B. Tai and M. T. Nguyen, Journal of Chemical Theory and Computation **7**, 1119 (2011).

[122] D. Bandyopadhyay, Journal of Applied Physics **104**, 084308 (2008).

[123] D. Bandyopadhyay and M. Kumar, Chemical Physics **353**, 170 (2008).

[124] D. Bandyopadhyay, The European Physical Journal D-Atomic, Molecular, Optical and Plasma Physics **54**, 643 (2009).

[125] D. Bandyopadhyay and P. Sen, J. Phys. Chem. A **114**, 1835 (2010).

[126] M. Islam and A. Ray, Chemical physics letters **153**, 496 (1988).

[127] J. E. Northrup and M. L. Cohen, Chemical physics letters **102**, 440 (1983).

[128] G. Pacchioni, Chemical physics letters **107**, 70 (1984).

[129] G. Pacchioni and J. Kouteckỳ, The Journal of chemical physics **84**, 3301 (1986).

[130] D. Dai and K. Balasubramanian, The Journal of chemical physics **96**, 8345 (1992).

[131] P. Deutsch, L. Curtiss, and J. Blaudeau, Chemical physics letters **270**, 413 (1997).

[132] T. Abtew and D. Drabold, Physical Review B **75**, 045201 (2007).

[133] S. Nagendran, S. S. Sen, H. W. Roesky, D. Koley, H. Grubmuller, A. Pal, and R. Herbst-Irmer, Organometallics **27**, 5459 (2008).

[134] N. Bell, F. Glockling, M. Schneider, H. Shearer, and M. Wilbey, Acta Crystallographica Section C: Crystal Structure Communications **40**, 625 (1984).

[135] I. Shim, J. E. Kingcade Jr, and K. A. Gingerich, The Journal of chemical physics **89**, 3104 (1988).

[136] B. Reddy, S. Nayak, S. Khanna, B. Rao, and P. Jena, The Journal of Physical Chemistry A **102**, 1748 (1998).

[137] J. Ho, M. L. Polak, K. M. Ervin, and W. Lineberger, The Journal of chemical physics **99**, 8542 (1993).

[138] V. G. Grigoryan and M. Springborg, Physical Chemistry Chemical Physics **3**, 5135 (2001).

[139] J. O. Noell, M. D. Newton, P. J. Hay, R. L. Martin, and F. W. Bobrowicz, The Journal of Chemical Physics **73**, 2360 (1980).

[140] D. Bandyopadhyay, J. Mol. Model. **18**, 737 (2012).

[141] E. Wigner and E. Witmer, Z. Phys **51**, 859 (1928).

[142] D. Bandyopadhyay, Mole. Sim. **35**, 381 (2009).

[143] S. Hati and D. Datta, The Journal of Physical Chemistry **98**, 10451 (1994).

[144] T. K. Ghanty and S. K. Ghosh, The Journal of Physical Chemistry **98**, 9197 (1994).

[145] J. Paier, M. Marsman, and G. Kresse, The Journal of chemical physics **127**, 024103 (2007).

[146] A. R. Oganov and C. W. Glass, The Journal of chemical physics **124**, 244704 (2006).

[147] G. Kresse, Phys. Rev. B **54**, 11 (1996).

[148] A. Frisch, *Gaussian 09: User's Reference* (Gaussian, 2009).

[149] J. P. Perdew, K. Burke, and M. Ernzerhof, Phys. Rev. Lett **78**, 1396 (1997).

[150] K. L. Schuchardt, B. T. Didier, T. Elsethagen, L. Sun, V. Gurumoorthi, J. Chase, J. Li, and T. L. Windus, Journal of chemical information and modeling **47**, 1045 (2007).

[151] W. R. Wadt and P. J. Hay, The Journal of Chemical Physics **82**, 284 (1985).

[152] A. M. Köster, P. Calaminici, M. E. Casida, R. Flores-Moreno, G. Geudtner, A. Goursot, T. Heine, A. Ipatov, F. Janetzko, J. Del Campo, et al., The International deMon Developers Community, Cinvestav-IPN, México (2006).

[153] W. Ekardt, Physical Review B **29**, 1558 (1984).

[154] P. J. Roach, W. H. Woodward, A. C. Reber, S. N. Khanna, and A. W. Castleman Jr, Physical Review B **81**, 195404 (2010).

[155] W. H. Woodward, A. Reber, J. C. Smith, S. Khanna, and A. Castleman Jr, The Journal of Physical Chemistry C **117**, 7445 (2013).

[156] H. Hiura, T. Miyazaki, and T. Kanayama, Phys. Rev. Lett. **86**, 1733 (2001).

[157] R. Bader, *A quantum theory, clarendon* (1990).

[158] S. Lu, L. Hu, X.-L. Xu, H.-G. Xu, H. Chen, and W. Zheng, Physical Chemistry Chemical Physics (2016).

[159] A. Ugrinov and S. C. Sevov, Journal of the American Chemical Society **124**, 10990 (2002).

[160] G. Kresse and D. Joubert, Phys. Rev. B **59**, 1758 (1999).

[161] G. Kresse and J. Furthmüller, Phys. Rev. B **54**, 11169 (1996).

[162] W. Press, B. Flannery, S. Teukolsky, and W. Vetterling (1986).

[163] A. K. Singh, T. M. Briere, V. Kumar, and Y. Kawazoe, Physical review letters **91**, 146802 (2003).

[164] A. Palaria, G. Klimeck, and A. Strachan, Physical Review B **78**, 205315 (2008).

[165] R. Zhang, H.-L. Lee, W.-K. Li, and B. K. Teo, The Journal of Physical Chemistry B **109**, 8605 (2005).

[166] J. Wang, J. Zhao, L. Ma, G. Wang, and R. B. King, Nanotechnology **18**, 235705 (2007).

[167] M. Vanević, V. M. Stojanović, and M. Kindermann, Physical Review B **80**, 045410 (2009).

[168] T. He, M. Zhao, W. Li, X. Lin, X. Zhang, X. Liu, Y. Xia, and L. Mei, Nanotechnology **19**, 205707 (2008).

[169] K. M. Alam and A. K. Ray, Nanotechnology **18**, 495706 (2007).

[170] W. Liang, M. Bockrath, D. Bozovic, J. H. Hafner, M. Tinkham, and H. Park, Nature **411**, 665 (2001).

[171] S. Frank, P. Poncharal, Z. Wang, and W. A. de Heer, Science **280**, 1744 (1998).

[172] Y. Chen, D. T. Shaw, X. Bai, E. Wang, C. Lund, W. Lu, and D. Chung, Applied physics letters **78**, 2128 (2001).

[173] A. Dillon and M. Heben, Applied Physics A **72**, 133 (2001).

[174] N. Lee, D. Chung, I. Han, J. Kang, Y. Choi, H. Kim, S. Park, Y. Jin, W. Yi, M. Yun, et al., Diamond Relat. Mater **10**, 265 (2001).

[175] H. Sugie, M. Tanemura, V. Filip, K. Iwata, K. Takahashi, and F. Okuyama, Applied Physics Letters **78**, 2578 (2001).

[176] C. L. Cheung, J. H. Hafner, T. W. Odom, K. Kim, and C. M. Lieber, Applied Physics Letters **76**, 3136 (2000).

[177] P. G. Collins, K. Bradley, M. Ishigami, and A. Zettl, science **287**, 1801 (2000).

[178] M. W. Heaven, A. Dass, P. S. White, K. M. Holt, and R. W. Murray, Journal of the American Chemical Society **130**, 3754 (2008).

[179] V. Chauhan, S. Sahoo, and S. N. Khanna, Journal of the American Chemical Society (2016).

[180] Z. Liu, X. Wang, and H. Zhu, RSC Advances **3**, 1450 (2013).

[181] L. Boyer, Physical Review Letters **42**, 584 (1979).

Appendix A

Ni doped Germanium nanoclusters

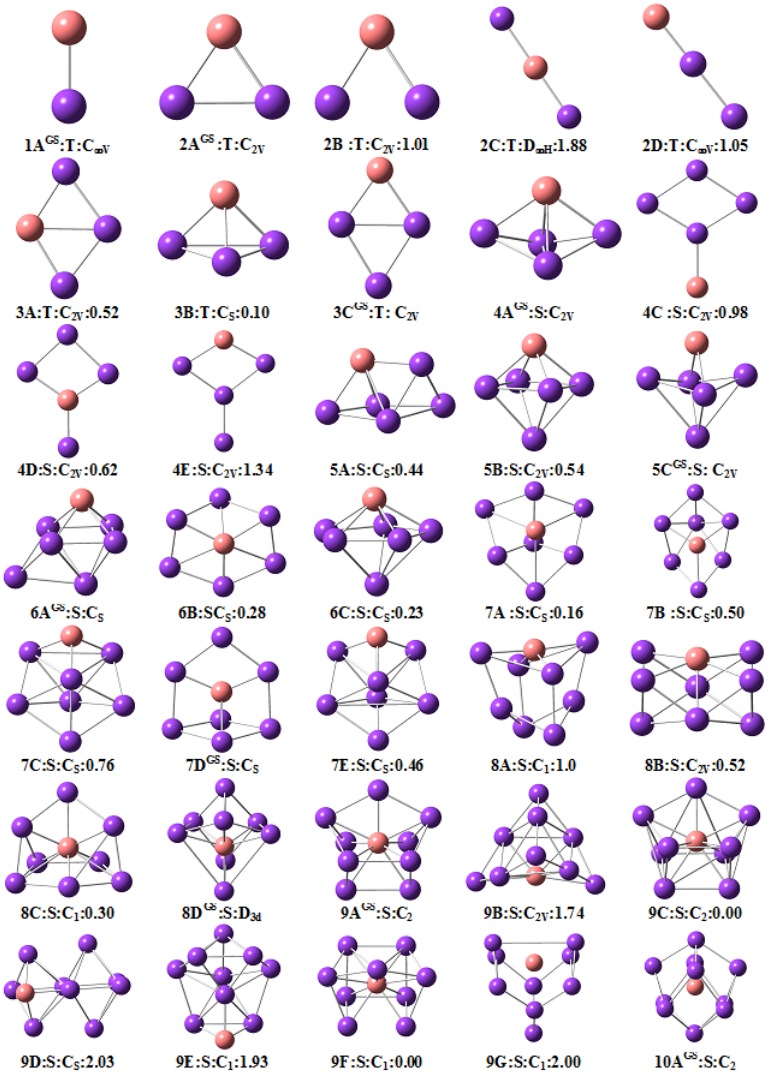

Figure A.1: Optimized structures of neutral Ge_nNi (n=1–20) clusters.

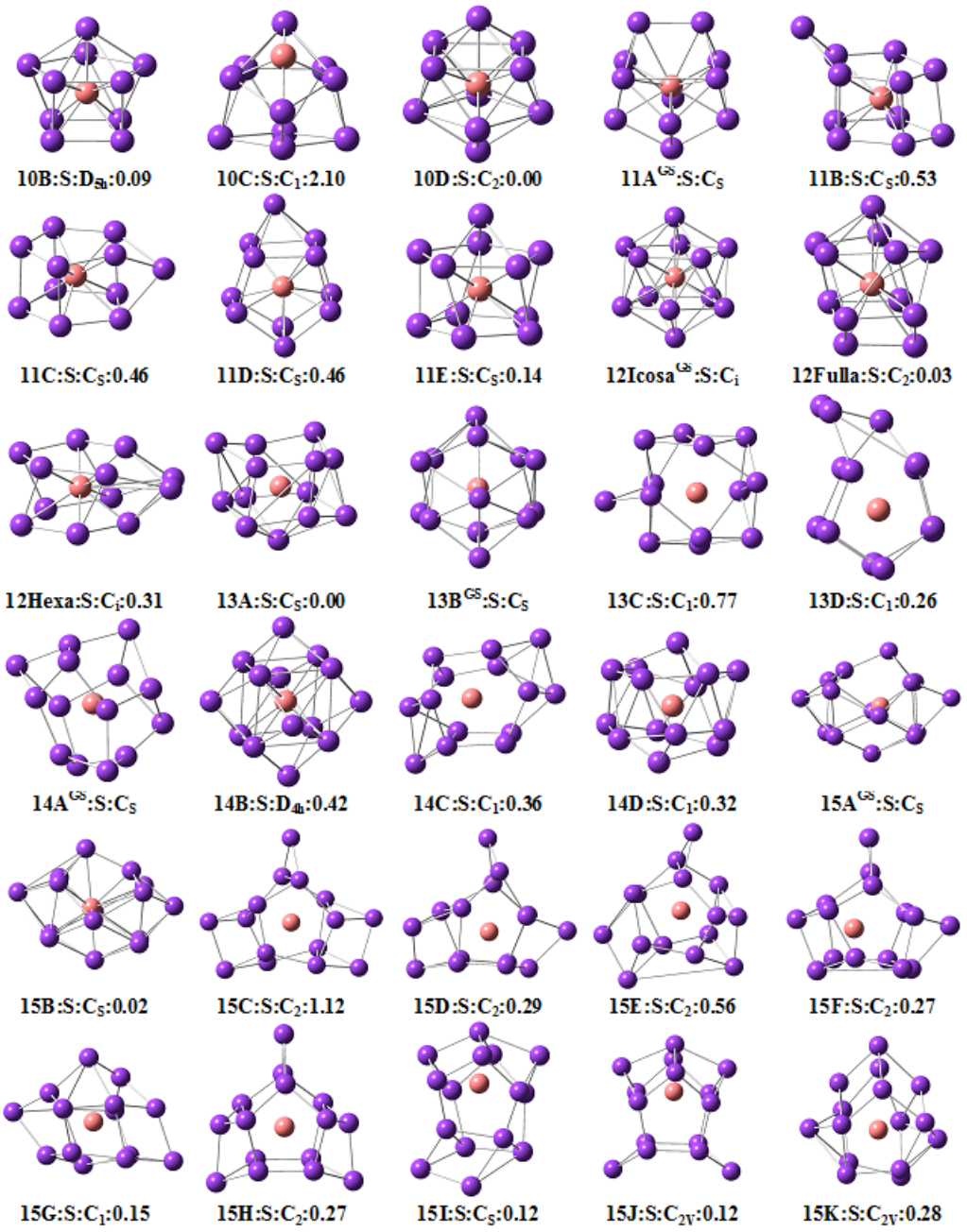

Figure A.2: Optimized structures of neutral Ge_nNi (n=1–20) clusters with spin state (S singlet, T triplet), point group symmetry and energy with respect to the calculated ground state in each size. Purple balls Germanium atoms, orange balls nickel atoms..

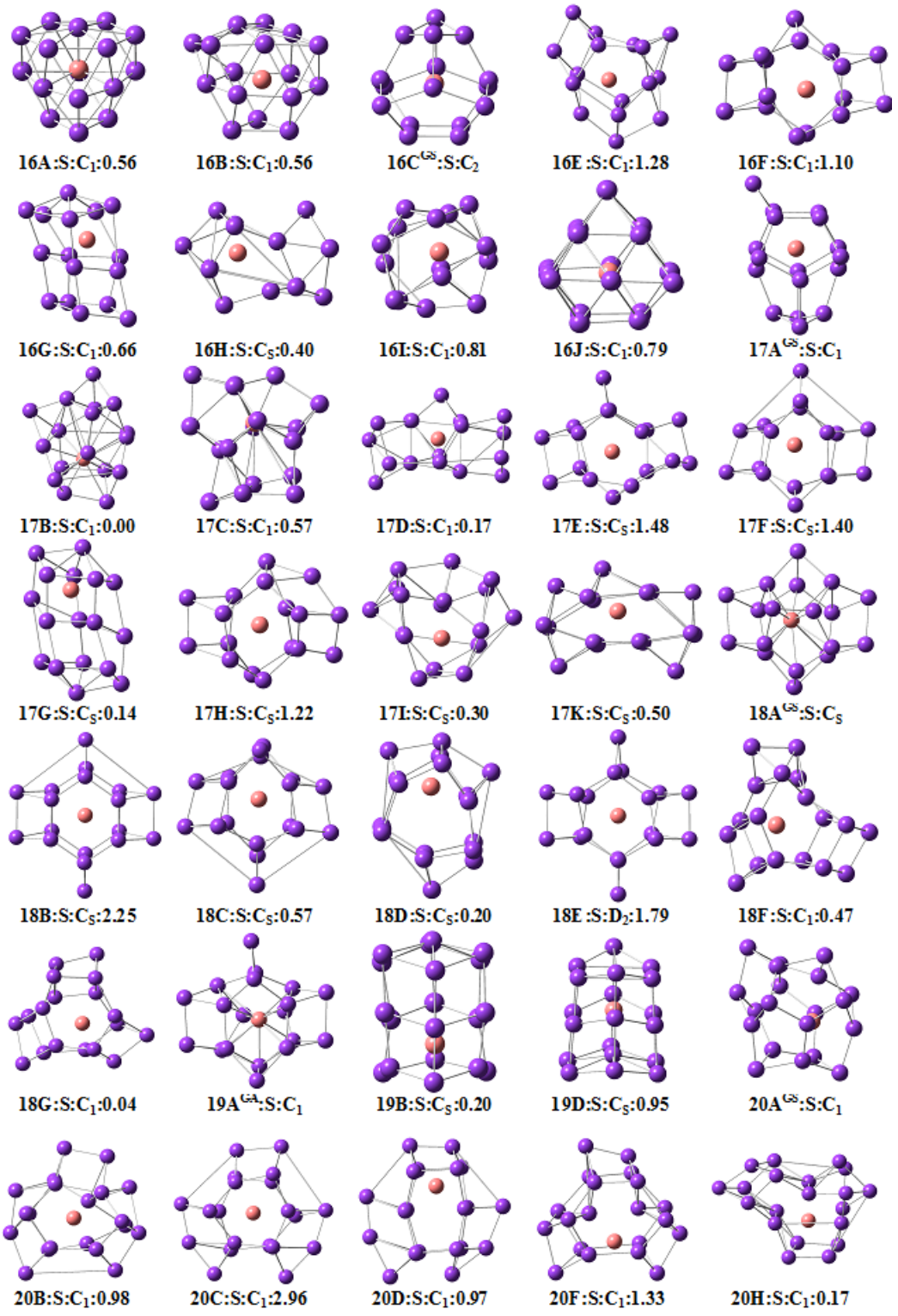

Figure A.3: Optimized structures of neutral Ge_nNi (n=1–20) clusters.

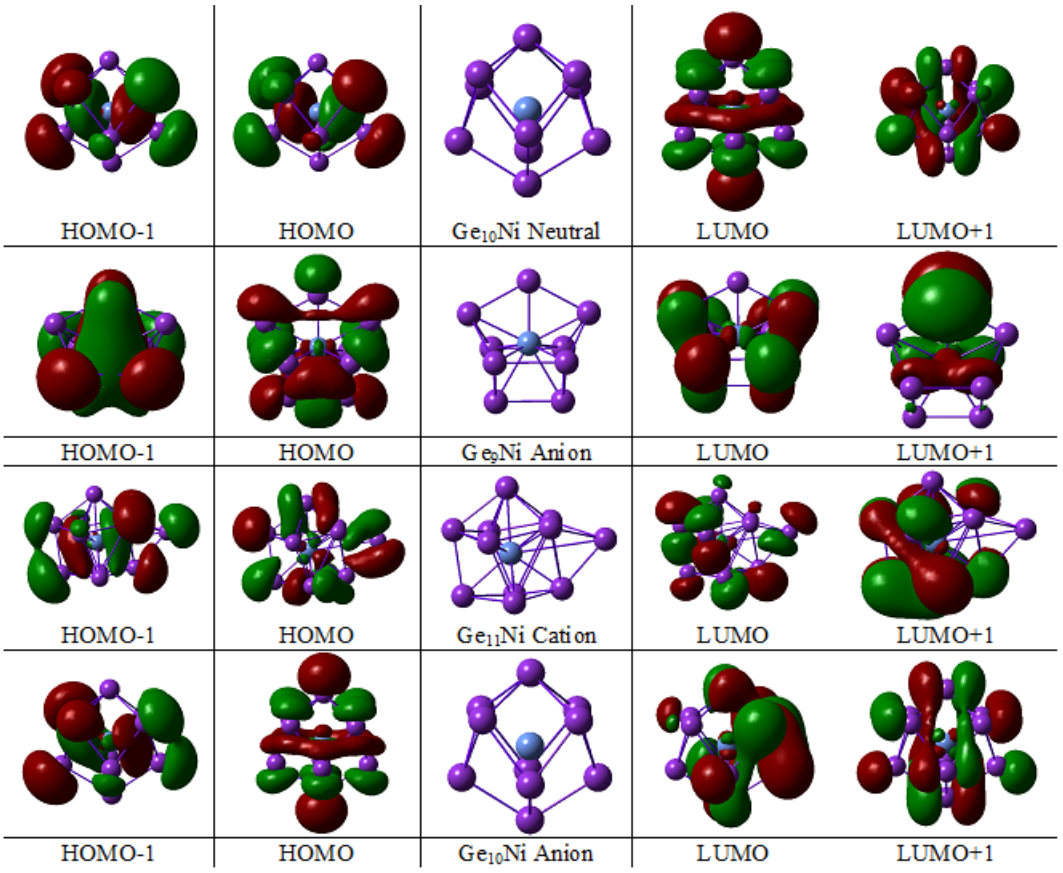

Figure A.4: Different Valence orbitals of 20-electron ground state clusters

Gaussian basis set for Ni and Ge

```
Ni     0
S   3   1.00
     7.6200000           -0.4082550
     2.2940000            0.7455308
     0.8760000            0.5325721
S   4   1.00
     7.6200000            0.1872591
     2.2940000           -0.3966964
     0.8760000           -0.4954003
     0.1153000            1.0844343
S   1   1.00
     0.0396000            1.0000000
P   3   1.00
    23.6600000           -0.0481558
     2.8930000            0.6258473
     0.9435000            0.4715158
P   1   1.00
     0.0840000            1.0000000
P   1   1.00
     0.0240000            1.0000000
D   4   1.00
    42.7200000            0.0372699
    11.7600000            0.1956103
     3.8170000            0.4561273
     1.1690000            0.5621587
D   1   1.00
     0.2836000            1.0000000
****

NI     0
NI-ECP     2     10
d potential
  3
1    469.9324331          -10.0000000
2     85.4236411          -69.4084805
2     21.2674984          -12.0951020
s-d potential
  4
0    162.1686097            3.0000000
1    176.5333232           22.0253618
2     68.9562010          443.0181088
2     13.5792838          145.5696411
p-d potential
  4
0     69.0181506            5.0000000
1    275.5955596            4.9882824
2     47.1315453          256.6945853
2     12.9874075           78.4754450
```

```
Ge 0
S   2   1.00
     0.8935000           -2.1756591
     0.4424000            2.4493467
S   1   1.00
     0.1162000            1.0000000
P   2   1.00
     1.8770000           -0.1006779
     0.2623000            1.0306256
P   1   1.00
     0.0798000            1.0000000
P   1   1.00
     0.0209000            1.0000000
D   1   1.00
     0.2460000            1.0000000
****

GE     0
GE-ECP     3     28
f-ul potential
  5
1    318.2167583          -28.0000000
2     61.5370967          -180.9891676
2     13.2986899          -55.0043909
2      3.8985215          -19.7906526
2      1.2137666          -1.8533572
s-ul potential
  5
0    205.1886932            3.0000000
1     68.9790278           65.2262558
2     27.9194879          225.2354522
2      8.5481650           94.0125472
2      2.3173734           29.9415005
p-ul potential
  5
0     33.2488002            5.0000000
1     15.7777247           23.4778157
2     14.9260722           45.0980414
2      5.8416394           56.3326957
2      1.8349575           16.6058640
d-ul potential
  5
0     42.0206343            3.0000000
1     19.2096363           23.7371518
2      9.4133917           56.4792249
2      3.3282907           25.8901835
2      0.8522331            3.0229836
```

Appendix B

Cr doped Germanium nanoclusters

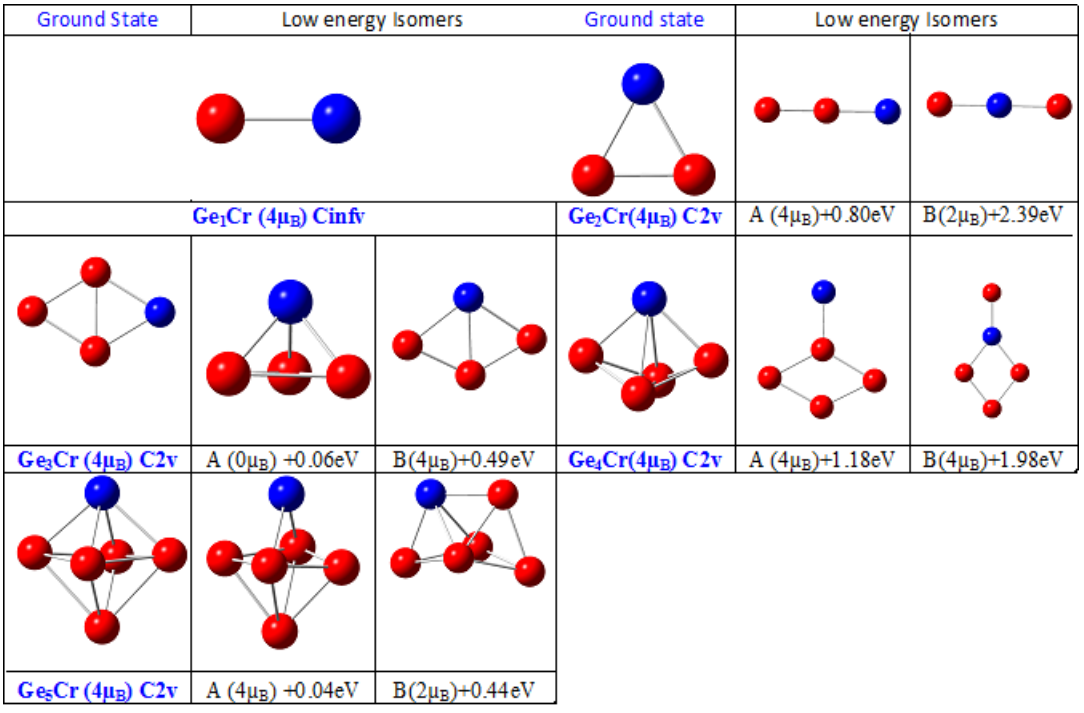

Figure B.1: Selected optimized low energy isomers (n=1 to 5) the spin magnetic moments and point group symmetries.

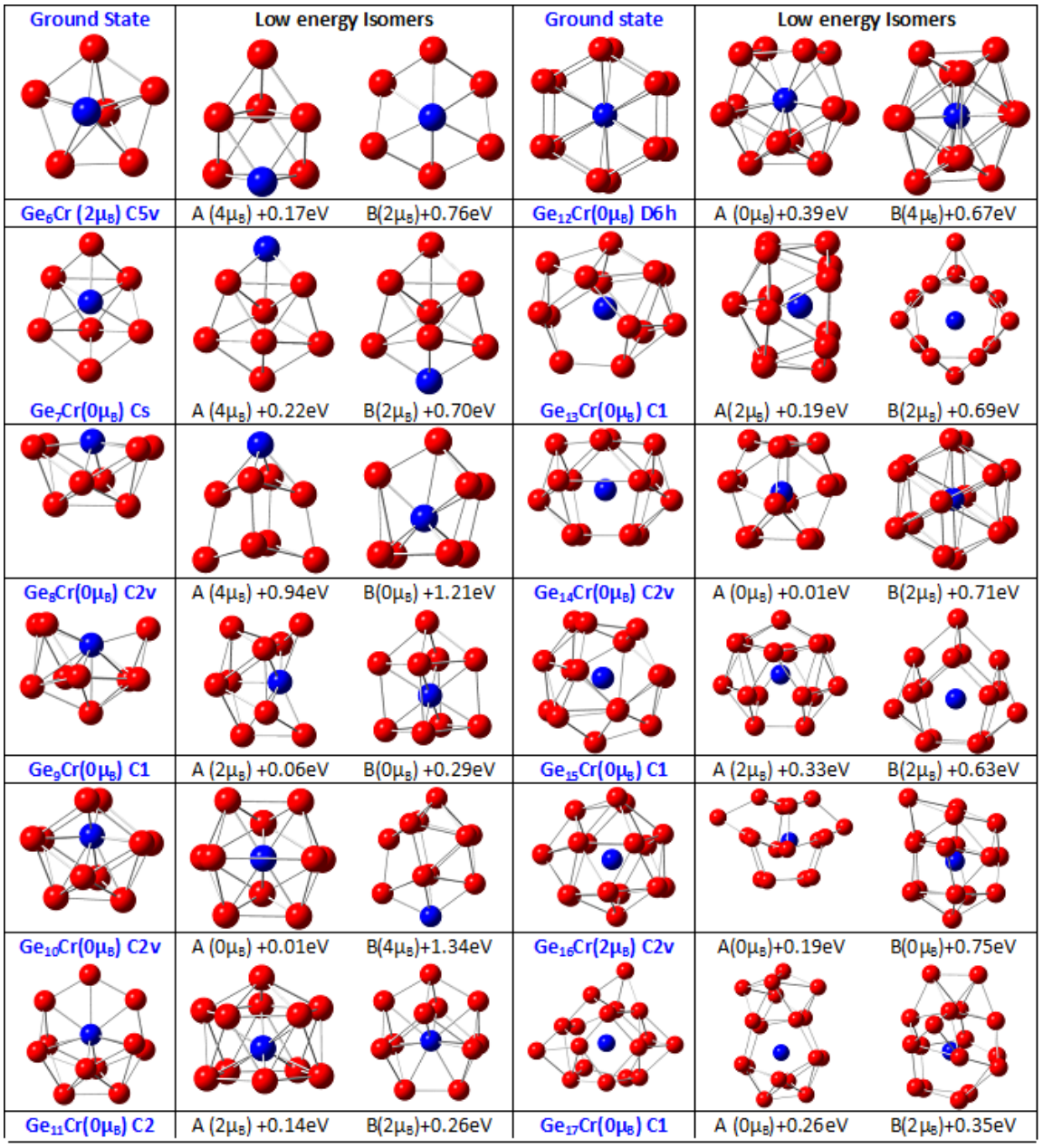

Figure B.2: Selected optimized low energy isomers (n=6 to 17) the spin magnetic moments and point group symmetries.

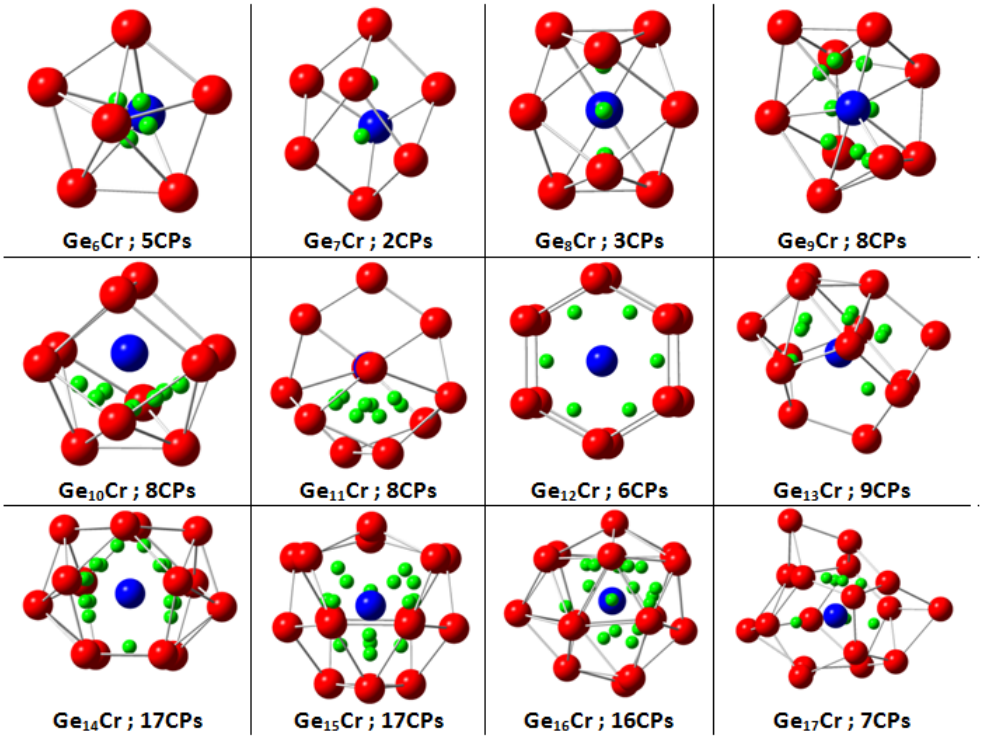

Figure B.3: Ground state structures with the positions of (3, +3) Cage Critical Points (CCPs).

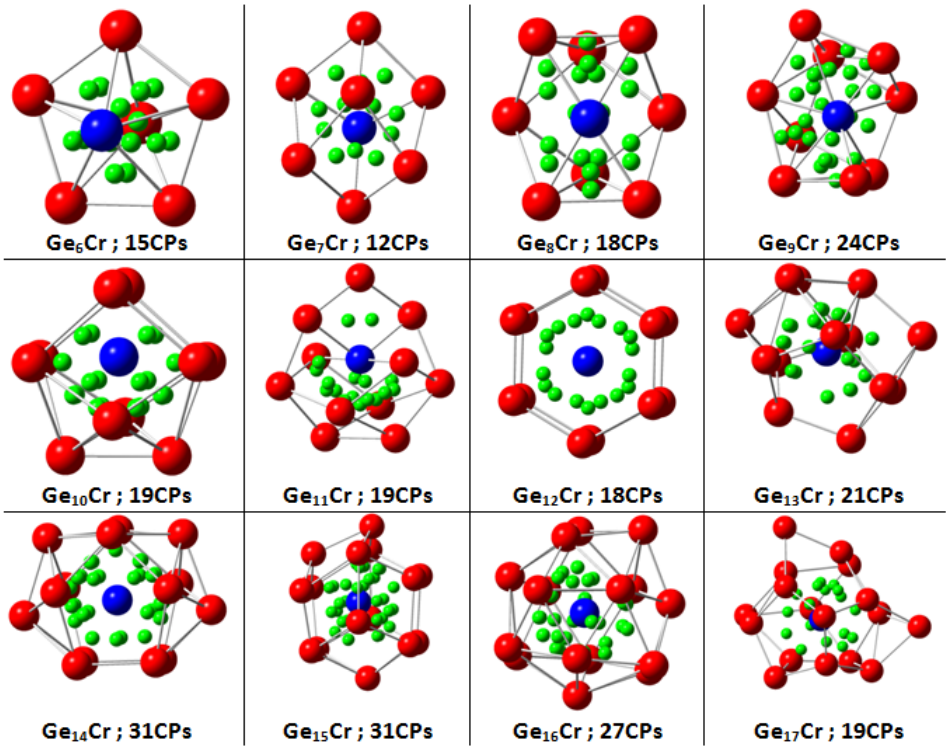

Figure B.4: Ground state structures with the positions of (3, +1) Ring Critical Points (RCPs).

Gaussian basis set for Cr and Ge

```
Cr 0
6-311g
****
 Ge 0
S   2   1.00
     0.8935000          -2.1756591
     0.4424000           2.4493467
S   1   1.00
     0.1162000           1.0000000
P   2   1.00
     1.8770000          -0.1006779
     0.2623000           1.0306256
P   1   1.00
     0.0798000           1.0000000
P   1   1.00
     0.0209000           1.0000000
D   1   1.00
     0.2460000           1.0000000
****

GE     0
GE-ECP     3     28
f-ul potential
 5
1    318.2167583          -28.0000000
2     61.5370967         -180.9891676
2     13.2986899          -55.0043909
2      3.8985215          -19.7906526
2      1.2137666           -1.8533572
s-ul potential
 5
0    205.1886932            3.0000000
1     68.9790278           65.2262558
2     27.9194879          225.2354522
2      8.5481650           94.0125472
2      2.3173734           29.9415005
p-ul potential
 5
0     33.2488002            5.0000000
1     15.7777247           23.4778157
2     14.9260722           45.0980414
2      5.8416394           56.3326957
2      1.8349575           16.6058640
d-ul potential
 5
0     42.0206343            3.0000000
1     19.2096363           23.7371518
2      9.4133917           56.4792249
2      3.3282907           25.8901835
2      0.8522331            3.0229836
```

Appendix C

Au doped Ge_n^- nanoclusters

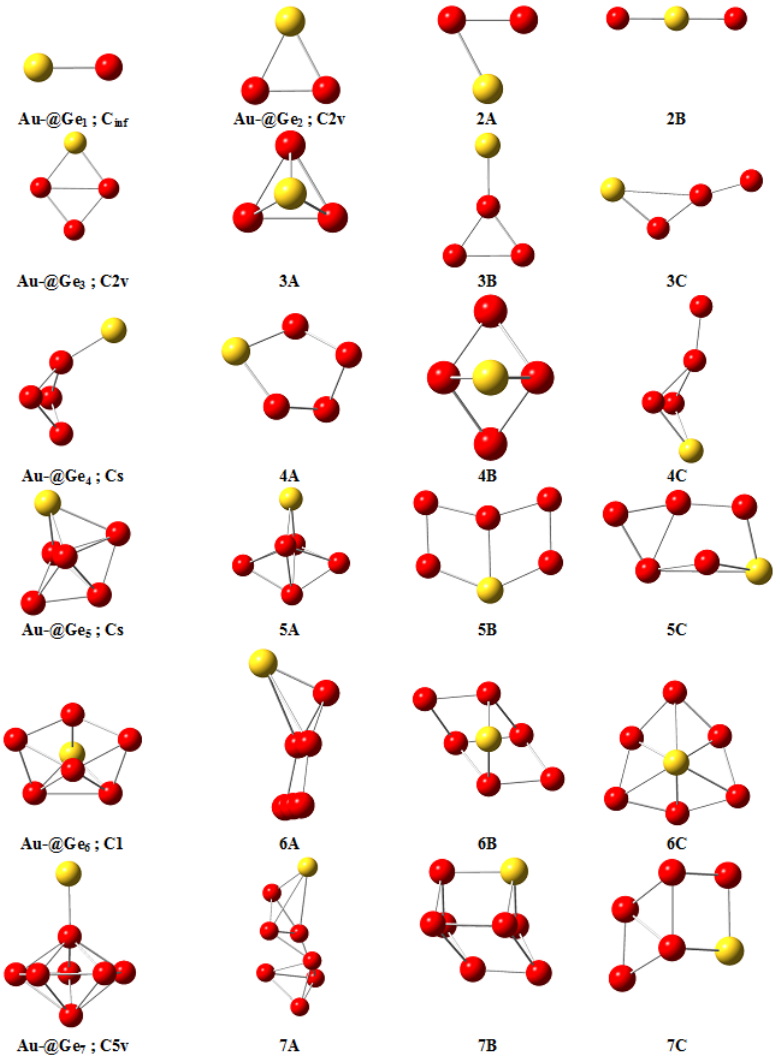

Figure C.1: Selected optimized low energy isomers $AuGe_n^-$ (n=1 to 7) First column has the ground state structure and next A,B and C are the nearest energy isomers. Red and yellow balls represent Ge and Au atoms respectively.

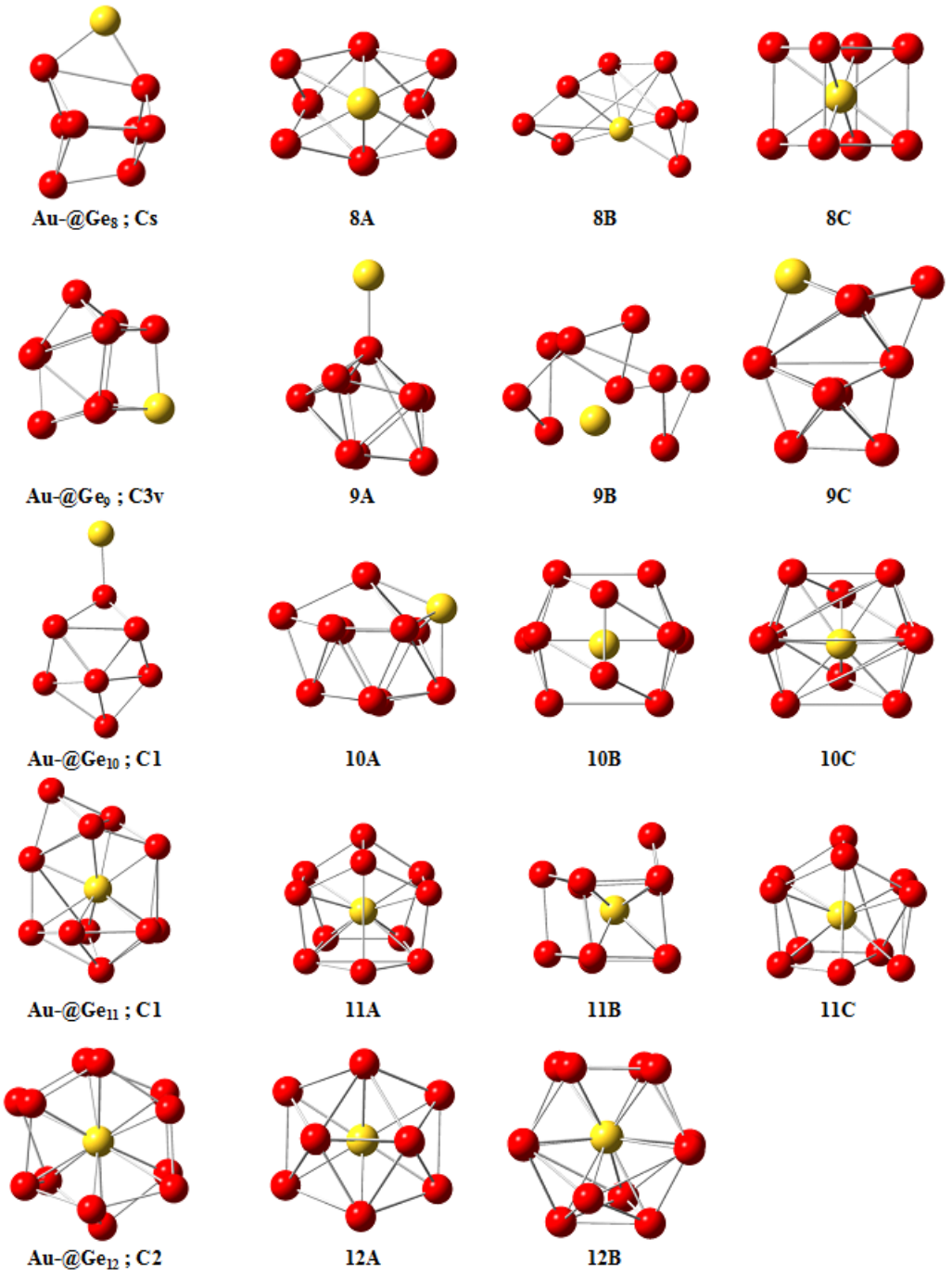

Figure C.2: Selected optimized low energy isomers $AuGe_n^-$ (n=8 to 12) First column has the ground state structure and next A,B and C are the nearest energy isomers. Red and yellow balls represent Ge and Au atoms respectively.

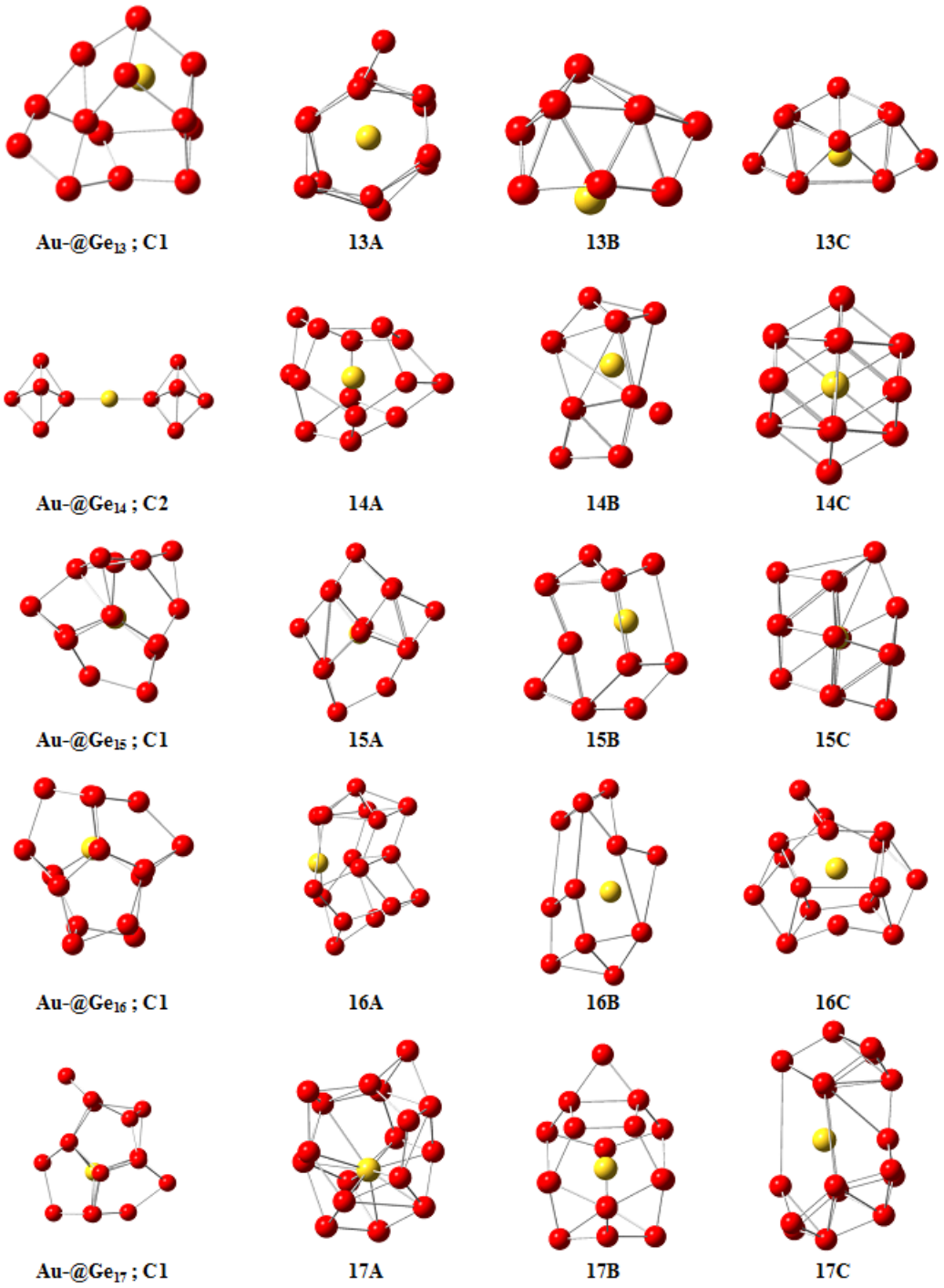

Figure C.3: Selected optimized low energy isomers $AuGe_n^-$ (n=13 to 17) First column has the ground state structure and next A,B and C are the nearest energy isomers. Red and yellow balls represent Ge and Au atoms respectively.

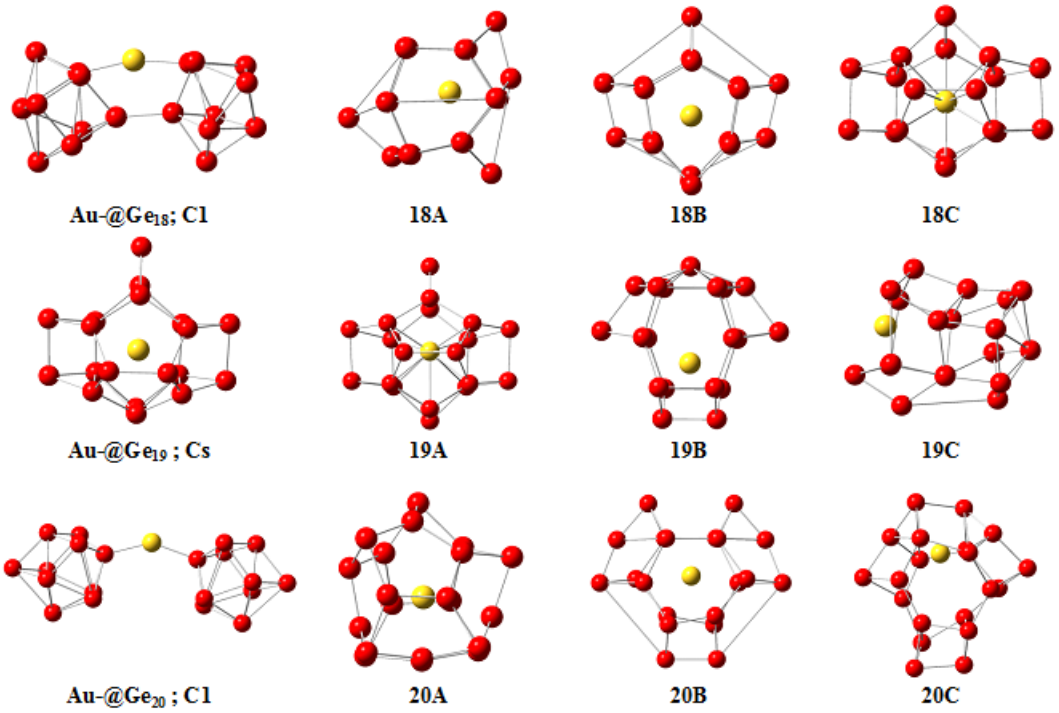

Figure C.4: Selected optimized low energy isomers $AuGe_n^-$ (n=18 to 20) First column has the ground state structure and next A,B and C are the nearest energy isomers. Red and yellow balls represent Ge and Au atoms respectively.

Gaussian basis set for Au and Ge

```
Au    0
S  3   1.00
     2.8090000          -1.2021556
     1.5950000           1.6741578
     0.5327000           0.3526593
S  4   1.00
     2.8090000           1.1608481
     1.5950000          -1.8642846
     0.5327000          -1.0356230
     0.2826000           1.3064399
S  1   1.00
     0.0598000           1.0000000
P  3   1.00
     3.6840000          -0.2802681
     1.6660000           0.7818398
     0.5989000           0.4804776
P  2   1.00
     0.6838000          -0.0952078
     0.0977000           1.0299147
P  1   1.00
     0.0279000           1.0000000
D  2   1.00
     1.2870000           0.5844273
     0.4335000           0.5298161
D  1   1.00
     0.1396000           1.0000000
****

AU    0
AU-ECP    4    60
g-ul potential
 5
1    622.6287956          -60.0000000
2    136.2843607         -555.5292312
2     33.1549781         -168.0019785
2      9.9894895          -63.0399875
2      3.0481312           -4.2516681
s-ul potential
 6
0    194.7374304           3.0000000
1    351.5327447          38.6020880
2    122.3270402         864.8370727
2     32.0914617         374.9935520
2      5.2451812         289.7910100
2      4.4916223        -152.4532773
p-ul potential
 4
0    420.6158801           2.0000000
1    109.4417815          73.8885625
2     34.1714280         326.6729872
2      5.9879750         126.5814591
d-ul potential
 5
0    219.2666158           3.0000000
1    122.7297786          55.6793149
2     63.1063369         449.1987335
2     18.3684520         215.0269091
2      4.4972844          64.0840995
f-ul potential
 5
0    108.5506037           4.0000000
1     56.4795527          51.8065335
2     29.2069159         231.2183113
2      9.5440543         119.0047386
2      2.8965118          15.3424188

Ge 0
S  2   1.00
     0.8935000          -2.1756591
     0.4424000           2.4493467
S  1   1.00
     0.1162000           1.0000000
P  2   1.00
     1.8770000          -0.1006779
     0.2623000           1.0306256
P  1   1.00
     0.0798000           1.0000000
P  1   1.00
     0.0209000           1.0000000
D  1   1.00
     0.2460000           1.0000000
****

GE    0
GE-ECP    3    28
f-ul potential
 5
1    318.2167583          -28.0000000
2     61.5370967         -180.9891676
2     13.2986899          -55.0043909
2      3.8985215          -19.7906526
2      1.2137666           -1.8533572
s-ul potential
 5
0    205.1886932           3.0000000
1     68.9790278          65.2262558
2     27.9194879         225.2354522
2      8.5481650          94.0125472
2      2.3173734          29.9415005
p-ul potential
 5
0     33.2488002           5.0000000
1     15.7777247          23.4778157
2     14.9260722          45.0980414
2      5.8416394          56.3326957
2      1.8349575          16.6058640
d-ul potential
 5
0     42.0206343           3.0000000
1     19.2096363          23.7371518
2      9.4133917          56.4792249
2      3.3282907          25.8901835
2      0.8522331           3.0229836
```

Appendix D

Functionalized Cluster Assembled TM doped Si Nanotubes

D.1 Confirmation of stability: Study of IR spectrum and Free energy variation of the clusters with the increase of the cluster size as functionalized assembled materials as finite nanotubes

In order to provide spectroscopic fingerprints of the finite nanotubes, as an example we have calculated the IR spectrum of Type 1 nanoclusters ($Si_{12}Cr$, $Si_{24}Cr_3$, $Si_{36}Cr_5$ and $Si_{12}Fe$, $Si_{24}Fe_3$, $Si_{36}Fe_5$) as shown in Fig. D.1 . For the Cr doping, the spectrum shows three prominent peaks at 248 cm^{-1}, 260 cm^{-1} and 275 cm^{-1} for $Si_{12}Cr$, $Si_{24}Cr_3$, $Si_{36}Cr_5$ unites. Similarly for Fe doping, these pecks are 270 cm^{-1}, 238 cm^{-1} and 275 cm^{-1}.

Using these vibration frequencies, we have also calculated the free energies including the vibrational entropies within the quasi-harmonic approximation[181]:

$$F(T) = E_0 + \frac{1}{2}\sum_i h\nu_i + k_B T \sum_i ln\left[1 - e^{-\frac{h\nu_i}{K_B T}}\right] \tag{D.1}$$

where E_0 is the total energy, and i are the vibrational frequencies of the clusters. In the Fig. D.2, we demonstrate the variation of free energy with temperature from 0 to 1000K. It can be clearly seen in Fig. D.2 that the addition of functionalized

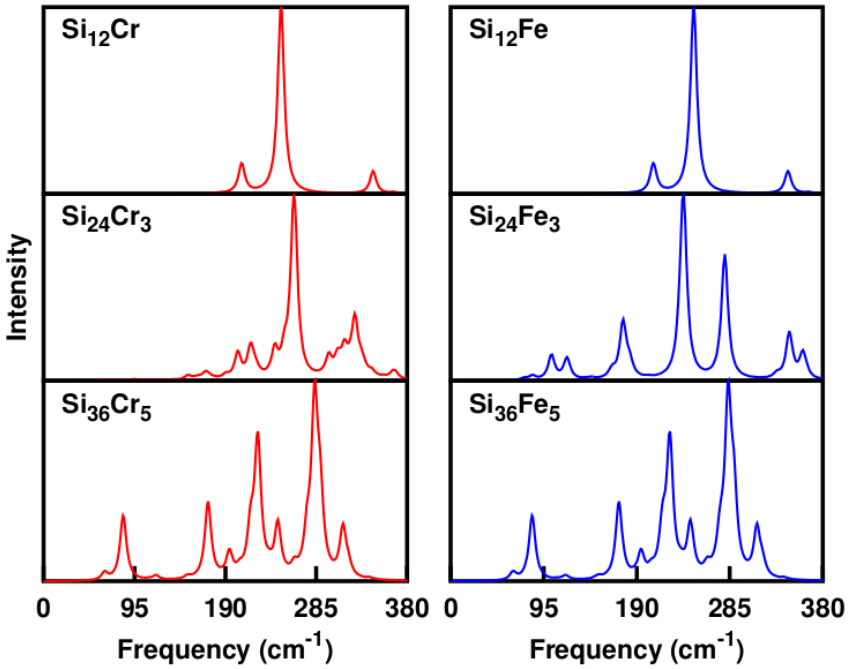

Figure D.1: IR frequency variation of type 1 functionalized clusters assemblies.

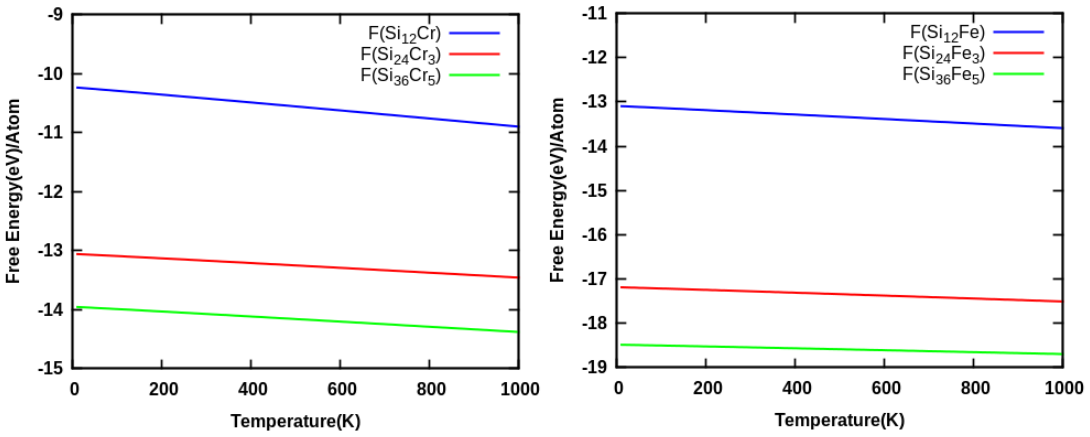

Figure D.2: Variation in free energies including the vibrational entropies within the quasi-harmonic approximation with temperature.

units at the end of the tubes reduces the energy. This indicates the stability of the bigger sized units.

D.2 Density of states

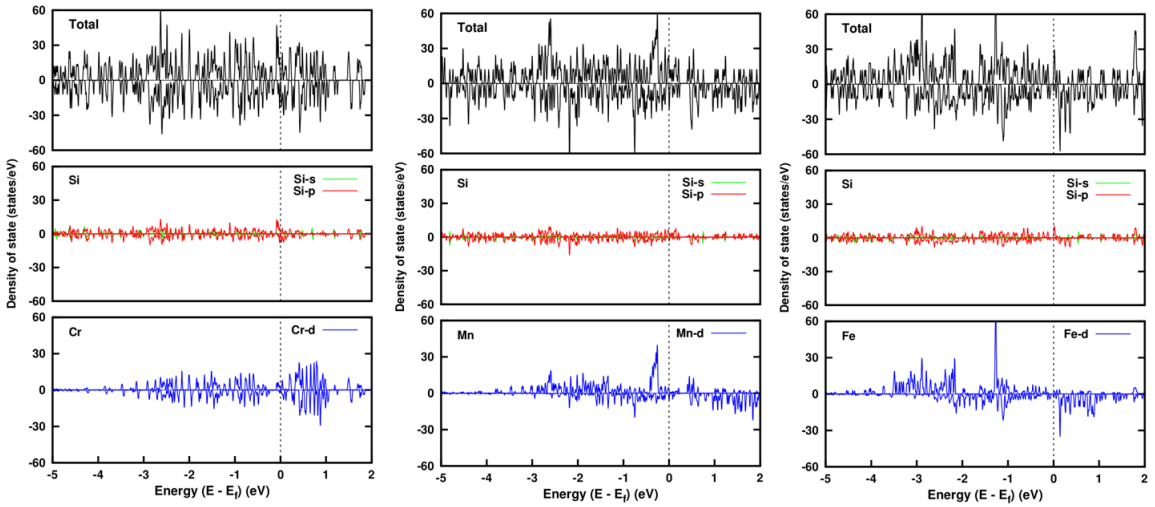

Figure D.3: Variation of DOS and PDOS with energy near Fermi level for type 1 $(Cr_4Si_{24})_n$, $(Mn_4Si_{24})_n$ and $(Fe_4Si_{24})_n$, infinite nanotubes, respectively.

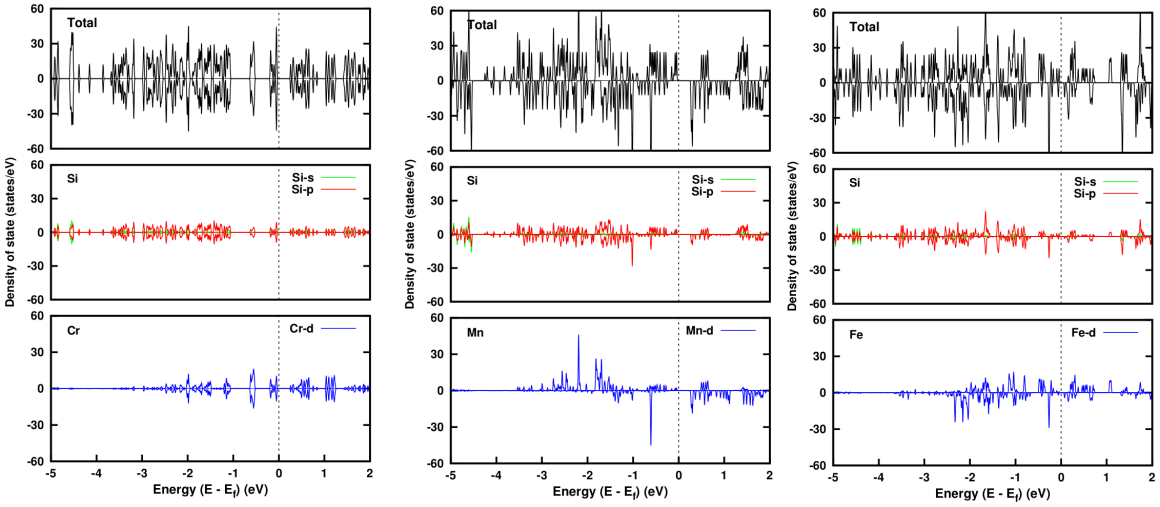

Figure D.4: Variation of DOS and PDOS with energy near Fermi level for type 2 $(Cr_2Si_{24})_n$, $(Mn_2Si_{24})_n$ and $(Fe_2Si_{24})_n$, infinite nanotubes, respectively.

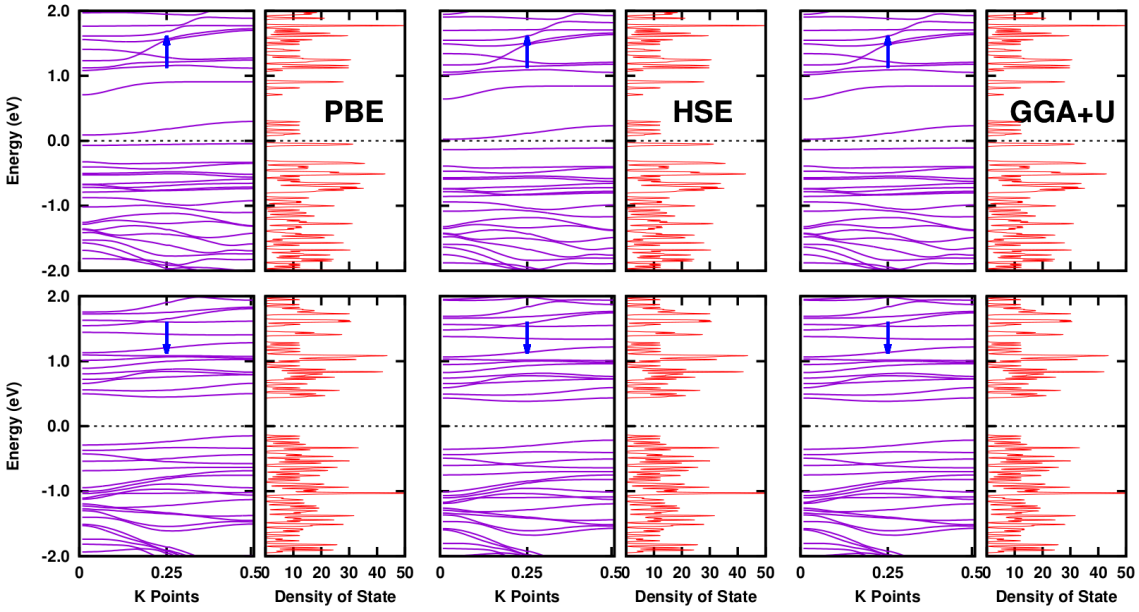

Figure D.5: Comparison of the band structure and DOS calculated using different approach as PBE, hybrid functional HSE and GGA+U in Mn doped Si Type 3 nanotube It can be clearly seen that band gaps from each level of theory are almost same.

Appendix E

LIST OF PUBLICATIONS

Publications in international journals

1. **Electronic structure and stabilities of Ni-doped germanium nanoclusters: a density functional modeling study**
   Kapil Dhaka, Ravi Trivedi and Debashis Bandyopadhyay, J. Mol. Model (2013), 19,1473-1488.
2. **Shell Magnetism in Chromium Doped Germanium Superatom**
   Kapil Dhaka and Debashis Bandyopadhyay, Adv. Sci. Lett. 20, 1135-1137 (2014)
3. **Study of electronic properties, stabilities and magnetic quenching of molybdenum-doped germanium clusters: a density functional investigation.**
   Ravi Trivedi, Kapil Dhaka and Debashis Bandyopadhyay, RSC Adv. (2014), 4, 64825-64834
4. **Study of electronic structure, stability and magnetic quenching of $CrGe_n$ (n=1-17) clusters: A density functional investigation**
   Kapil Dhaka and Debashis Bandyopadhyay, RSC Adv. 2015, 5, 83004-83012
5. **Stabilization and magnetism of Si-based nanotubes: A density functional study Metallic characteristics of transition metal doped Si-nanotube**
   Kapil Dhaka and Debashis Bandyopadhyay, Dalton Transection (Accepted, 2016)

Publication in conference

1. **Magnetic behavior in $Cr_2@Ge_n$ ($1 \leq n \leq 12$) Clusters: A Density Functional Investigations**

   Kapil Dhaka, Ravi Trivedi and Debashis Bandyopadhyay, AIP Conf. Proc. 1591, 1498 (2014)

Appendix F

LIST OF PRESENTATIONS

1. **Oral presentation:** Workshop on High Performance Computing, Inter University Accelerator Centre, New Delhi during 11-13 March, 2015.
2. **Oral presentation:** International Conference in Nanoscience and Nanotechnology, ICNN -2013. BBAU, Lucknow, during 18-20 Nov, 2013.
3. **Poster presentation:** International Symposium on Clusters, Cluster–Assemblies and Nanomaterials IISER TVM, Trivandrum, during 9-12 March, 2016.
4. **Poster presentation:** School on Nanoscale Electronic Transport and Magnetism: Fundamentals to Applications, HRI, Allahabad during 22-Feb to 2-March, 2016.
5. **Poster presentation:** 58th DAE Solid State Physics Symposium 2013, Thapar University, Patiala, Punjab during 17–21 December, 2013.
6. **Poster presentation:** International E-Workshop on Computational Condensed Matter Physics and Materials Science, IWCCMP-2013, IIITM, Gwalior, during 27-29 Nov, 2013.
7. **Poster presentation:** National conference in condensed matter physics, NCCMP -2012, Birla Institute of Technology and Sciences, Pilani, during 24-25 February, 2012.

Appendix G

BIOGRAPHY OF THE CANDIDATE

Mr. Kapil is a full time research scholar in the Department of Physics, BITS, Pilani. He is working in the field of a computational materials since August 2011. He did his Graduation (Physics, Chemistry and Mathematics) from University of Rajasthan, Jaipur in the year of 2006 and did his Masters degree in Physics with specialization in Electronics from Malviya National Institute of Technology (M.N.I.T.), Jaipur in the year of 2008.

His research interests are study of material properties based on first principle electronic structure methods. His prime focus in research is to study electronic and magnetic properties of transition metal (TM) doped semiconductor nano-clusters by using density functional approach. Since 2011, he has five peer reviewed publication in international journals and presented his work in seven national or international conferences.

Apart from this, he has qualified CSIR NET in December 2013 and GATE-2012. Worked as fellow in BITS, he was BITS JRF from 2011 to 2013 and after that he was UGC-BSR fellow.

Appendix H

BIOGRAPHY OF THE SUPERVISOR

Prof. Debashis Bandyopadhyay is an experimental and theoretical condensed matter physicist. He obtained his Ph.D. from Indian Institute of Technology (I.I.T), Kanpur in experimental condensed matter physics in the year of 1997. After spending a couple of years in IIT Kanpur as post doctoral fellow he joined Emory University, Atlanta, USA his second post doctoral work. There he worked on the study of reaction kinetics of several proteins at low-temperatures. Then returning to India, he joined the physics department of BITS, Pilani. He has wide range of research experiences in several fields, like, low temperature physics, magnetism, industrial material, mineral processing, fuel, alloys phase diagram, reaction kinetics in biological systems etc. Currently his main research focus is density functional theory based study of magnetic nanoclusters, transition metal doped semiconductor nanoclusters and super atoms which are useful for several potential applications in science and technology. He is the author of several research papers published in reputed international journals. At present he is professor in the department of physics in BITS Pilani.